AERODYNAMICS AND AEROACOUSTIC SOURCES OF A COAXIAL ROTOR

A Dissertation
Presented to
The Academic Faculty

By

Natasha Lydia Schatzman

In Partial Fulfillment
of the Requirements for the Degree
Doctor of Philosophy in the
Daniel Guggenheim School of Aerospace Engineering

Georgia Institute of Technology

May 2018

AERODYNAMICS AND AEROACOUSTIC SOURCES OF A COAXIAL ROTOR

Approved by:

Professor Narayanan M. Komerath, Advisor
Daniel Guggenheim School of Aerospace Engineering
Georgia Institute of Technology

Professor Lakshmi N. Sankar
Daniel Guggenheim School of Aerospace Engineering
Georgia Institute of Technology

Professor Kenneth S. Brentner
Department of Aerospace Engineering
The Pennsylvania State University

Dr. Gloria Yamauchi
National Aeronautics and Space Administration (NASA)
Ames Research Center

Professor Daniel Schrage
Daniel Guggenheim School of Aerospace Engineering
Georgia Institute of Technology

Professor John R. McIntyre
Scheller College of Business
Georgia Institute of Technology

Professor Mitchell L. R. Walker II
Daniel Guggenheim School of Aerospace Engineering
Georgia Institute of Technology

Date Approved: April 6, 2018

Dedicated to my mentor and friend Dr. Wel Chong (Ben) Sim.

ACKNOWLEDGEMENTS

I would like to thank my husband, Dr. David M. Schatzman, for all of his love and support. You have been my support system throughout the process and gave me advice to help me along the way. Special thanks to my parents, Mr. and Mrs. James and Lydia Barbely, thank you for supporting my educational goals. My grandmother, Mrs. Lydia Zakrewsky, has shown me that it takes hard work and courage to succeed, thank you. Thank you to my brothers, Eric and Allen Barbely, for guiding me into engineering as a young lady. A special thank you to my sisters, Crystal Bowen and Erin Barbely, thank you for your patience and guidance. Thank you Crystal Bowen and Eric Barbely for being my support system in Atlanta and being there when I needed you the most. Thank you Katie Pope for being my best friend and support system over the years. Thank you Meridith Segall and Tammy Baier for listening and guiding me during my early and current years at NASA. Thank you to all of my friends and family not mentioned.

I have been blessed to have coworkers and teachers at NASA Ames Research Center, U.S. Army Aviation Development Directorate, and the Georgia Institute of Technology that have given me professional development advice to help better my future including, but not limited to: Dr. Wel Chong (Ben) Sim, Dr. William Warmbrodt, Dr. Gloria Yamauchi, Mr. Ethan Romander, Professor Narayanan Komerath, Ms. Susan A. Gorton, Professor Kenneth Brentner, Mr. Cahit Kitaplioglu, Dr. Wayne Johnson, Mr. Mark Potsdam, Dr. Neal Chaderjian, Dr. Thomas Pulliam, Mr. Barry Lakinsmith, Dr. Colin Theodore, Mr. Thomas Norman, Mr. Larry Meyn, Dr. Carlos Malpica, Dr. Alan Wadcock, Mr. Larry Young, Mr. Eduardo Solis, Mr. Rohit Jain, Professor Lakshmi N. Sankar, Professor Daniel Schrage, Professor Jechiel Jagoda, Professor John R. McIntyre, Ms. Kristen Kallstrom, Ms. Michelle Dominguez, Mr. Witold Koning, Mr. Geoffrey Ament, Ms. Shirley Burek, Mr. Luke Novak, Professor Ganesh Rajagopalan, and Professor Vrishank Raghav.

A special thank you to my rabbit, Chestnut. You have helped keep me calm, I love you

Chestnut. A special thank you to my canine friends and family: Mr. Sherman Potsdam, Mr. Coby Liang-Sun, Ms. Daisy Liang-Sun, and the late Ms. Lucky Barbely, Mr. Piper Potsdam and Mr. Chance Liang-Sun.

First and foremost, I am blessed to have all of these people in my life because of the Lord. Thanks be to God!

TABLE OF CONTENTS

LIST OF TABLES

LIST OF FIGURES

NOMENCLATURE

Symbol	Description
Ai	airfoil i
B_1	single rotor blade one
B_2	single rotor blade two
c	chord (ft)
c_0	speed of sound in undisturbed medium (ft/s)
c_l	coefficient of 2D sectional lift
c_{l_α}	2D lift curve slope
c_d	coefficient of 2D sectional drag
c_x	coefficient of 2D sectional force in the horizontal direction
c_z	coefficient of 2D sectional force in the vertical direction
C_P	rotor power coefficient
C_T	rotor thrust coefficient
D	rotor diameter (ft)
dS	element of the rotor blade surface (ft)
h	miss distance (ft)
$\overline{I}$	BVI impulse factor
$L1$	lower rotor blade one
$L2$	lower rotor blade two
LAi	lower airfoil blade i
Li	lower rotor blade i
l_i	components of local force intensity that acts on the fluid, l_i= $P_{ij}\, n_{\hat{j}}$
l_r	$l_i\, \hat{r}_i$
$\dot{l}_r$	$\dot{l}_i\, \hat{r}_i$

$\vec{M}$	vector of local source Mach number with respect to a frame fixed to the undisturbed medium, with components M_i
M	$\left\vert\vec{M}\right\vert$
M_{tip}	tip Mach number
M_{r}	Mach number of source in radiation direction, $M_i\ \hat{r}_i$
$\dot{M}_r$	$\dot{M}_i\ \hat{r}_i$, where $\dot{M}_i$ = $\frac{\partial M}{\partial tau}$
N_b	number of blades (per rotor)
$\hat{n}$	unit outward pointing normal vector to rotor blade surface, with components $\hat{n}_i$
P_{ij}	compressive stress tensor
P	rotor power (hp)
p'	acoustic pressure in undisturbed medium
Q	torque (lb_f-ft)
R	rotor radius (ft)
r	distance between source and observer (ft)
r/R	dimensionless radial position
r	spanwise radial position (ft)
$\hat{r}$	unit vector in the radiation direction, with components $\hat{r}_i$
T	rotor thrust (lb_f)
t	observer time (s)
T_U	upper rotor thrust (lb_f)
T_L	lower rotor thrust (lb_f)
UAi	upper airfoil blade i
Ui	upper rotor blade i
V	forward flight velocity (ft/s)
V_i	downwash, induced inflow (ft/s)
V_b	translating blade velocity (ft/s)

v_n	local normal velocity of rotor blade (ft/s)
$\dot{v}_n$	$\dot{v}_i \, \hat{n}_i$
$v_{\dot{n}}$	$v_i \, \dot{\hat{n}}_i$
V_{tip}	rotor blade rotational speed at tip (ft/s)
$\overline{X}$	shape function
$\vec{x}$	observer location vector with x, y, and z components (ft)
$\vec{y}$	source location vector with x, y, and z components (ft)
Z	vertical distance between rotors or airfoils (ft)
α	airfoil angle-of-attack (deg), positive pitch up
α_S	blade pitch angle (deg), positive pitch up
Γ	vortex strength
$\overline{\Gamma}$	vortex strength factor
γ	blade-vortex interaction angle (deg)
$\frac{\partial F}{\partial t}$	time rate of change of loading
κ_{int}	coaxial rotor induced power interference factor
λ_i	inflow (ft/s)
μ	advance ratio (V/V_{tip})
ω	rotor angular velocity (rad/s)
ρ_0	density in medium (slugs/ft^3)
σ	rotor solidity, $\frac{N_b c R}{\pi R^2}$
τ	source time (s)
θ_S	single rotor collective pitch angle (deg)
θ_L	lower rotor collective pitch angle (deg)
θ_U	upper rotor collective pitch angle (deg)
θ_{1cU}	upper rotor lateral cyclic pitch (deg)
θ_{1cL}	lower rotor lateral cyclic pitch (deg)
θ_{1sU}	upper rotor longitudinal cyclic pitch (deg)

θ_{1sL}	lower rotor longitudinal cyclic pitch (deg)
χ_{TPP}	wake skew angle(deg)

Subscripts

ISO	isolated airfoil
i	blade and airfoil number counter (1, 2, 3, 4, ...)
L	loading noise component (Pa)
ret	quantity is evaluated at the retarded time, $\tau = t + \frac{r}{c}$
T	thickness noise component (Pa)

SUMMARY

Vehicles with coaxial, contra-rotating rotor systems (CACR) are being considered for a range of applications, including those requiring high speed and operations in urban environments. Community and environmental noise impact is likely to be a concern in these applications. Design parameters are identified that affect the fundamental aerodynamics and fluid dynamic features of a CACR in hover, vertical, and edgewise flight. Particular attention is paid to those features affecting noise sources. These sources include thickness, loading, blade-vortex interaction (BVI), and high-speed-impulsive (HSI) noise. Understanding the fluid dynamic features is a precursor to studying the aeroacoustics of a coaxial rotor.

A literature survey has been completed, listing theoretical, computational, and experimental studies relevant to CACR. Due to the lack of information in regards to the flow field and acoustics of CACR compared to single rotor systems, this dissertation investigates the aerodynamic and aeroacoustic sources of CACR by investigating each noise source independently. The impact of thickness, circulation, compressibility, viscosity, downwash, and shed vorticity of a CACR are compared to a single rotor system and the rotor noise sources are identified.

Two blades passing in close proximity can cause strong compressibility effects that can have a profound impact on noise generation. Prior to examining the complex 3D flow field of a coaxial rotor in detail, two airfoils traveling in opposite directions were simulated. Furthermore, two trains of eight airfoils passing are simulated to understand the effects due to shed vorticity, and a vertical velocity is simulated representative of downwash. The airfoils are displaced vertically by a distance equivalent to the typical spacing between the upper and lower rotors of a coaxial system. A 2D potential flow code and the 2D OVERFLOW compressible-flow Navier-Stokes solver were used to investigate the complex coaxial rotor system flow field.

A 2D potential flow solver simulated two airfoils crossing, modeling the airfoil as a source, vortex and sink. The simulation revealed that the lift of both the upper and lower airfoils increased before the crossing, followed by a decrease in lift after the crossing. Before the crossing, the upper airfoil sees an increase in angle-of-attack due to the upwash from the lower airfoil. The angle-of-attack of the lower airfoil also increases due to the upwash from the upper airfoil, therefore an increase in lift is experienced by both airfoils. The opposite occurs after the airfoils pass each other, where a decrease in lift is seen for both the upper and lower airfoil. This phenomenon is a circulation effect, which contributes to loading noise.

2D OVERFLOW was used to further investigate circulation, along with thickness, compressibility, viscosity, downwash, and shed vorticity in 2D. Airfoil thickness effects were explored by comparing three different separation distances at a constant low speed for a symmetrical airfoil, this eliminated the large effects of circulation and compressibility. Comparing the upper and lower airfoils revealed that at low and high speeds, thickness effects due to the airfoil were negligible, although a vertical separation distance greater than twice the chord is recommended to avoid thickness effects of one rotor on the other. Furthermore, two different airfoils were compared to understand thickness noise contributions due to airfoil shape. This comparison indicated that thickness noise for a CACR compared to a single rotor is negligible at vertical separation distances larger than twice the chord.

For two airfoils crossing, the flow field and aerodynamic forces for three angles-of-attack with the same symmetrical airfoil, speed, and vertical separation distance were simulated using OVERFLOW in order to eliminate any large effects due to airfoil thickness or compressibility. When comparing circulation at various angles-of-attack, an angle-of-attack greater or less than zero resulted in a change in lift, drag, and moment before and after the airfoils crossed and therefore a change in loading noise.

High-speed-impulsive (HSI) noise due to compressibility effects was investigated in 2D by performing a Mach sweep (M = 0.5 through 1.2), while keeping angle-of-attack, airfoil

and vertical separation distance constant. The higher the Mach number, the larger the change in lift, drag, and moment at the time of overlap. As Mach numbers reach near 1.0, a large change in drag and moment was observed due to compressibility and the formation of weak shocks. The formation of shocks leads to possible rotor-rotor shock interaction. HSI noise can be reduced by ensuring the translating blade velocity does not exceed Mach numbers where possible rotor-rotor, shock-shock interactions can occur.

Simulations of an isolated airfoil, two airfoils crossing, a single train of eight airfoils, and two trains of eight airfoils were used to independently understand effects of shed vorticity and downwash in 2D. An airfoil overlap/crossing results in deposited shed vorticity in the flow field due to the rapid change in aerodynamic forces. The addition of downwash resulted in an overall decrease in lift and moment, and increase in drag. Computations of viscid and inviscid out of plane vorticity contours indicated that the deposited shed vorticity was pushed downward by the vertical downwash velocity, which in turn, deposited shed vorticity from the upper airfoils that directly impacted the lower airfoils. Overall, shed vorticity effects can be avoided with reduced rotor RPM and increased horizontal and vertical separation distance.

A hovering modern single and coaxial rotor system were simulated in 3D by stacking 2D OVERFLOW calculations along the rotor span. Using PSU-WOPWOP, OVERFLOW calculations were used as input to calculate thickness and loading noise. Compared to the single modern rotor, coaxial modern rotor acoustic predictions revealed a minimal contribution to thickness noise as compared to loading noise, even though the modern coaxial rotor design had three additional blades. Blade crossing events (circulation) are the dominate contribution to total noise.

The 3D CACR performance analysis used momentum theory and the RotUNS Navier-Stokes solver. Calculations were compared with data for the hovering CACR Harrington rotor tested in the 1950s. The simulation was extended to forward flight using the lifting-line blade model in RotUNS. Steady hover calculations showed improved accuracy

compared to blade element momentum theory using the ability of RotUNS to couple the rotor momentum disk to an incompressible, Navier-Stokes flow solver. The pressure fields above, between, and below the coaxial rotor system computed by RotUNS were then examined for different azimuth positions of the upper and lower rotor blades, this confirmed results from the 2D OVERFLOW simulations.

One challenge of analyzing the CACR is the difficulty in envisioning all the possible interactions and their possible locations as flight conditions and rotor designs change. A calculation tool was developed to identify time and location of blade overlap. The tool was then integrated with a wake aerodynamics model to identify locations and instances of upper rotor tip vortex interaction with a lower rotor blade. This tool enables rapid identification of different types of blade-vortex interaction (BVI) based on relative rotor orientation. Specific aerodynamic phenomena that occur for each noise source relevant to CACR are presented.

CHAPTER 1

INTRODUCTION AND BACKGROUND

Coaxial rotorcraft are finding increased use in civil and military applications, as well as in the small unmanned aerial vehicles (UAVs) market. As with all rotorcraft, the rotor noise generated by a coaxial contra-rotating rotor (CACR) system must be mitigated to minimize impact to the community. Unlike single main rotor helicopters, the CACR system results in aerodynamic interactions between the upper and lower rotor, especially their wakes, as shown in Fig. 1.1. A literature survey of CACR research was performed, and gaps in research are highlighted and discussed.

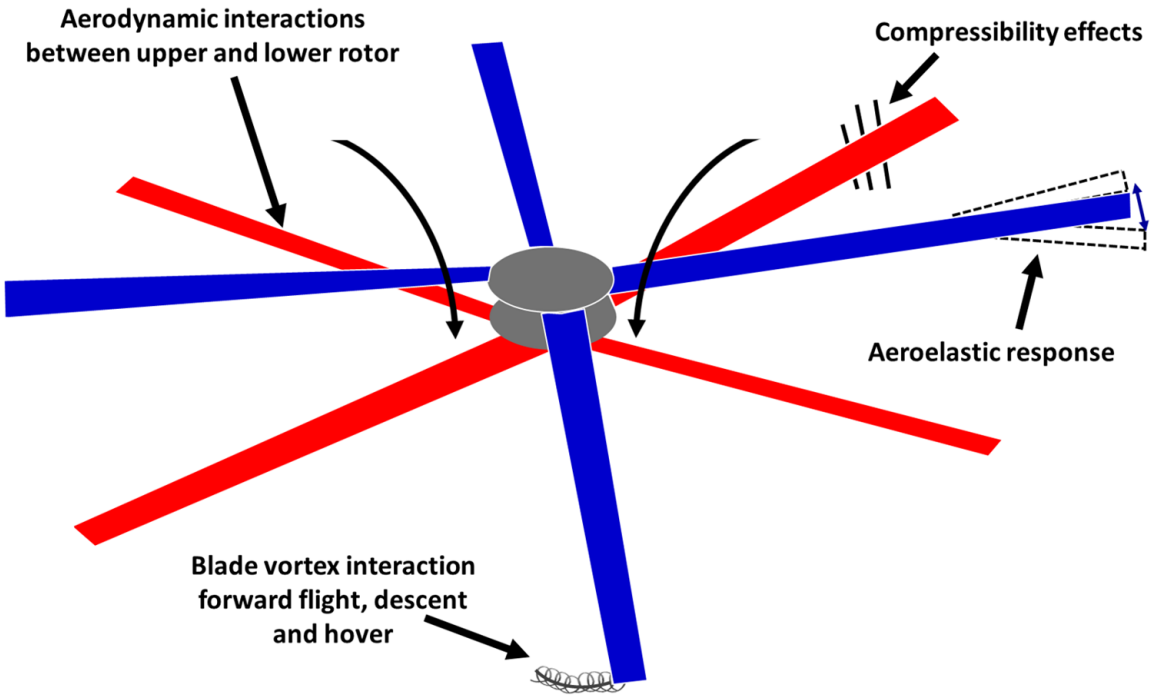

Figure 1.1: Coaxial rotorcraft aerodynamic complexities

1.1 Literature survey

Unlike single-main rotor or tiltrotor configurations, there are limited analytical and experimental studies on CACR noise [1, 2, 3, 4, 5, 6]. Studies on CACR performance are highlighted below. Coleman [7] provides a thorough summary of experimental and analytical studies of CACR through 1997. In the U.S., the first documented coaxial rotor test was a hover test by Taylor in 1950 [8] in the full-scale wind tunnel at NASA Langley Research Center. The CACR consisted of two 20-in diameter rotors, with two blades per rotor. The test objective was to visualize the flow through several (single, coaxial, tandem) rotor configurations with and without a ground plane present. A surprisingly small number of coaxial rotor hover experiments have been performed since the Taylor test, with the work by Ramasamy [9] being the most comprehensive. Ramasamy measured the performance of single, coaxial, tandem, and tiltrotor configurations using untwisted and twisted blade sets. The coaxial rotor system comprised two independent test rigs allowing performance measurements of the upper and lower rotor separately. Ramasamy provided a convenient summary of coaxial rotor hover performance measurements prior to 2013, including those surveyed by Coleman. More recently, Cameron et al. [10] measured the performance of a single rotor and coaxial rotor system using an 80-in diameter rotor with untwisted blades. Hub loads and blade deformation were also measured. Coaxial rotor measurements in forward flight are scarcer compared to hover. Since 1997, the data from the Sikorsky X2 [11] flight test joins the handful of forward flight measurements included in the Coleman survey.

Analysis of coaxial rotor systems has progressed over the last decade thanks to improved modeling capabilities. Leishman and Ananthan [12] developed a Blade Element Momentum Theory (BEMT) model for coaxial rotors in hover and axial flight to design an optimum coaxial rotor for hover and used the Harrington data [13] to validate the model. Using momentum theory and the Harrington data, Leishman and Syal [14] developed expressions for the figure of merit for a coaxial rotor for four different operating conditions.

Ho et al. [15] summarized some of the more recent validation studies of coaxial rotors. Analysis validations have relied primarily on the Harrington [13] and Dingeldein [16] large-scale coaxial rotor data. Though the Ramasamy data are for an approximately 4.3-ft diameter coaxial rotor system, the individual rotor performance measurements are valuable for analysis validation. Ho et al. [15] used RCAS (a comprehensive rotorcraft analysis) to model the rotors used by Harrington and Ramasamy to compute coaxial rotor performance in hover and forward flight. Table 1.1 lists the validation studies discussed by Ho et al. [15], including the configurations modeled and the data set used for validation.

Using lift offset rotors in a coaxial rotor system has gained interest in recent years. Lift offset rotors maintain lift on the advancing side of the rotor disk in forward flight by eliminating the requirement for roll moment balance of the rotor. A very stiff hingless rotor is used to carry the roll moment. By changing angle-of-attack and loading distribution over the disk, the retreating side does not have to carry lift to balance the advancing side, so the retreating side does not have to approach stall. Lift offset is accomplished by varying the blade pitch distribution around the azimuth. Changing the lift vector location affects the overall performance, though dynamic stall still occurs but not as severe because the location of the lift vector changes. The location of the lift offset rotor vector depends on the aerodynamics, which is controlled by varying the collective pitch (θ_0), lateral cyclic pitch (θ_{1c}), and longitudinal cyclic pitch (θ_{1s}). The collective pitch is the zeroth harmonic and the lateral and longitudinal cyclic pitch are the first harmonic.

The idea of lift offset rotors has been crucial in enabling CACR vehicle designs for high-speed forward flight. The vehicle rolling moment is balanced by having contra-rotating rotors, so that one rotor is always advancing on each side of the vehicle. However, each rotor is now likely to generate strong root moments requiring stiffer hub designs [17].

Kim and Brown [18, 19, 4, 3] exercised their Vorticity Transport Model (VTM) analysis, and also predicted maneuverability performance of a lift-offset rotor using Harrington [13] and Dingeldein [16] data for validation and design. Kim and Brown [4, 3] are one of

the few studies on coaxial rotor noise.

Juhasz et al. [20] applied three aerodynamic models to simulate the McAlister et al. [21] model-scale coaxial rotor in hover. The three models include BEMT, a free-wake model and CFD using OVERFLOW2. A combination of the three methodologies was found to be the best approach to analyze the aerodynamics, though dependent on the level of detail desired. Schmaus and Chopra [22] developed a comprehensive analysis for a coaxial rotor for high advance ratios, using the code UMARC. The experimental rotor data from the University of Texas at Austin [10] along with data from the Harrington rotor 1 [13] and the XH-59A [23] were used for validation. Using the University of Texas rotor [10], the flight envelope for high advance ratios was defined for anticipated experimental tests.

Singh and Kang [24] performed computational simulations using a loosely coupled CFD(Helios) / CSD(RCAS) approach using a scaled-model coaxial rotor in hover from the University of Texas [10]. Results revealed that the interference between the upper and lower rotor required a CSD solver in order to have a robust trim convergence.

Walsh et al. [25, 26] performed computational aerodynamic and aeroacoustic predictions using RCAS and PSU-WOPWOP respectively, for the XH-59A [23]. Thickness and loading noise were explored with emphasis on blade crossings and BVI for a variety of high-speed flight conditions.

The approach to explore a coaxial rotor in 2D, developed by the on going work of Schatzman (formerly Barbely) et al. [27, 28, 29, 30] was pursued in a recent papers by Singh and Friedmann [31, 32]. Using vortex discretized airfoils, Singh and Friedmann's 2D simulations included effects of downwash and shed vorticity by using periodic boundaries. Furthermore, ongoing coaxial rotor computational and experimental research has been performed by the University of Maryland [33, 34] and University of Texas at Austin [35], with focus on rotor performance and blade flap bending moments, particularly with variation in lift offset.

Limited research in regard to the fundamental aerodynamics specific to CACR was found. To build upon the existing literature, performance and flow field characteristics of CACR are explored in the present work to further understand the aerodynamics and acoustic sources. This work uses the hybrid-CFD analysis tool RotUNS for hover and forward flight performance predictions to compare against Harrington [13] and Dingeldein [16] data, as well as 2D OVERFLOW to understand various aerodynamic phenomena. The effect of the relative position of the upper and lower rotor blades on the flow field pressures near the rotor blades, which are important for acoustics, is studied. This exploration of the physics of coaxial aerodynamics adds to the computational work of Table 1.1.

Table 1.1: Computational investigations of coaxial rotors in hover (h) and forward flight (ff).

Citation	Flight condition	R (ft)	V_{tip} (ft/s)	N_b (per rotor)	Z/D	Validation data
Leishman and Ananthan 2006 [12]	hover	12.5	500	2	0.095	[13]
	h	12.5	327, 392	2	0.080	[13]
Wachspress and Quackenbush 2006 [2]	h	1.25	400	4	0.105 - 0.5	[36]
	ff	26.0	740	3	0.095	[37]
McAlister et al. 2006 [21]	h	2.04	165	3	0.1 - 0.73	[21]
Bagai 2008 [38, 11]	h	13.2	620	4	N/A	[11]
		13.2	620	4	N/A	[11]
Ruzicka and Strawn 2008 [39]	h	2.04	165	3	0.1 - 0.73	[21]
Kim and Brown 2009 [18, 19, 4, 3]	h	12.5	500	2	0.095	[13]
	ff	12.5	469	2	0.095	[16]
Lim at al. 2009 [40]	hr	12.5	500	2	0.095	[13]
	h	12.5	327, 392	2	0.080	[13]
	hover	2.04	165	3	0.1 - 0.73	[21]
	h	18.0	650	3	0.0694	[23]
Johnson 2009 [41]	hover	18.0	650	3	0.0694	[23]
	h	12.5	500	2	0.095	[13]
	hover	12.5	327, 392	2	0.080	[13]
	ff	18.0	650	3	0.0694	[23, 42]
	ff	12.5	469	2	0.095	[16]
Lakshminarayan and Baeder	h	12.5	327, 392	2	0.080	[13]
	h	0.28	55 - 80	3	0.625	[43]

2009 [44]						
Juhasz et al.	h	12.5	500	2	0.095	[13]
2010 [20, 22]	h	2.04	165	3	0.1 - 0.73	[21]
	ff	18.0	650	3	0.0694	[23]
	ff	2.04	165	3	0.1 - 0.73	[21]
Johnson et al.	h	18.0	650	3	0.0694	[23]
2012 [17]	h	13.2	620	4	N/A	[11]
	ff	18.0	650	3	0.0694	[23]
	ff	13.2	620	4	N/A	[11]
Yeo and Johnson.	h	18.0	650	3	0.0694	[23]
2013 [45]	ff	18.0	650	3	0.0694	[23]
Rajmohan et al.	h	2.04	165	3	0.1 - 0.73	[21]
2014 [46]						
Ho et al.	h	12.5	500	2	0.095	[13]
2015 [15]	hover	12.5	327, 392	2	0.080	[13]
	hover	2.17	182, 273	3	0.05 - 1.5	[9]
	hover	2.15	180, 270	3	0.05 - 0.75	[9]
Schmaus and Chopra	h	12.5	500	2	0.095	[13]
2015 [22]	h	18.0	650	3	0.0694	[23]
	hover	3.83	573	2	0.060	[10]
Singh and Kang	h	12.5	500	2	0.095	[13]
2015 [24]	h	3.83	573	2	0.060	[10]
Walsh	ff	18.0	650	3	0.0694	[23]
2016 [25]						
Barbely et al.	h	12.5	500	2	0.095	[13]
2016 [27, 28, 29, 30]	ff	12.5	469	2	0.095	[16]
Singh and Friedmann	h	12.5	500	2	0.095	[13]
2017 [31, 32]	h/ff	13.2	620	4	0.114	[11]
Bhagwat	hover/ff	3.33	623	2	0.068	[10, 35]
2017 [47, 15, 35]	hover	2.17	182, 273	3	0.05 - 1.5	[9]
	hover	2.15	180, 270	3	0.05 - 0.75	[9]

1.2 Scope and objectives

The goal of this work is to develop an analysis approach to understand the aerodynamics and aeroacoustics of a coaxial contra-rotating rotor and their relation to noise generation sources. The results will identify primary rotor design parameters that affect noise, informing low-noise CACR designs.

1.3 Coaxial rotor aerodynamic features

A contra-rotating rotor brings new aerodynamic challenges, primarily the interactions between the upper and lower rotor. Specifically in hover and low-speed flight, the wake from the upper rotor will impinge on the lower rotor blades and therefore, affect the performance [14]. In high-speed forward flight, the possibility of shock formation occurs for each rotor and introduces the possibility of shock-shock interactions between the rotors. In descent or climb, coaxial rotors complicate blade-vortex interactions occurrences, with the possibility of tip vortices from one rotor interacting with the other rotor [3].

1.4 Coaxial rotor aerodynamic acoustic sources

The Ffowcs Williams-Hawkings equation [48] extended Sir James Lighthill's [49] acoustic analogy to include turbulence and sound generation from surfaces that are in arbitrary motion, which is used for various rotor configurations. Equations 1.1 through 1.3 are known as Formulation 1A, which are the solutions of the Ffowcs Williams-Hawkings equation [50].

$$p'(\vec{x},t) = p'_T(\vec{x},t) + p'_L(\vec{x},t), \tag{1.1}$$

where

$$4\pi p'_T(\vec{x},t) = \int_{f=0} \left[\frac{\rho_0(\dot{v_n} + v_{\dot{n}})}{r\left|1-M_r\right|^2}\right]_{ret} dS + \int_{f=0} \left[\frac{\rho_0 v_n(r\dot{M}_r + cM_r - c_0M^2)}{r^2\left|1-M_r\right|^3}\right]_{ret} dS \tag{1.2}$$

$$\begin{aligned} 4\pi p'_L(\vec{x},t) = \frac{1}{c}\int_{f=0} \left[\frac{\dot{l_r}}{r\left|1-M_r\right|^2}\right]_{ret} dS + \int_{f=0} \left[\frac{l_r - l_M}{r^2\left|1-M_r\right|^2}\right]_{ret} dS \\ + \frac{1}{c}\int_{f=0} \left[\frac{l_r(r\dot{M}_r + c_0M_r - c_0M^2)}{r^2\left|1-M_r\right|^3}\right]_{ret} dS \end{aligned} \tag{1.3}$$

A complete derivation and theoretical background of the Ffowcs Williams-Hawkings equation is presented by Brentner and Farassat [51]. A fundamental understanding of retarded time is important when predicting noise. The time at the source (τ) and time at the observer (t) are two different but dependent variables based on distance (r) between the source ($\vec{y}$) and the observer ($\vec{x}$), and the speed of sound in the undisturbed medium (c_o). The source location ($\vec{x}$) is dependent on rotor radius (R), rotor velocity (ω), and τ. The relation is mathematically represented in Equations 1.4 through 1.6.

$$t = \tau + \frac{r}{c_0} \tag{1.4}$$

where

$$r = |\vec{x} - \vec{y}| \tag{1.5}$$

$$\vec{y} = -R(cos(\omega\tau), sin(\omega\tau), 0) \tag{1.6}$$

The Ffowcs Williams-Hawkings equation consists of monopole, dipole, and quadrupole sources used to mathematically model the noise. Three categories of noise (thickness, loading, and high-speed-impulsive noise) are discussed below. Loading is inclusive of steady loading and unsteady loading. Unsteady loading noise includes blade-vortex interaction (BVI), broadband, and blade-wake interaction (BWI) noise, along with other unsteady noise sources.

1.4.1 Thickness noise

A rotor blade continuously displaces the air while rotating. The displacement is due to the geometric shape of the blade. This effect is mathematically modeled as a monopole source and is referred to as thickness noise. A monopole source can be described as a sphere that

repeatedly expands and contracts sinusoidally [52]. Thickness noise is predominately directed in the plane of the rotor or rotors [51]. For a coaxial rotor, the presence of two rotors in different locations will have two independent signals adding together linearly from two independent source locations. Compared to a single rotor, this rotor-rotor interaction gives rise to different aerodynamic flow behavior (air displacement) and emission directionality.

1.4.2 Loading noise

Loading noise can be both steady and unsteady. Within unsteady loading, the following noise sources are particularly important for coaxial rotors: Blade-Vortex Interaction (BVI), and Broadband or Blade-Wake Interaction (BWI) noise.

Steady loading

The noise generated by steady aerodynamic forces is referred to as loading noise and is directed below the rotor [51]. This loading noise can be mathematically modeled as a dipole. A dipole source is a combination of two spheres expanding and contracting, 180 degrees out of phase with each other [52].

Unsteady loading

Coaxial rotors create new problems due to the rotor wake interaction, unlike the single-main rotor. Crossings of the upper and lower rotor blades also generate unsteady loading occurrences.

A subset of unsteady loading is BVI, and is dependent on advance ratio, tip path plane, Mach tip number, and thrust [53], whether the rotor is in ascent, descent, or forward flight. BVI noise occurs when the tip vortices interact with a rotor blade [54]. BVI noise is usually out-of-plane, directed down and forward for single-main rotors; this is true for CACR with the addition of other directions. The strength of each interaction depends on the tip vortex strength, the local interaction angle between the blade and vortex, and the vertical distance

between the blade and vortex [55]. For coaxial rotors, the interaction between the lower rotor blade and the tip vortex from the upper rotor can create a close and possible interaction [3].

Analysis and prediction of rotor broadband noise has been performed, particularly by Brooks and Burley [56], but will not be explored in this dissertation.

1.4.3 High-speed-impulsive noise

High-speed-impulsive (HSI) noise can occur at high rotational or forward flight speeds where transonic flow and severe shocks can form on the rotor blade. HSI noise is mathematically modeled as a quadrupole [51]. HSI noise is acoustically radiated in front of the rotor, similar to the thickness noise radiation direction.

The addition of another rotor creates a possible shock-rotor blade interaction between the upper and lower rotor, unlike a single rotor where the shock would essentially have little or no interaction with another body or rotor. Although measurements of transonic flow over static airfoils have been conducted [57] and computationally predicted by many including Sengupta et al. [58], little or no work has been performed on coaxial rotor blade shock formation. With the lack of information available, the idea of possible upper rotor shock and lower rotor shock interaction becomes worth exploring.

CHAPTER 2

2D SIMULATION OF BLADE CROSSINGS

On a coaxial rotor, each rotor operates in the induced flow field produced by the opposing rotor. This complicated flow field introduces additional aerodynamic and aeroacoustic effects compared to the single rotor. One of the effects is due to blade crossings or blade overlap. Figure 2.1 shows a visual representation of how this 3D complex problem of blades crossing can be deconstructed to a 2D problem by simulating the upper and lower blades as airfoils moving past each other in opposite directions.

The 2D simulations aided in understanding the effects of circulation, thickness, compressibility, viscosity, shed vorticity, and downwash for a coaxial rotor. Information from these aerodynamic effects give insight into the aeroacoustic sources of thickness, loading, and high-speed-impulsive noise.

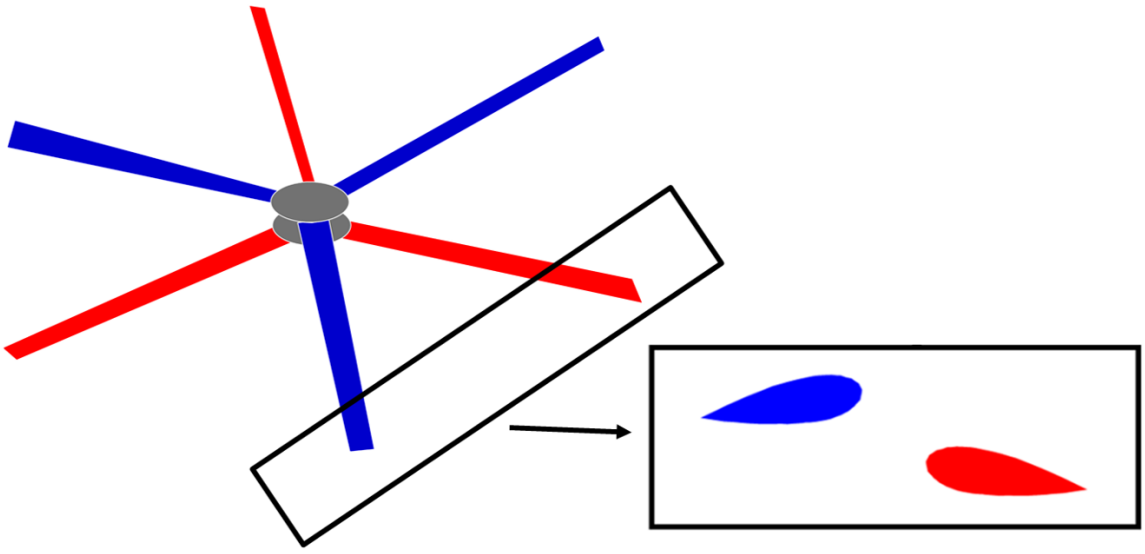

Figure 2.1: 3D representation of a coaxial rotor simulated in 2D as two airfoils moving past each other.

2.1 2D representation and assumptions

The first step towards understanding this complex 3D time-varying flow field was to model the coaxial rotor as a 2D potential flow simulation of two airfoils moving past each other. First, a simulation of two airfoils modeled as a source, vortex, and sink were computed to understand effects due to thickness and circulation. Next, a Navier-Stokes computational fluid dynamic tool was used to further investigate incompressible and compressible effects due to circulation, thickness, compressibility, shed vorticity, and downwash (inflow). Compared to the 3D model, the 2D representation did not capture span wise flow, tip vortices, and curvature. However, 2D results were stacked to approximate the 3D solution in hover. Forward flight cases were not investigated in 2D for this analysis.

2.2 Potential flow simulation

A simplified, incompressible simulation was used to understand the change in lift at the time of airfoil crossing (or overlap). A vortex was used in this model to simulate the effect of circulation, while a source and sink were used to represent the body of the airfoil in order to simulate thickness effects. A low-speed incompressible flow is a realistic conditions for inboard spanwise r/R locations.

2.2.1 Computational set up

The unsteady effects of two airfoils crossing in an incompressible flow ($M \leq 0.30$) was simulated using MATLAB. This simplified model enabled the aerodynamic interactions at the time of an airfoil crossing to be easily analyzed. To model the unsteady effects for an incompressible flow, assumptions included: 2D, inviscid, instantaneous reaction and airfoil modeled using a source, vortex and sink.

The upper and lower airfoils were each simulated using a source (leading edge), vortex (quarter-chord) and sink (trailing edge) as shown in Fig. 2.2 a). The source and sink gives

the ability to model thickness effects and while the vortex models circulation. Figure 2.2 b) shows a mathematical model of the individual sink, vortex, and source used to represent an airfoil. Figure 2.2 c) shows a simulated NACA 0012 airfoil at 9.8 degree angle-of-attack traveling at M = 0.25 using the source-vortex-sink model. The simulated airfoils are representative of a NACA 0012 with a chord of 0.5 ft. For the simulation of two airfoils crossing, the vertical separation distance was two chords. Since airfoil geometry was not fully modeled, only the change in angle-of-attack caused by the two airfoils crossing was analyzed.

2.2.2 Potential flow simulation results

The potential flow code VITS (Vortex Interaction Tracking Simulation) was developed to understand the aerodynamic behavior of airfoils crossing at a fixed vertical separation distance, where each airfoil is modeled as a source, vortex, and sink. VITS calculates c_l for each airfoil by using the Biot-Savart law and updating the airfoils vortex strength for each time step [59]. As the two airfoils approach each other, each airfoil induces a velocity on the other, resulting in a change in vortex strength. Figure 2.3 shows c_l versus distance to overlap for a flight condition of M = 0.25, α = 9.8°, and S/c = 4.0 (S = 2.0 ft, c = 0.5 ft) with no downwash for upper and lower airfoil. The c_l of the upper (UA) and lower (LA) airfoils for VITS calculations see an increase in lift before overlap followed by a decrease in lift after overlap. To understand the change in c_l before and after overlap, the flow field is analyzed.

Figure 2.4 shows the flow field from the VITS simulation in terms of vorticity, for two airfoils before, at, and after the time of crossing at a flight condition of M = 0.25, α = 9.8°, and S/c = 4.0 (S = 2.0 ft, c = 0.5 ft). To simplify the problem, downwash was not modeled for this simulation, but will be explored using OVERFLOW in a later section. As the two airfoils approach each other the surrounding flow field of each airfoil begin to interact. The interaction causes a symmetrical flow field before, at, and after time of

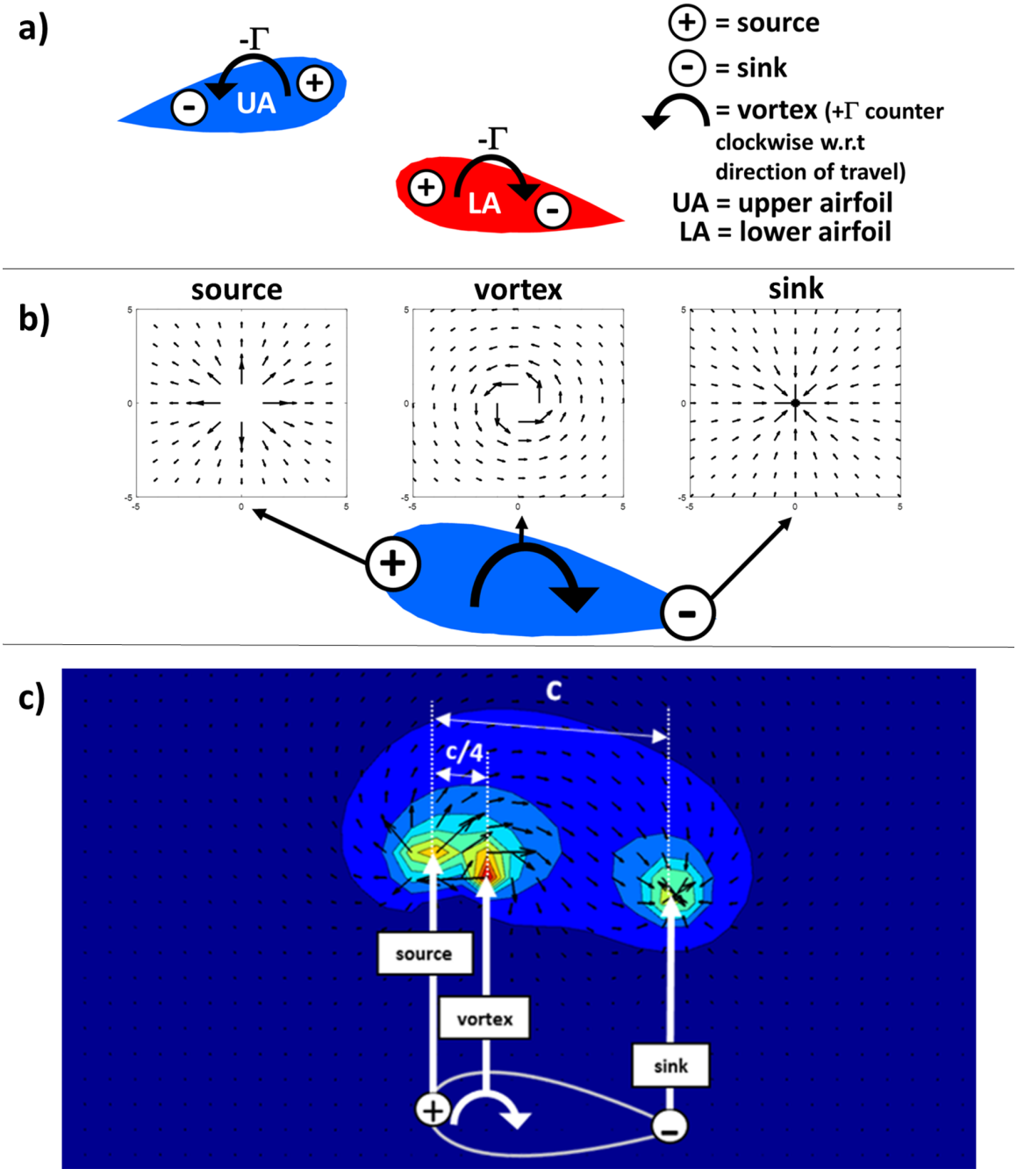

Figure 2.2: a) Pictorial representation of two airfoils moving past each other modeled by a source, sink, and vortex, b) mathematical model of an individual sink, vortex, and source and c) simulation of a combined sink, vortex, and source for an isolated airfoil.

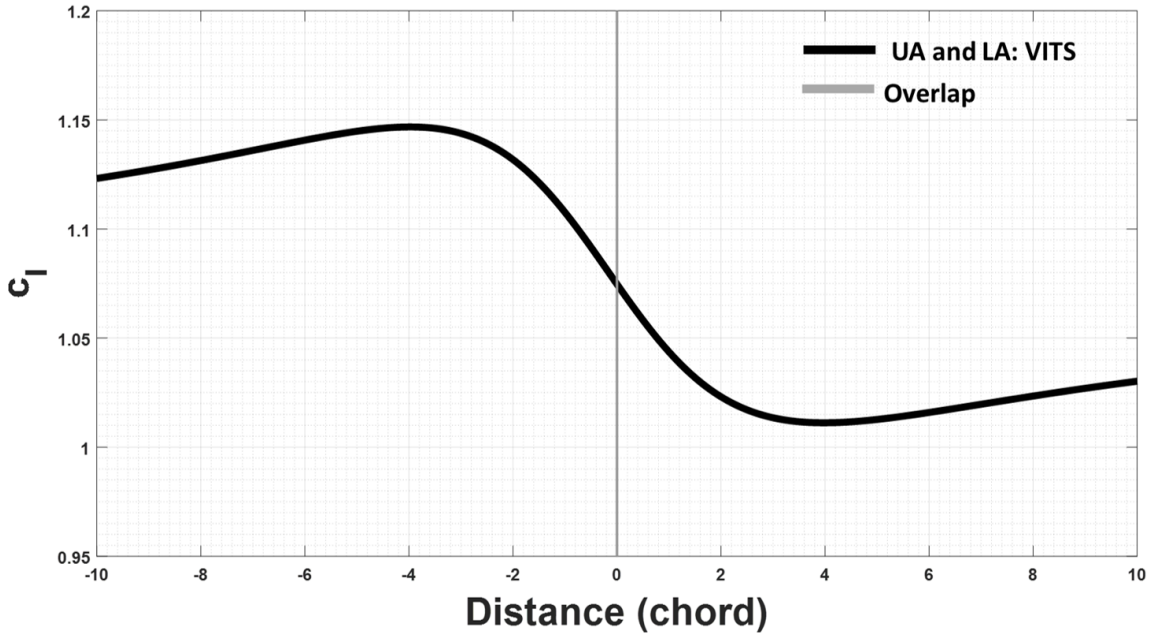

Figure 2.3: VITS simulation of two airfoils crossing, c_l versus distance to overlap in chords (M = 0.25, α = 9.8°, and S/c = 4.0 (S = 2.0 ft, c = 0.5 ft)).

overlap due to the absence of viscosity, resulting in an equal and opposite change in lift for the upper and lower airfoil. The resultant time history of the change in angle-of-attack (or lift) and induced velocity is visually explained in Fig. 2.5. When compressibility is not dominating, the lift of both the upper and lower airfoil increase before the overlap, followed by a decrease in lift after the overlap. Before the overlap, the upper airfoil sees an increase in angle-of-attack due to the upwash from the lower airfoil. The angle-of-attack of the lower airfoil also increases due to the upwash from the upper airfoil. Therefore an increase in lift is experienced by both airfoils as depicted in Fig. 2.5 a). The opposite occurs after the time of the overlap, where the lift for both the upper and lower airfoils (see Fig. 2.5 b)) decreases. As the airfoils approach one another, c_l of each airfoil changes due to the circulation effect of the other airfoil. A compressible flow solver is needed to further investigate the effects of viscosity, circulation, thickness, compressibility, downwash, and shed vorticity.

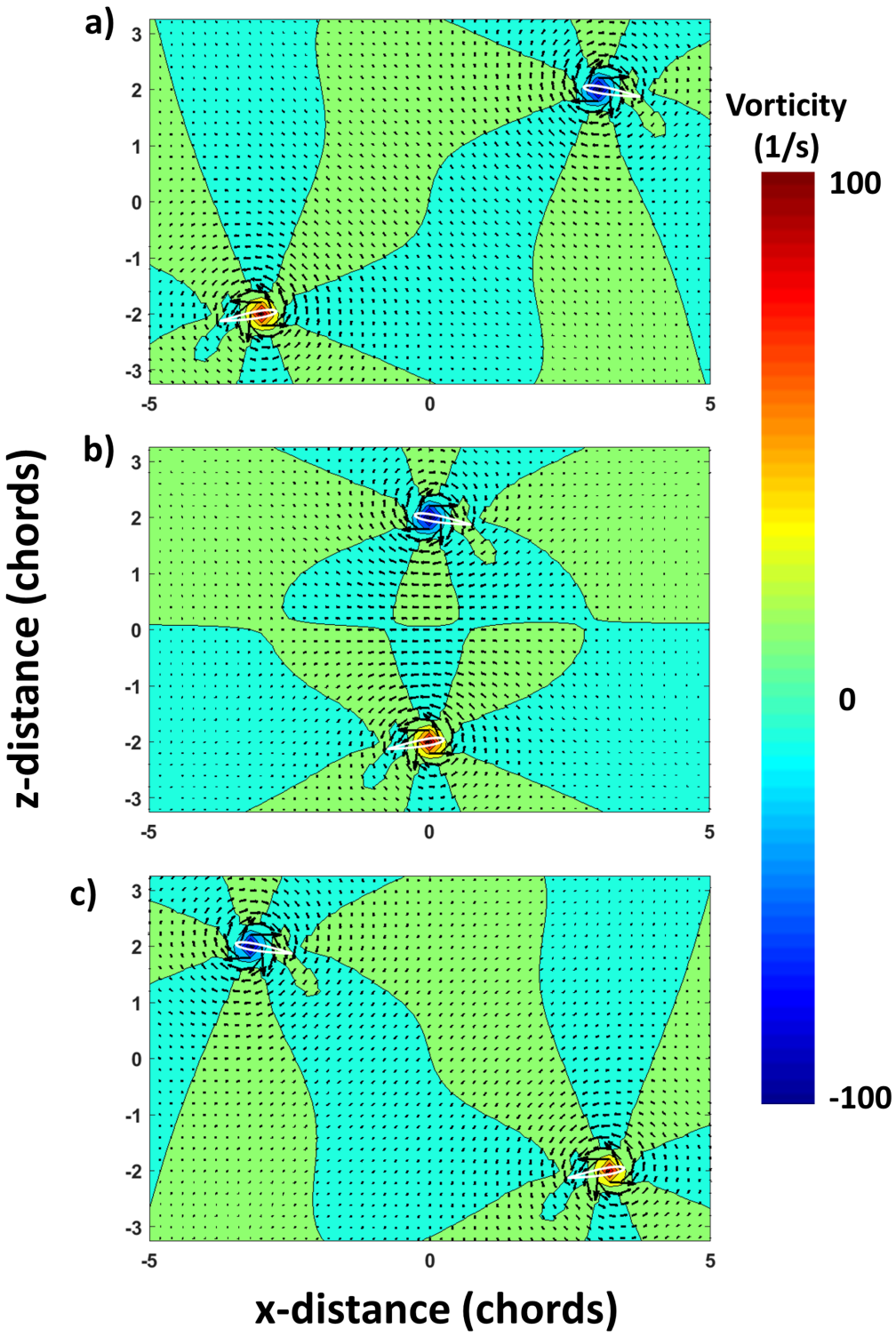

Figure 2.4: Simulation of two airfoils: a) before, b) at, and c) after time of crossing. Vorticity contour shown with u and v velocity vectors, downwash not simulated. (M = 0.25, α = 9.8°, and S/c = 4.0 (S = 2.0 ft, c = 0.5 ft)).

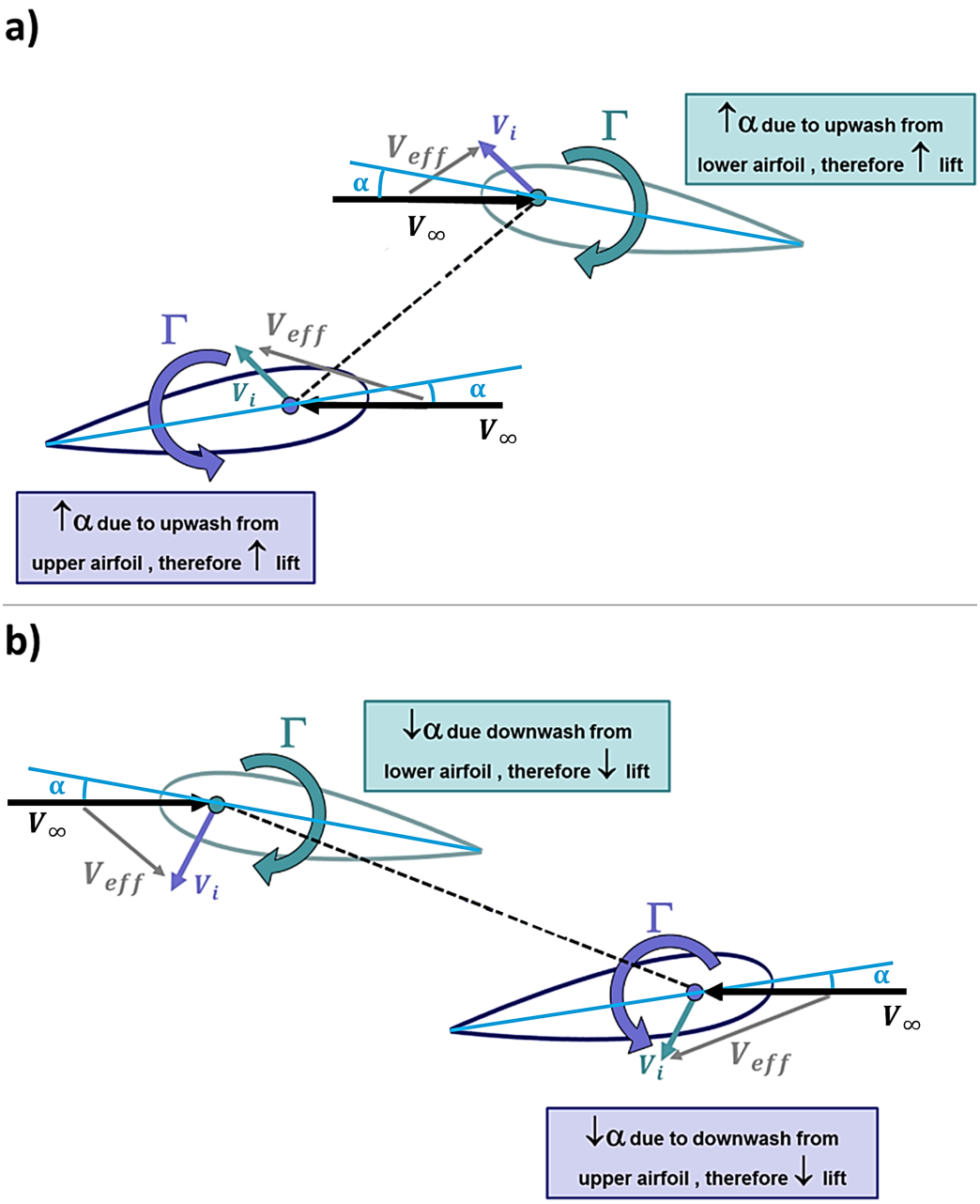

Figure 2.5: Change in lift of two NACA 0012 (when compressibility is not dominating) airfoils crossing: a) before and b) after.

2.3 Incompressible and compressible flow simulation

To capture all aerodynamic effects of a coaxial rotor in 2D, a compressible Reynolds-Averaged Navier-Stokes solver was used to further investigate the aerodynamic sources. The computational set up, along with a detailed description of the solver is discussed next. Initial calculations included Mach number variation of an isolated airfoil. Simulations of two airfoils crossing with variation of angle-of-attack, separation distance, Mach number, and airfoil thickness were compared to understand effects due to thickness, circulation, and compressibility. Furthermore, an isolated airfoil, two airfoils crossing, a single train of eight airfoils, and two trains of eight airfoils traveling in opposite directions were simulated to understand effects due to downwash and shed vorticity. Inviscid and viscid calculations were performed to help isolate the effects of downwash and shed vorticity.

2.3.1 Computational set up

The computational tool OVERFLOW 2.2k was selected due to availability and reputation to accurately calculate complex flow field phenomena [60]. The improved computational tool aids in computing more precise, and compressible flow field calculations.

OVERFLOW 2.2k

OVERFLOW 2.2k [60], developed by NASA, is a compressible Reynolds-Averaged Navier-Stokes CFD analysis tool that uses structured, overset grids. This study used OVERFLOWs 2D configuration to model airfoils moving through a static background mesh. Over the course of the simulation, these airfoil(s) moved horizontally toward the origin at a speed representative of the tip speed of the coaxial rotor design. At the origin they passed by each other to model a blade passage or overlap. The upper airfoil(s) were initially displaced 200 chord lengths to the right of the origin while the lower airfoils were initially displaced 200 chord lengths to the left of the origin. This distance was chosen to give the flow sufficient

time to reach a steady state before the airfoil grids reached the origin, where aerodynamic forces were constant over time. The airfoils were also displaced from the origin in the vertical direction by a distance that represented the rotor-rotor separation for the given coaxial design. This vertical separation was held constant for the entire simulation.

OVERFLOW 2.2k offers a wide variety of numerical schemes, turbulence models, and boundary conditions. All simulations in this study used a 5th-order accurate central difference spatial scheme with an ARC3D diagonalized Beam-Warming scalar pentadiagonal scheme for the left hand side. Time marching was performed using a 2nd-order dual time-stepping scheme. Turbulence was modeled using the Spalart-Allmaras one equation turbulence model. Airfoil surfaces were modeled as viscous, adiabatic walls, and the edges of the computational domain were modeled using a characteristic condition that imposed a quiescent freestream at standard atmospheric conditions. A physical time step was chosen such that the airfoils moved 1/200th of a chord length for each time step. Each physical time step included ten dual-time sub-iterations. These values ensured that sub-iteration convergence met or exceeded two orders of decrease in the residual at all times.

Airfoils were modeled using a set of identical body fitted, curvilinear structured grids. These grids were of an O-topology with 253 points around each airfoil and 65 points normal to the airfoil surface. The $y+$ value at the first point off the airfoil surface was less than one. These airfoil grids moved through a Cartesian background mesh that extended 1200 chords from the origin in the horizontal and vertical direction. Background grids can be refined based on an estimate of the solution error using overlapping Cartesian refinement grids (see Fig. 2.6). This grid adaption scheme ensured sufficient grid support for shed vorticity in the wake of the airfoils. All grids were modeled in 2D. Total grid sizes ranged from approximately 350,000 points for an isolated airfoil before grid adaption to approximately 11 million for an eight airfoil simulation after grid adaption.

Forces and moments exerted on the airfoils were integrated from the pressure and viscous stress at the airfoil surface. These quantities were integrated and recorded periodically

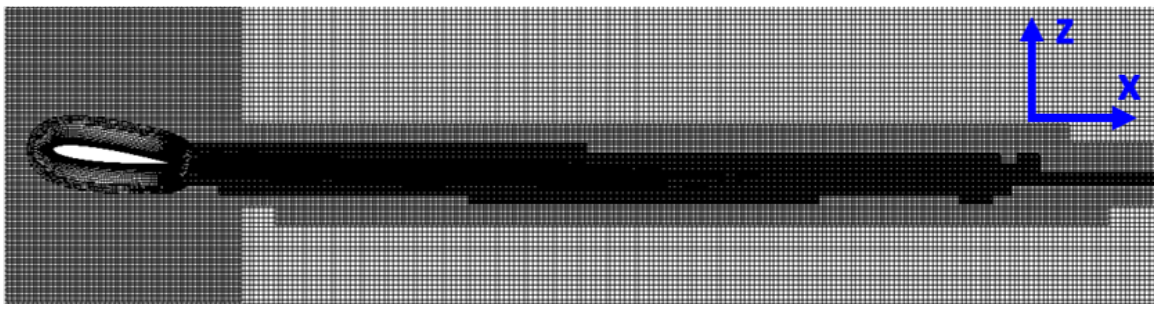

Figure 2.6: OVERFLOW 2.2k simulation with grid adaption for an NACA 0012 isolated airfoil at α = 7°.

Table 2.1: Atmospheric conditions for 2D OVERFLOW simulations.

Variable	Value	Units
pressure	2,118.17	(lb_f/ft^2)
viscosity	3.737x10^{-7} (viscous)	(slug/(s-ft))
density	0.002377	(slug/ft^3)
temperature	518.7	(R°)
speed of sound	1,116.46	(ft/s)

over the entire course of the simulation. The force in the vertical, z, direction is positive up and is equivalent to aerodynamic lift. The coefficient of z-force is abbreviated as c_z. The direction of force in the horizontal, x, direction is positive toward the airfoils trailing edge and is equivalent to aerodynamic drag. The coefficient of x-force is abbreviated by c_x. The coordinate system origin is located at the quarter chord of the airfoil, where the x direction is positive toward the airfoils trailing edge and the z direction is positive up. Atmospheric conditions for all 2D OVERFLOW simulations are shown in Table 2.1.

2.3.2 Simulation set up

In order to understand the effects due to circulation, thickness, compressibility, shed vorticity, and downwash (inflow), multiple simulations were performed to study the effects independently. A complete pictorial list of different types of simulations performed are shown in Fig. 2.7.

A viscid isolated airfoil was first simulated for a Mach number sweep as shown in

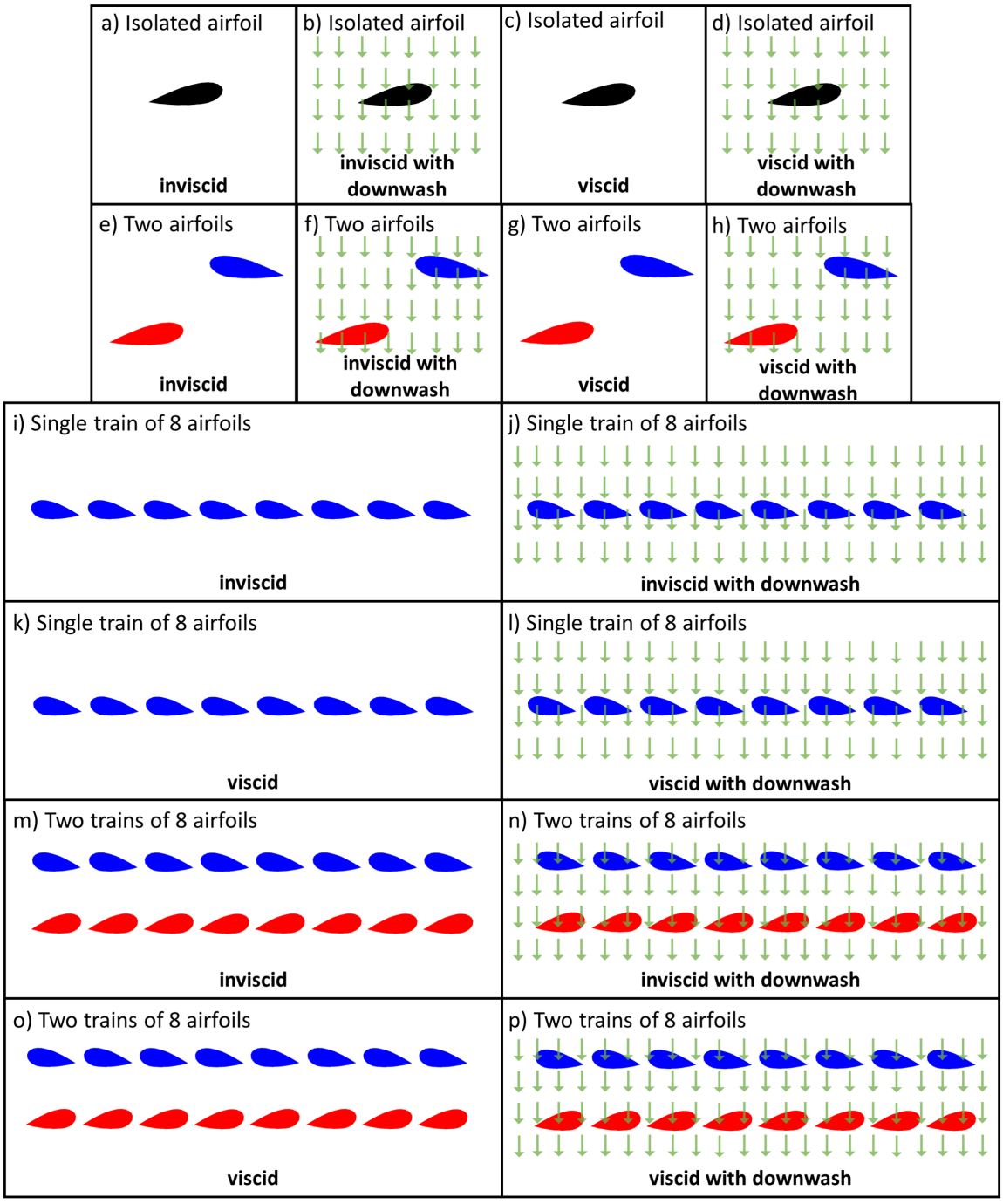

Figure 2.7: Inviscid and viscid simulations of an isolated airfoil (a) through d)), two airfoils crossing (e) through h)), train of eight airfoils (i) through l)), and two trains of eight airfoils crossing (m) through p)).

Fig. 2.7 c) to understand OVERFLOW settings and grid resolution. To explore effects due to circulation, thickness and compressibility, two viscid airfoils crossing in opposite directions were simulated, as shown in Fig. 2.7 g). An inviscid and viscous isolated airfoil were simulated and compared to understand the effect of viscous flow (Figs. 2.7 a) and c)). Downwash was simulated for both the inviscid and viscid isolated airfoil case to understand independent effects on a single airfoil for inflow (Figs. 2.7 b) and d)). Inviscid and viscid cases of two airfoils traveling in opposite directions were simulated to represent blade crossing of a coaxial rotor (Figs. 2.7 e) and g)). Due to the presence of the inflow, downwash was applied for both the inviscid and viscid cases (Figs. 2.7 f) and h)). The effects due to shed vorticity were simulated by a single train of eight airfoils for both inviscid and viscous cases (Figs. 2.7 i) and k)). Downwash was simulated in the single train of eight airfoils for the inviscid and viscous case (Figs. 2.7 j) and l)). Two trains of eight airfoils traveling in opposite directions were simulated to represent a coaxial rotor for an inviscid and viscous case (Figs. 2.7 m) and o)). Downwash was simulated in the two trains of eight airfoils to model the inflow for both the inviscid and viscid case (Figs. 2.7 n) and p)). A pictorial of all shed vorticity simulations are shown in Figs. 2.7 i), j), k), l) m), n), o), and p).

As previously mentioned in Chapter 1, Harrington coaxial rotor 1 (HC1) was tested in a wind tunnel and the results have been used by many as a validation case [13]. For this study, a configuration was introduced that is representative of modern coaxial systems [41], and previously modeled by Barbely et al. [27, 28, 29]. The modern coaxial rotor design has three blades per rotor, a smaller rotor-rotor vertical separation distance, and faster tip speed compared to the HC1. Table 2.2 shows HC1 and modern coaxial rotor design parameters and the 2D analog.

The downwash was simulated by introducing a vertical velocity everywhere as shown in Figs. 2.7 b), d), f), h), j), l), n), and p). The induced velocity (downwash) was calculated using a Blade Element Momentum Theory (BEMT) hover model for the modern rotor

Table 2.2: Simulated rotor design parameters 3D and 2D analog.

2D rotor tip parameter	HC1	Modern	**Coaxial rotor parameter**	HC1	Modern
R, Radius (ft)	N/A	N/A	R, Radius (ft)	12.5	20
No. of airfoils (per train)	8	8	No. of blades (per rotor)	2	3
S, vertical separation between airfoils (ft)	2.33	2	S, rotor separation (ft)	2.33	2
D, horizontal separation between airfoils (ft)	39.27	41.9	D, horizontal separation (ft)	N/A	N/A
c, chord (ft)	0.375	0.5	c, chord (ft)	varying	0.5
Airfoil speed (ft/s)	500	700	V_{tip}, hover (ft/s)	500	700
M, Mach number	0.47	0.627	M, Mach number (M_{tip} for hover)	0.47	0.627
θ_{tw}, Linear twist (deg)	N/A N/A	N/A N/A	θ_{tw}, Linear twist (deg)	0	-8
α (deg)	7	5	α (deg)	N/A	N/A
θ_0 (deg)	N/A	N/A	θ_0 (deg)	7	0
Airfoils	NACA 0012	NACA 0012	Airfoils	varying	NACA 0012

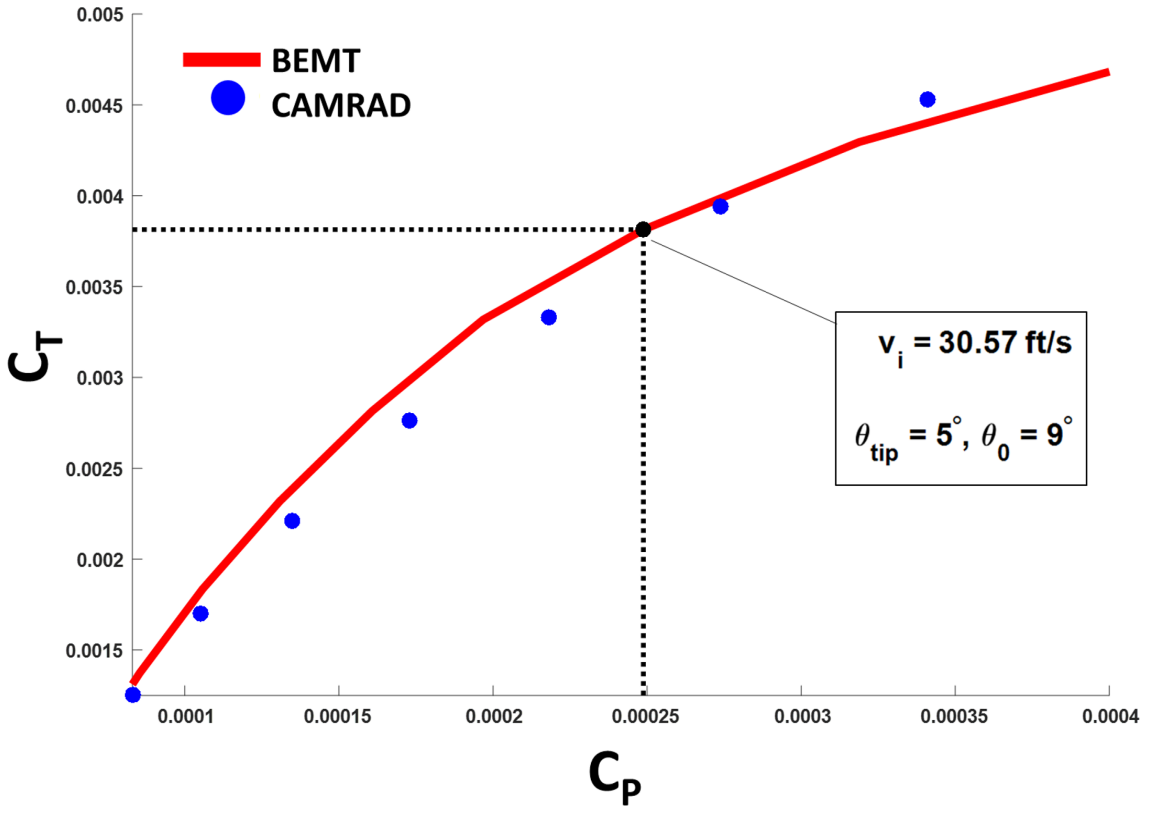

Figure 2.8: Coefficient of thrust versus coefficient of power for modern coaxial rotor in hover.

design as shown in Table 2.2. The results from the BEMT hover model were then compared to CAMRAD [61] as shown in Fig. 2.8. The BEMT uses a coaxial interference-induced power factor from Leishman's Case 4a [12]. Leishman's Case 4a assumes that the rotors have balanced torque with the lower rotor operating in the slipstream of the upper rotor. The BEMT uses a C81 table and interpolates to find the correct C_l and C_d for the various span locations. For all downwash simulations, an induced velocity (V_i) of 31 ft/s was used from the modern rotor design BEMT results.

Simulation test conditions

Along with the various simulation set ups, test conditions were varied to understand the effects of changing angle-of-attack (α), Mach number (M), airfoil thickness (NACA 0001/NACA

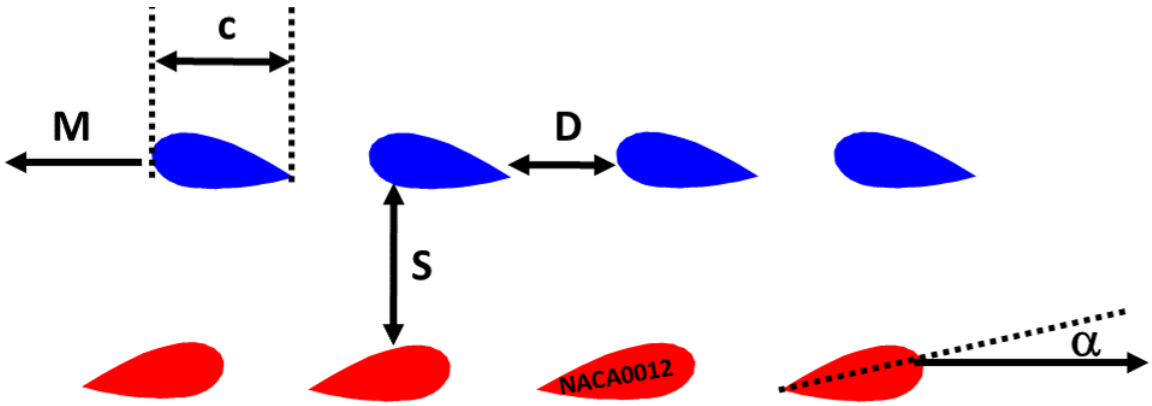

Figure 2.9: Simulated test condition variables.

Table 2.3: List of isolated airfoil OVERFLOW simulations.

Airfoil	M	S/c	D/c	$\alpha(^\circ)$	V_i (ft/s)	$Re\ \#$
NACA 0012*	0.25	N/A	N/A	9.8	31	8.90×10^5
NACA 0012*	0.25	N/A	N/A	9.8	0	8.90×10^5
NACA 0012	0.10	N/A	N/A	7.0	0	3.60×10^5
NACA 0012	0.20	N/A	N/A	7.0	0	7.10×10^5
NACA 0012	0.30	N/A	N/A	7.0	0	1.10×10^6
NACA 0012	0.40	N/A	N/A	7.0	0	1.40×10^6
NACA 0012	0.50	N/A	N/A	7.0	0	1.80×10^6
NACA 0012	0.60	N/A	N/A	7.0	0	2.10×10^6
NACA 0012	0.70	N/A	N/A	7.0	0	2.50×10^6
NACA 0012	0.75	N/A	N/A	7.0	0	2.70×10^6
NACA 0012	0.80	N/A	N/A	7.0	0	2.80×10^6
NACA 0012	0.90	N/A	N/A	7.0	0	3.20×10^6
NACA 0012	1.00	N/A	N/A	7.0	0	3.60×10^6
NACA 0012	1.10	N/A	N/A	7.0	0	3.90×10^6

0012), vertical separation distance (S) and horizontal separation distance (D)-see Fig. 2.9. Tables 2.3 through 2.6 provides a complete list of simulations for an isolated airfoil, two airfoils crossing, a single train of eight airfoils, and two trains of eight airfoils crossing. In Tables 2.3 through 2.6, a '*' represents calculations performed inviscid and viscid, and simulations without a '*' represent viscid calculations only.

Table 2.4: List of two airfoils crossing OVERFLOW simulations.

Airfoil	M	S/c	D/c	$\alpha(^\circ)$	V_i (ft/s)	$Re\ \#$
NACA 0012*	0.25	4	N/A	9.8	31	8.90×10^5
NACA 0012*	0.25	4	N/A	9.8	0	8.90×10^5
NACA 0012	0.50	4	N/A	-7.0	0	1.80×10^6
NACA 0012	0.50	4	N/A	0.0	0	1.80×10^6
NACA 0012	0.50	4	N/A	7.0	0	1.80×10^6
NACA 0012	0.90	4	N/A	-7.0	0	3.20×10^6
NACA 0012	0.90	4	N/A	0.0	0	3.20×10^6
NACA 0012	0.90	4	N/A	7.0	0	3.20×10^6
NACA 0012	0.50	2	N/A	7.0	0	1.80×10^6
NACA 0012	0.50	4	N/A	7.0	0	1.80×10^6
NACA 0012	0.50	6	N/A	7.0	0	1.80×10^6
NACA 0012	0.90	2	N/A	7.0	0	3.20×10^6
NACA 0012	0.90	4	N/A	7.0	0	3.20×10^6
NACA 0012	0.90	6	N/A	7.0	0	3.20×10^6
NACA 0012	0.20	4	N/A	0.0	0	7.10×10^5
NACA 0012	0.50	4	N/A	0.0	0	1.80×10^6
NACA 0012	0.70	4	N/A	0.0	0	2.50×10^6
NACA 0012	0.90	4	N/A	0.0	0	3.20×10^6
NACA 0012	1.00	4	N/A	0.0	0	3.60×10^6
NACA 0012	1.20	4	N/A	0.0	0	4.30×10^6
NACA 0012	0.50	4	N/A	0.0	0	1.80×10^6
NACA 0001	0.50	4	N/A	0.0	0	1.80×10^6
NACA 0012	0.90	4	N/A	0.0	0	3.20×10^6
NACA 0001	0.90	4	N/A	0.0	0	3.20×10^6
NACA 0012	0.50	4	N/A	3.0	0	1.80×10^6
NACA 0001	0.50	4	N/A	3.0	0	1.80×10^6
NACA 0012	0.90	4	N/A	3.0	0	3.20×10^6
NACA 0001	0.90	4	N/A	3.0	0	3.20×10^6

Table 2.5: List of single train of eight airfoils OVERFLOW simulations.

Airfoil	M	S/c	D/c	$\alpha(^\circ)$	V_i (ft/s)	$Re\ \#$
NACA 0012	0.08	N/A	11.14	11.9	0	3.00×10^5
NACA 0012	0.16	N/A	20.94	11.0	0	5.60×10^5
NACA 0012*	0.25	N/A	33.51	9.8	0	8.90×10^5
NACA 0012	0.31	N/A	41.89	9.0	0	1.10×10^6
NACA 0012	0.38	N/A	50.27	8.2	0	1.30×10^6
NACA 0012	0.47	N/A	62.83	7.0	0	1.70×10^6
NACA 0012	0.50	N/A	67.02	6.6	0	1.80×10^6
NACA 0012	0.53	N/A	71.21	6.2	0	1.90×10^6
NACA 0012	0.56	N/A	75.40	5.8	0	2.00×10^6
NACA 0012	0.60	N/A	79.59	5.4	0	2.10×10^6
NACA 0012	0.63	N/A	83.78	5.0	0	2.20×10^6

Table 2.6: List of two trains of eight airfoils OVERFLOW simulations.

Airfoil	M	S/c	D/c	$\alpha(^\circ)$	V_i (ft/s)	$Re\ \#$
NACA 0012	0.08	4	11.14	11.9	31	3.00×10^5
NACA 0012	0.16	4	20.94	11.0	31	5.60×10^5
NACA 0012*	0.25	4	33.51	9.8	31	8.90×10^5
NACA 0012	0.31	4	41.89	9.0	31	1.10×10^6
NACA 0012	0.38	4	50.27	8.2	31	1.30×10^6
NACA 0012	0.47	4	62.83	7.0	31	1.70×10^6
NACA 0012	0.50	4	67.02	6.6	31	1.80×10^6
NACA 0012	0.53	4	71.21	6.2	31	1.90×10^6
NACA 0012	0.56	4	75.40	5.8	31	2.00×10^6
NACA 0012	0.60	4	79.59	5.4	31	2.10×10^6
NACA 0012	0.63	4	83.78	5.0	31	2.20×10^6

2.3.3 Isolated airfoil Mach sweep

A Mach number sweep simulation was performed for Mach 0.10, 0.20, 0.30, 0.40, 0.50, 0.60, 0.70, 0.75, 0.80, 0.90, 1.00, and 1.10 for a viscid isolated NACA 0012 airfoil at α = 7° with a chord of 0.50 ft (Tables 2.3). Figure 2.10 a) shows the variation with Mach number for c_l and c_d. Figure 2.10 b) shows C_P versus non-dimensional chord (x/c) for the same Mach number range. Coefficient of pressure (C_P) contours of the flow field of the isolated airfoil for M = a) 0.10, b) 0.30, c) 0.50, d) 0.60, e) 0.70, f) 0.80, g) 0.90, h) 1.0, and i) 1.1 is shown in Fig. 2.11.

An increase in c_d with increasing Mach number was observed in Fig. 2.10 a) which is due to shocks and viscous forces increasing with Mach number [59]. As shocks move toward the trailing edge, the drag decreases due to the trailing edge shocks weakening.

From Mach 0.10 to 0.50, an increase in c_l was observed. From Mach 0.50 to 0.80 a decrease in c_l is observed in Fig. 2.10 a); this decrease in c_l is because flow is supersonic over most of the lower surface and decelerated to subsonic speeds through a shock wave at the trailing edge, so lower surface pressures are lower than before Mach 0.50. The location of the shock wave can be determined from Fig. 2.10 b). For example, at Mach 0.80 and 0.90, the shock was at x/c = 0.35 and 0.90, respectively. The formation of a shock wave on the upper surface became more apparent from the C_P behavior, as shown in Fig. 2.10 b) and Fig. 2.11 in comparison to Fig. 2.10 a). As the Mach number increased further to 0.90, c_l increased due to the upper surface shock wave moving to the trailing edge, where the local Mach number was supersonic for most of the airfoil [59]. Beyond, Mach 1.0, the upper and lower shock have moved to the tail, creating fish tail of shocks.

2.3.4 Two airfoils crossing: circulation, thickness, and compressibility effects

The effects due to circulation, thickness, and compressibility for a coaxial rotor blade crossing occurrence were simulated by two airfoils, separated vertically, traveling in opposite directions. The time of overlap is when the quarter-chord of each airfoil overlap. Due to

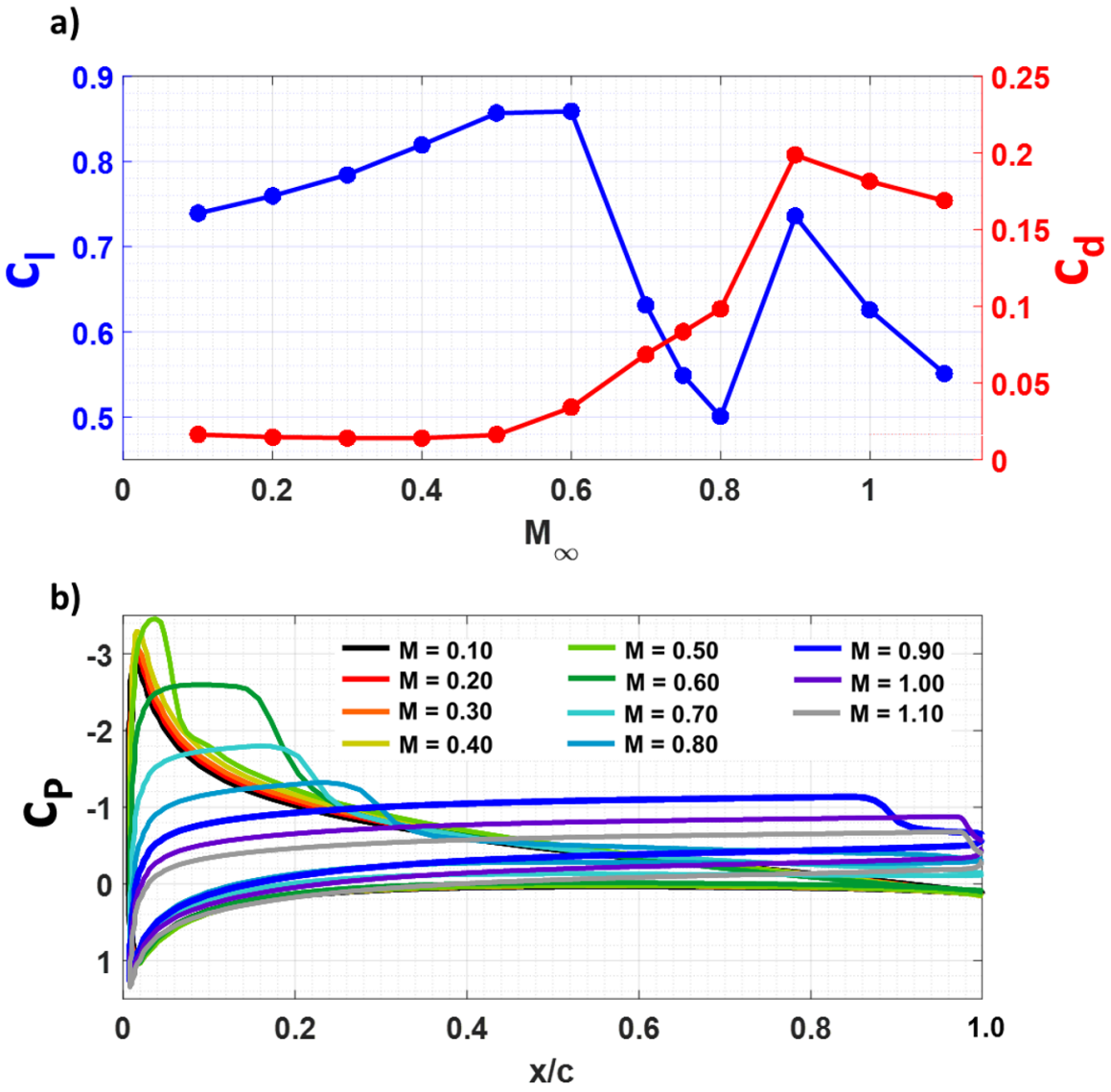

Figure 2.10: Viscid isolated NACA 0012 airfoil at α = 7° with a chord of 0.50 ft Mach number variation for a) c_l and c_d and b) C_P versus x/c.

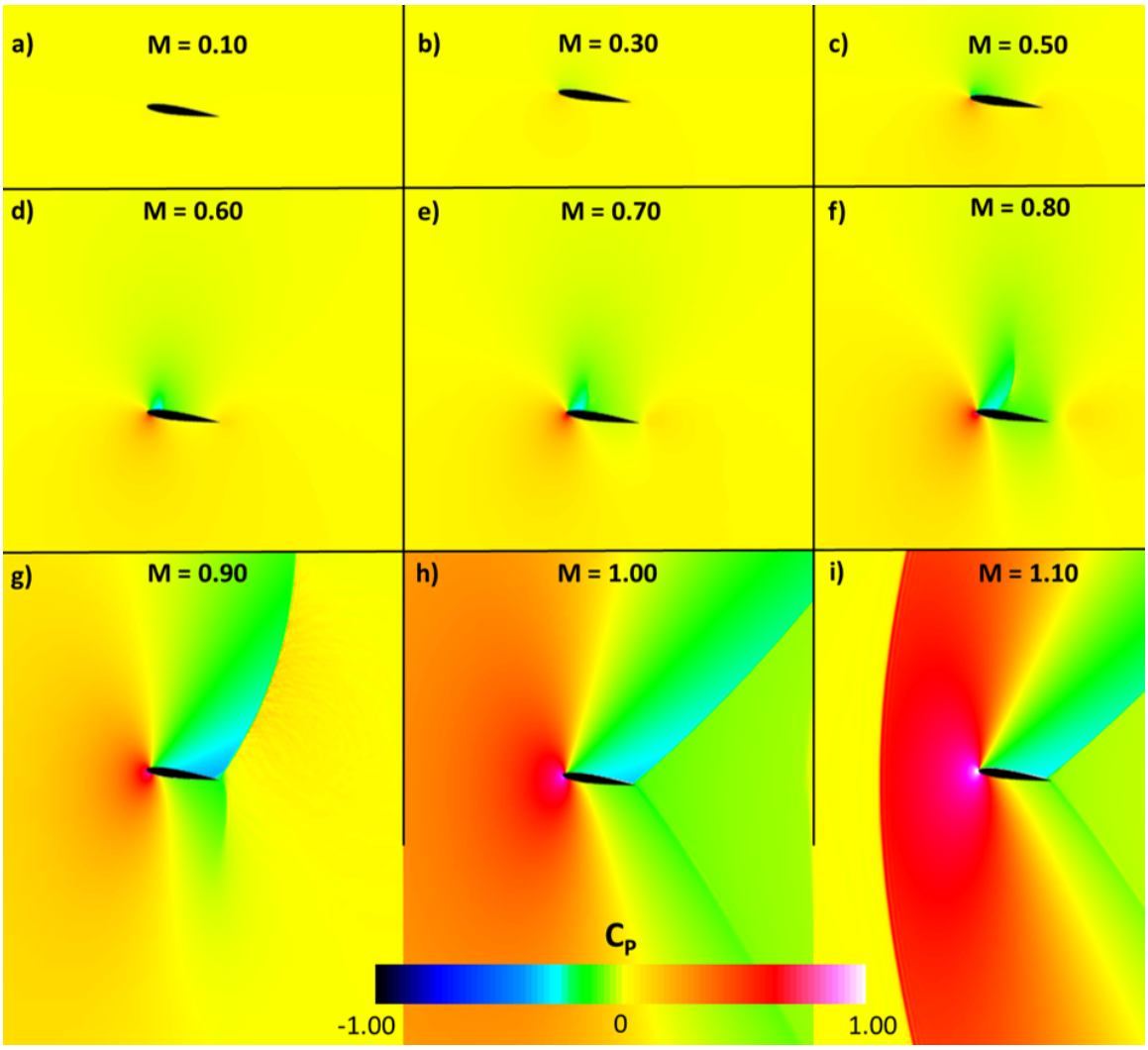

Figure 2.11: C_P flow field contours for Mach number variation for an isolated NACA 0012 airfoil at α = 7° M = a) 0.10, b) 0.30, c) 0.50, d) 0.60, e) 0.70, f) 0.80, g) 0.90, h) 1.0, and i) 1.1

the change in angle-of-attack at time of crossing, the notation c_l and c_d can not be used. The c_z is the force in the vertical direction at quarter-chord, while c_x is the force in the horizontal direction at quarter-chord. In general, c_l and c_d are in the wind axis, so the force direction changes based on angle-of-attack, whereas within OVERFLOW the vertical and horizontal force vectors are fixed (c_z and c_x). Various conditions were simulated for two airfoils crossing, each with a chord (c) of 0.5 feet.

Two airfoils crossing: circulation

Effects due to circulation are caused by changes in the measure of rotation for a finite area of fluid. A change in α will result in a change in circulation. To isolate effects due to circulation, airfoil thickness, separation distance, and Mach number were held constant.

For two NACA 0012 airfoils crossing at M = 0.50 and S/c = 4.0, angles-of-attack equal to -7°, 0° and 7° were simulated (see Figs. 2.12). An α of -7° and 7° show an equal and opposite result for c_z and c_m, while for c_x results are equal. Minimum change between the upper and lower airfoil in c_z, c_x, and c_m is shown for α = 0° compared to α = -7° and 7°, which reveals that effects due to circulation are significant.

The similar comparisons were made for M = 0.90. Figure 2.13 shows two NACA 0012 airfoils crossing at M = 0.90, S/c = 4.0, for angles-of-attack of -7°, 0° and 7°. As shown for the low-speed case, an α of -7° and 7° show an almost equal and opposite result for c_z and c_m, while for c_x results are equal. Large differences between the two speed cases could be due to compressibility effects.

Two airfoils crossing: thickness

Thickness effects are caused by the displacement of flow due to the geometry of the body and location of bodies relative to each other. To isolate effects due to thickness, a NACA 0001 and NACA 0012 were compared for 0° and 3° angle-of-attack for a low- and high-speed condition, while keeping all other variables constant. The NACA 0001 is used to

Table 2.7: Conditions for 2D OVERFLOW simulations for two airfoils crossing.

Airfoil	M	S (ft)	S/c	$\alpha(^\circ)$	Re #
Low-speed: α variation					
NACA 0012	0.5	2	4	-7	1.78×10^6
NACA 0012	0.5	2	4	0	1.78×10^6
NACA 0012	0.5	2	4	7	1.78×10^6
High-speed: α variation					
NACA 0012	0.9	2	4	-7	3.20×10^6
NACA 0012	0.9	2	4	0	3.20×10^6
NACA 0012	0.9	2	4	7	3.20×10^6
Low-speed: S variation					
NACA 0012	0.5	1	2	7	1.78×10^6
NACA 0012	0.5	2	4	7	1.78×10^6
NACA 0012	0.5	3	6	7	1.78×10^6
High-speed: S variation					
NACA 0012	0.9	1	2	7	3.20×10^6
NACA 0012	0.9	2	4	7	3.20×10^6
NACA 0012	0.9	3	6	7	3.20×10^6
Mach variation					
NACA 0012	0.2	2	4	0	7.10×10^5
NACA 0012	0.5	2	4	0	1.78×10^6
NACA 0012	0.7	2	4	0	2.49×10^6
NACA 0012	0.9	2	4	0	3.20×10^6
NACA 0012	1.0	2	4	0	3.55×10^6
NACA 0012	1.2	2	4	0	4.26×10^6
Low-speed: Airfoil variation, α = 0 $^\circ$					
NACA 0012	0.5	2	4	0	1.78×10^6
NACA 0001	0.5	2	4	0	1.78×10^6
High-speed: Airfoil variation, α = 0 $^\circ$					
NACA 0012	0.9	2	4	0	3.20×10^6
NACA 0001	0.9	2	4	0	3.20×10^6
Low-speed: Airfoil variation, α = 3 $^\circ$					
NACA 0012	0.5	2	4	0	1.78×10^6
NACA 0001	0.5	2	4	0	1.78×10^6
High-speed: Airfoil variation, α = 3 $^\circ$					
NACA 0012	0.9	2	4	3	3.20×10^6
NACA 0001	0.9	2	4	3	3.20×10^6

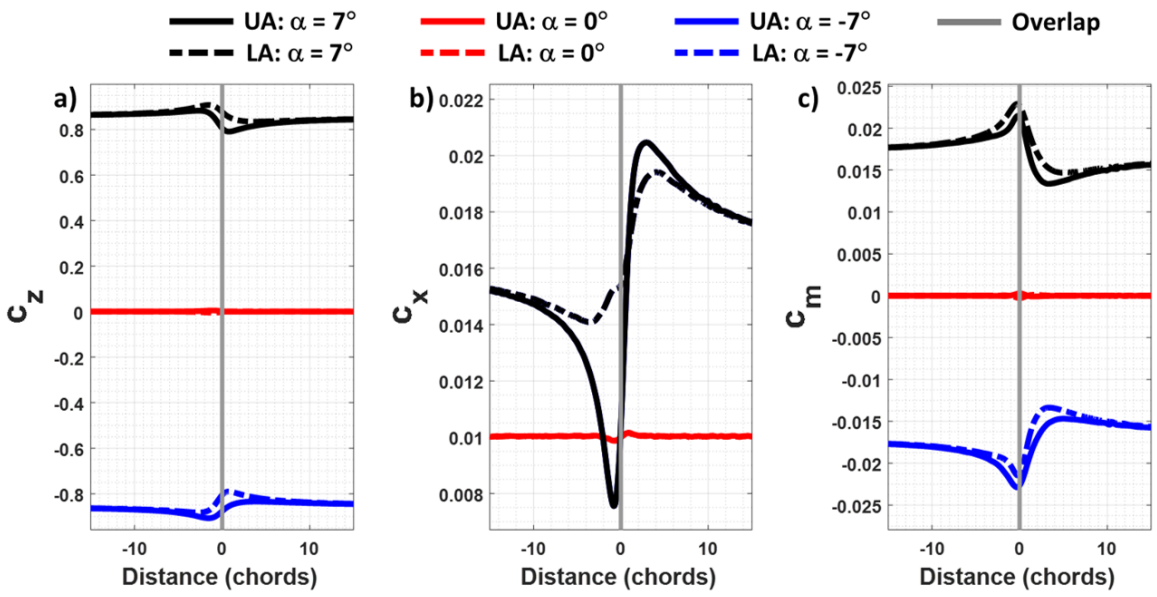

Figure 2.12: Two NACA 0012 airfoils crossing for a) c_z, b) c_x, and c) c_m versus distance to overlap (M = 0.5 (V_{tip} = 560 ft/s), α = -7°, 0°, and 7°, and S/c = 4.0 (S = 2.0 ft, c = 0.5 ft)).

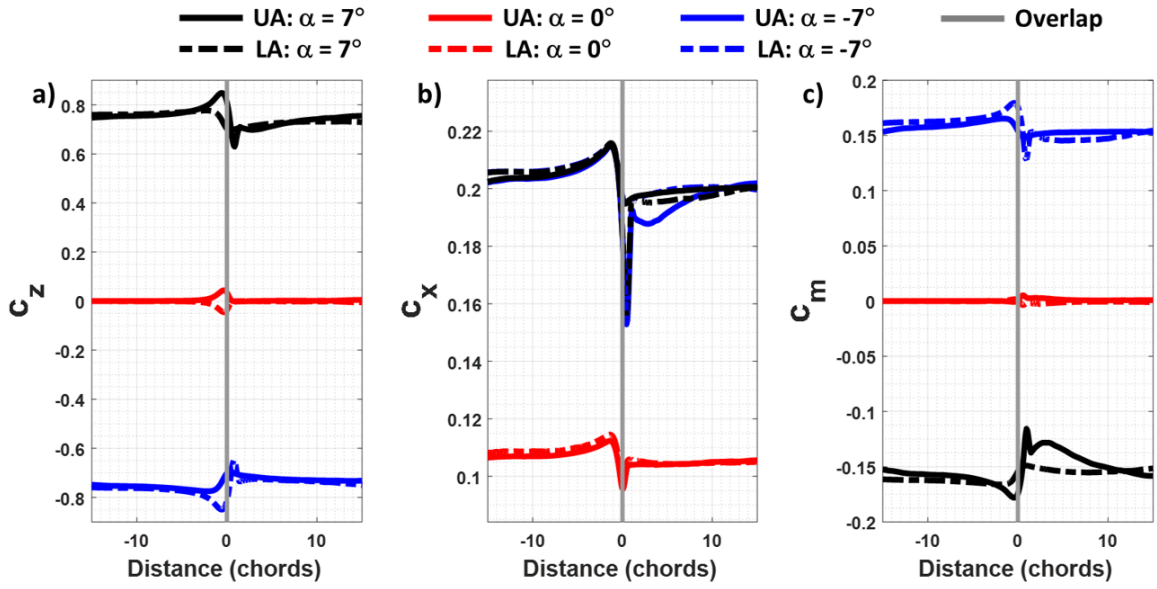

Figure 2.13: Two NACA 0012 airfoils crossing for a) c_z, b) c_x, and c) c_m versus distance to overlap (M = 0.9 (V_{tip} = 1,005 ft/s), α = -7°, 0°, and 7°, and S/c = 4.0 (S = 2.0 ft, c = 0.5 ft)).

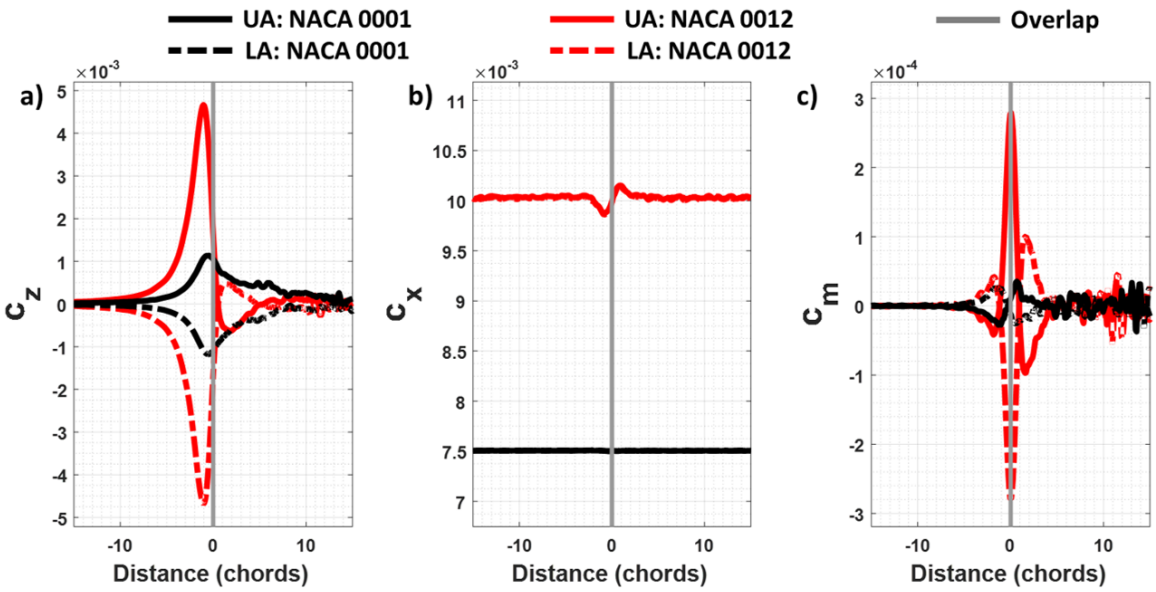

Figure 2.14: Comparison of two NACA 0001 and NACA 0012 airfoils crossing for a) c_z, b) c_x, and c) c_m versus distance to overlap (M = 0.5 (V_{tip} = 560 ft/s), α = 0°, and S/c = 4.0 (S = 2.0 ft, c = 0.5 ft)).

simulate a flat plate. A NACA 0012 is selected even though current modern day helicopters avoid thick airfoils, the NACA 0012 will represent an extreme geometry. Vertical separation distance between airfoils was varied for a low- and high-speed condition.

The c_z, c_x, and c_m of two NACA 0001 and two NACA 0012 airfoils crossing versus distance to overlap are shown in Fig. 2.14. The conditions for both airfoil calculation were M = 0.5 (V_{tip} = 560 ft/s), α = -7°, 0°, and 7°, and S/c = 4.0 (S = 2.0 ft, c = 0.5 ft). Although changes in c_z, c_x, and c_m are observed in Fig. 2.14 comparing the two airfoils, the magnitude of the aerodynamic forces for each airfoil is small. A similar comparison for the same airfoils but for α = 3° as shown in Fig. 2.16; for this case effects due to circulation dominate due to the increase in angle-of-attack. The aerodynamic forces shown in Fig. 2.14 are orders of magnitude fewer than the forces shown in Fig. 2.16, supporting the conclusion that circulation effects dominate thickness effects.

For a M = 0.90, a comparison of two NACA 0001 and two NACA 0012 airfoils crossing is shown in Fig. 2.15. As previously concluded from Fig. 2.14, minimal changes in c_z, c_x,

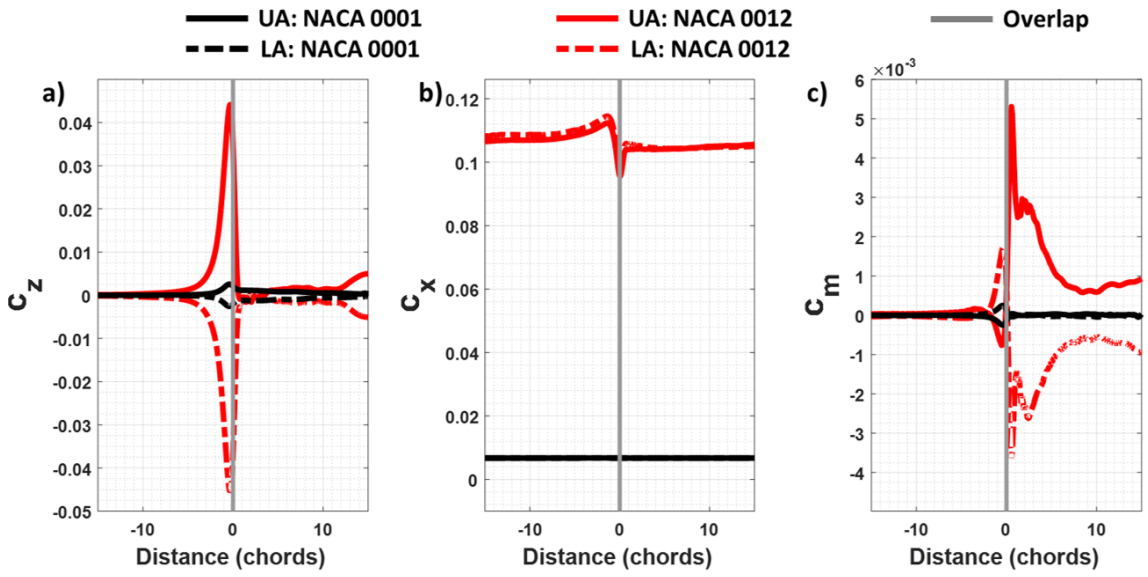

Figure 2.15: Comparison of two NACA 0001 and NACA 0012 airfoils crossing for a) c_z, b) c_x, and c) c_m versus distance to overlap (M = 0.9 (V_{tip} = 1,005 ft/s), α = 0°, and S/c = 4.0 (S = 2.0 ft, c = 0.5 ft)).

and c_m at time of overlap are observed due to thickness effects. Differences between the loads of the two speed cases are due to compressibility effects. A similar comparison is made for α = 3° (Fig. 2.17), where effects due to circulation and compressibility dominate.

Separation distance between airfoils was varied for two NACA 0012 airfoils crossing for M = 0.5 (V_{tip} = 560 ft/s) and α = 7°. Figure 2.18 shows results for S/c = 2.0, 4.0, and 6.0 (c = 0.5 ft)). An increase in S/c resulted in a decrease in c_z, c_x, and c_m in the interaction transient. For these cases, effects due to circulation (α = 7°) and airfoil thickness are present. The same comparison is made for a high-speed case (M = 0.9 (V_{tip} = 1,005 ft/s), as shown in Fig. 2.19.

Two airfoils crossing: compressibility

The magnitude of compressibility effects depends on Mach number. As the flow over an airfoil approaches Mach 1.0, the onset of shocks form. In order to explore effects due to compressibility, Mach number is varied for two airfoils traveling in opposite directions

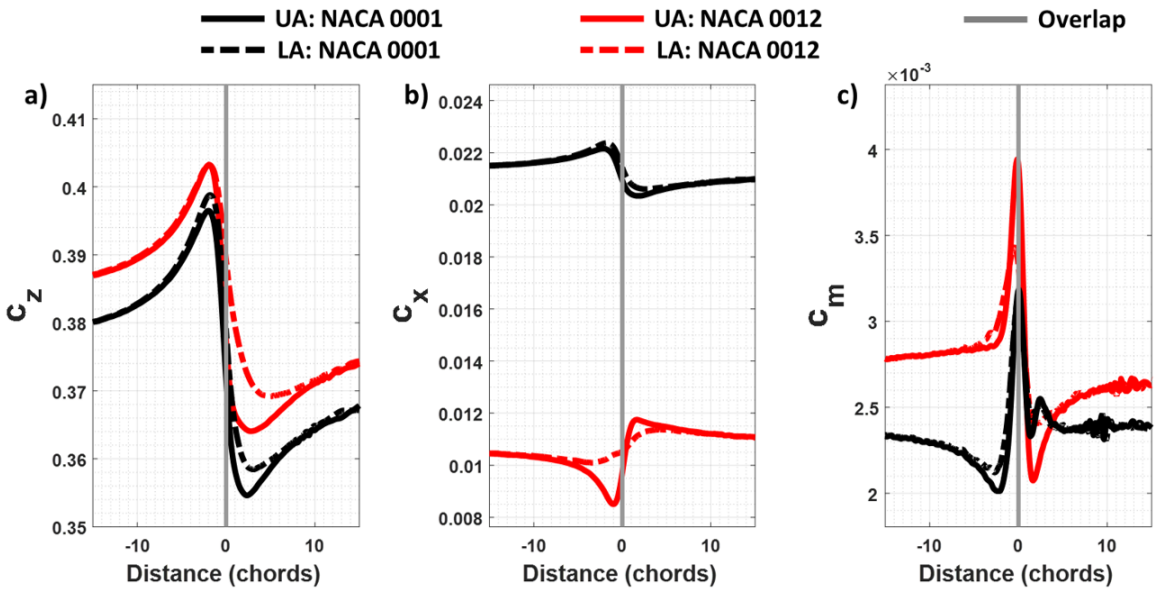

Figure 2.16: Comparison of two NACA 0001 and NACA 0012 airfoils crossing for a) c_z, b) c_x, and c) c_m versus distance to overlap (M = 0.5 (V_{tip} = 560 ft/s), α = 3°, and S/c = 4.0 (S = 2.0 ft, c = 0.5 ft)).

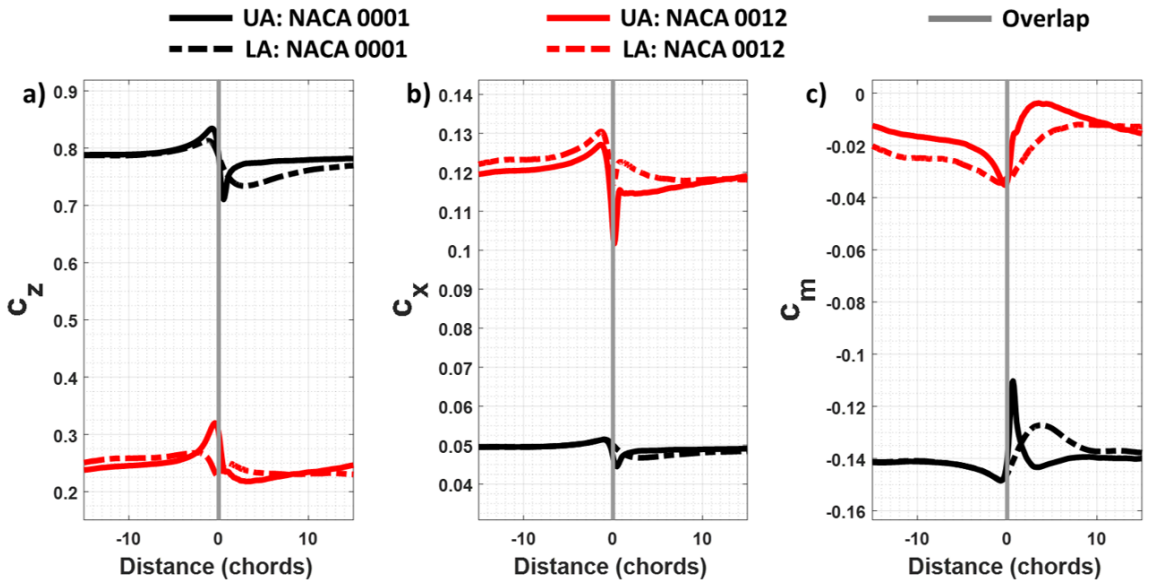

Figure 2.17: Comparison of two NACA 0001 and NACA 0012 airfoils crossing for a) c_z, b) c_x, and c) c_m versus distance to overlap (M = 0.9 (V_{tip} = 1,005 ft/s), α = 3°, and S/c = 4.0 (S = 2.0 ft, c = 0.5 ft)).

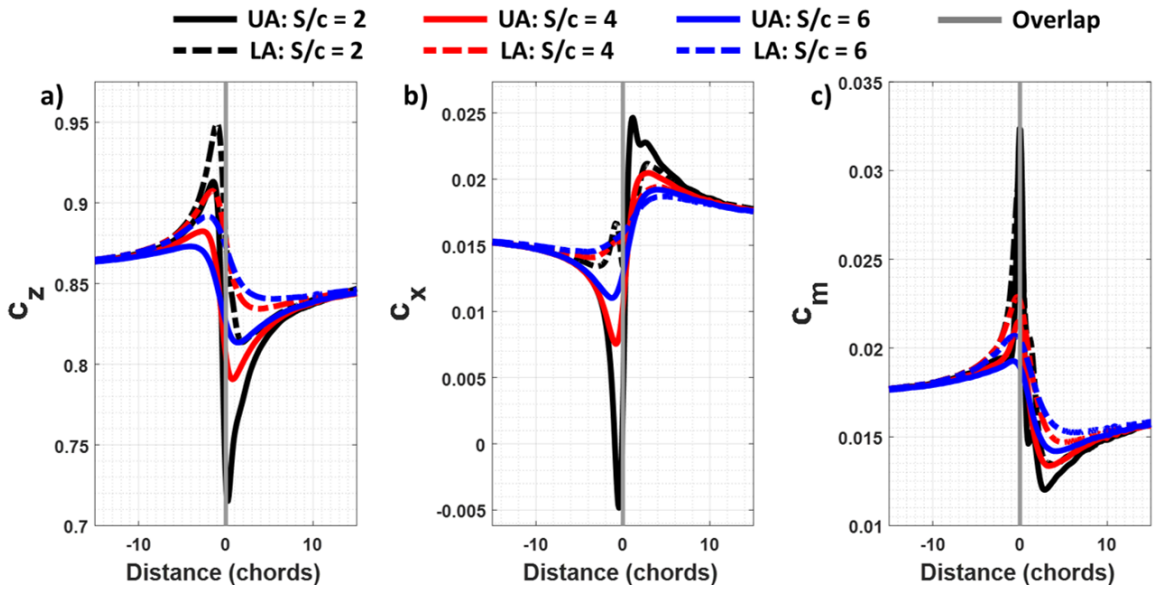

Figure 2.18: Two NACA 0012 airfoils crossing for a) c_z, b) c_x, and c) c_m versus distance to overlap (M = 0.5 (V_{tip} = 560 ft/s), α = 7°, and S/c = 2.0, 4.0, and 6.0 (c = 0.5 ft)).

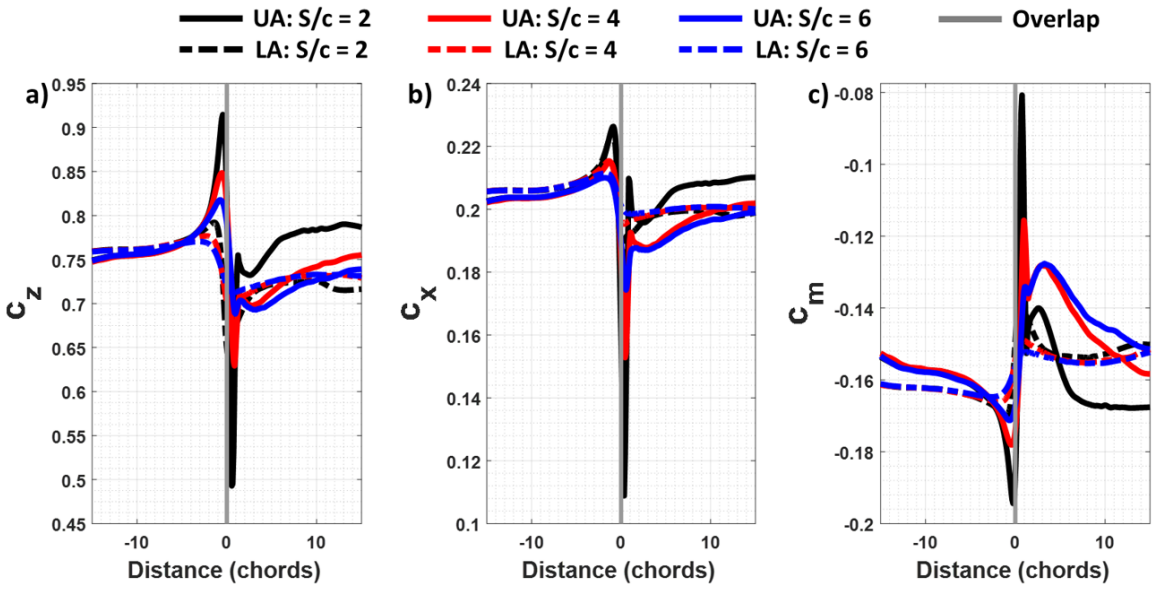

Figure 2.19: Two NACA 0012 airfoils crossing for a) c_z, b) c_x, and c) c_m versus distance to overlap (M = 0.9 (V_{tip} = 1,005 ft/s), α = 7°, and S/c = 2.0, 4.0, and 6.0 (c = 0.5 ft)).

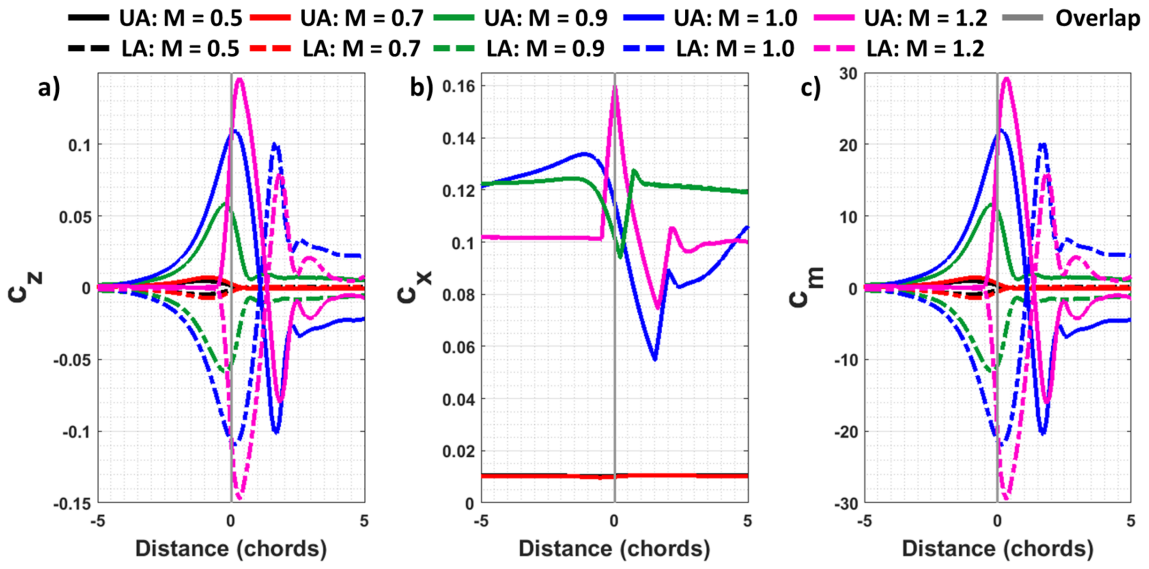

Figure 2.20: Two NACA 0012 airfoils crossing for a) c_z, b) c_x, and c) c_m versus distance to overlap (M = 0.5, 0.7, 0.9, 1.0, and 1.2 (V_{tip} = 560, 780, 1005, 1116, and 1340 ft/s), α = 0°, and S/c = 4.0 (S = 2.0 ft, c = 0.5 ft)).

with fixed angle-of-attack, and vertical separation distance.

Figure 2.20 shows c_z, c_x, and c_m for a Mach sweep of 0.50 to 1.2 for two NACA 0012 airfoils crossing. Even though helicopters avoid high-speed flight regimes, Mach numbers above 0.90 are compared to explore the design domain for educational purposes. Angle-of-attack of both airfoils was α = 0°, and S/c = 4.0 (S = 2.0 ft, c = 0.5 ft). An angle-of-attack of 0 is used to eliminate circulations effects, though an NACA 0012 still includes thickness effects. A large increase in lift, drag and moment is seen as Mach number reaches 0.90, where weak shocks begin to form.

Figure 2.21 shows the Mach contour of of two airfoils crossing a) before, b) at, and c) after overlap for Mach 1.2. As the two airfoils approach each other (Fig. 2.21 a)), a bow shock is formed in front of each airfoil. At the time of overlap (Fig. 2.21 b)), the shocks from each airfoil coincide and a shock-airfoil interaction occurs. After time of overlap (Fig. 2.21 c)), the the shock-airfoil interaction continues, where the lower surface of the upper airfoil is impacted by the upper surface shock of the lower airfoil and vice verse for

lower airfoil.

Today's helicopters avoid high Mach numbers, though a high Mach number of 0.9 is a more realistic case for today's coaxial rotors. Figure 2.22 shows the Mach contour of of two airfoils crossing a) before, b) at, and c) after overlap for Mach 0.9. As shown in Fig. 2.22, Fig. 2.22 also shows a shock-airfoil interaction but with weaker shocks. As angle-of-attack increases, so will the strength of the shocks and therefore resulting in unsteady aerodynamics.

2.3.5 Viscosity, shed vorticity, and downwash effects

The two airfoils traveling in opposite directions demonstrated the effects of circulation, thickness, and compressibility for a coaxial rotor, but lacked any treatment of the rotor wake, due to multiple blades. Viscous effects due to shed vorticity and downwash are discussed by comparing the aerodynamic flow field of an isolated airfoil, two airfoils crossing, single train of eight airfoils, and two trains of eight airfoils crossing. Inviscid calculations are performed to reveal further information that may not be easily discerned from viscous calculations.

As previously shown in Figs. 2.3 and 2.4, two airfoils crossing investigated circulation effects. VITS is further used to investigate shed vorticity by simulating a train of eight airfoils traveling in opposite directions, results are compared to OVERFLOW simulations as shown in Fig. 2.23. Comparing VITS simulations for UA/$LA$and $UA4$/$LA4$, the addition of airfoils resulted in a change in lift for $UA4$ and $LA4$ due to the circulation and crossing interaction of the surrounding airfoils, this was accounted for by using the Biot-Savart law [59]. Inviscid OVERFLOW calculations resulted in higher lift compared to the inviscid VITS potential calculations, this is due to the difference in airfoil modeling. OVERFLOW models the geometry, while VITS uses a source, vortex, and sink to represent an airfoil. The flight condition and geometry used to explore viscosity, shed vorticity, and downwash effects are based on a modern rotor design at a span location of r/R = 0.40, where M =

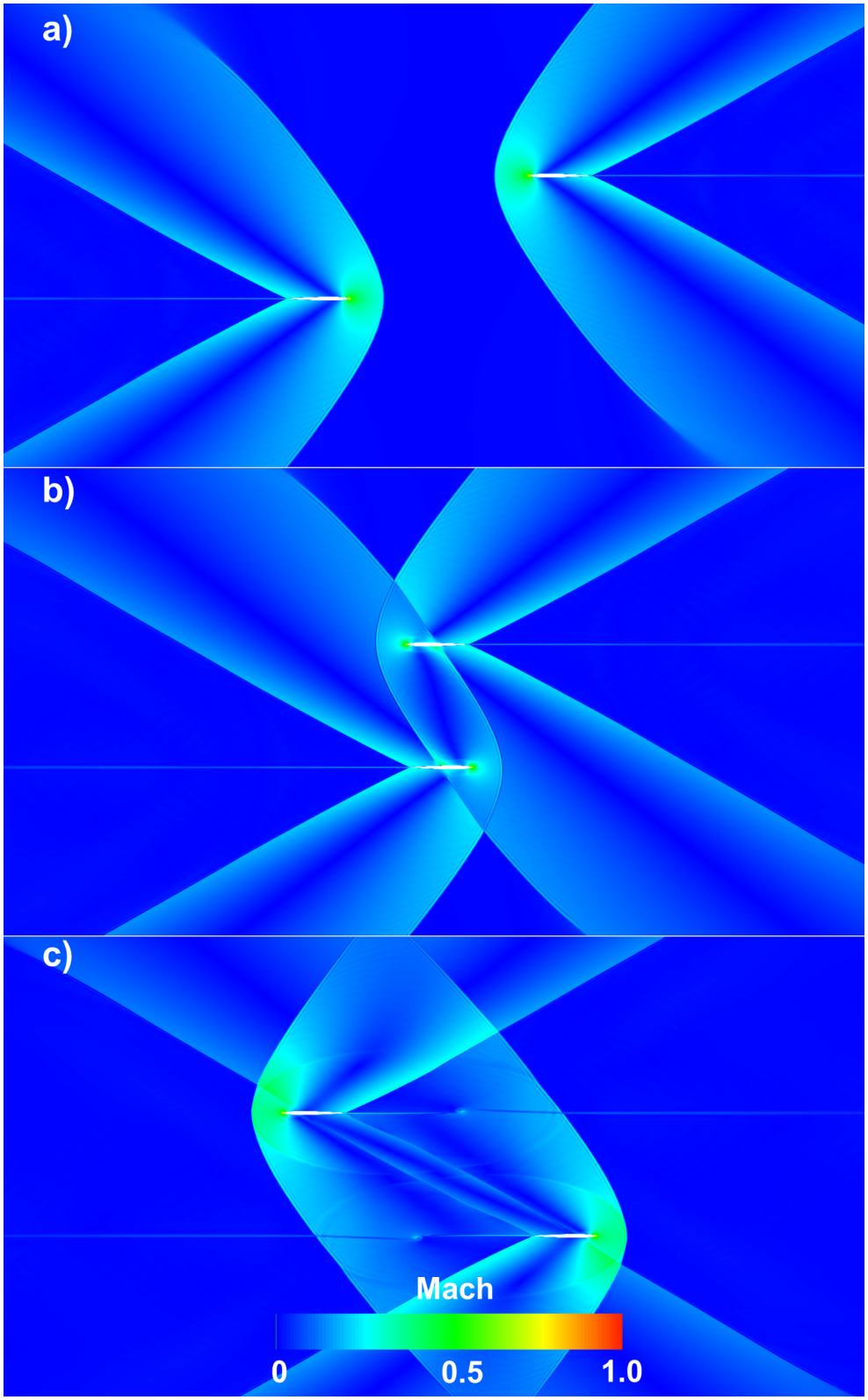

Figure 2.21: Mach contour of two airfoils crossing a) before, b) at, and c) after overlap (M = 1.2, α = 0°, and S/c = 4.0 (S = 2.0 ft, c = 0.5 ft)).

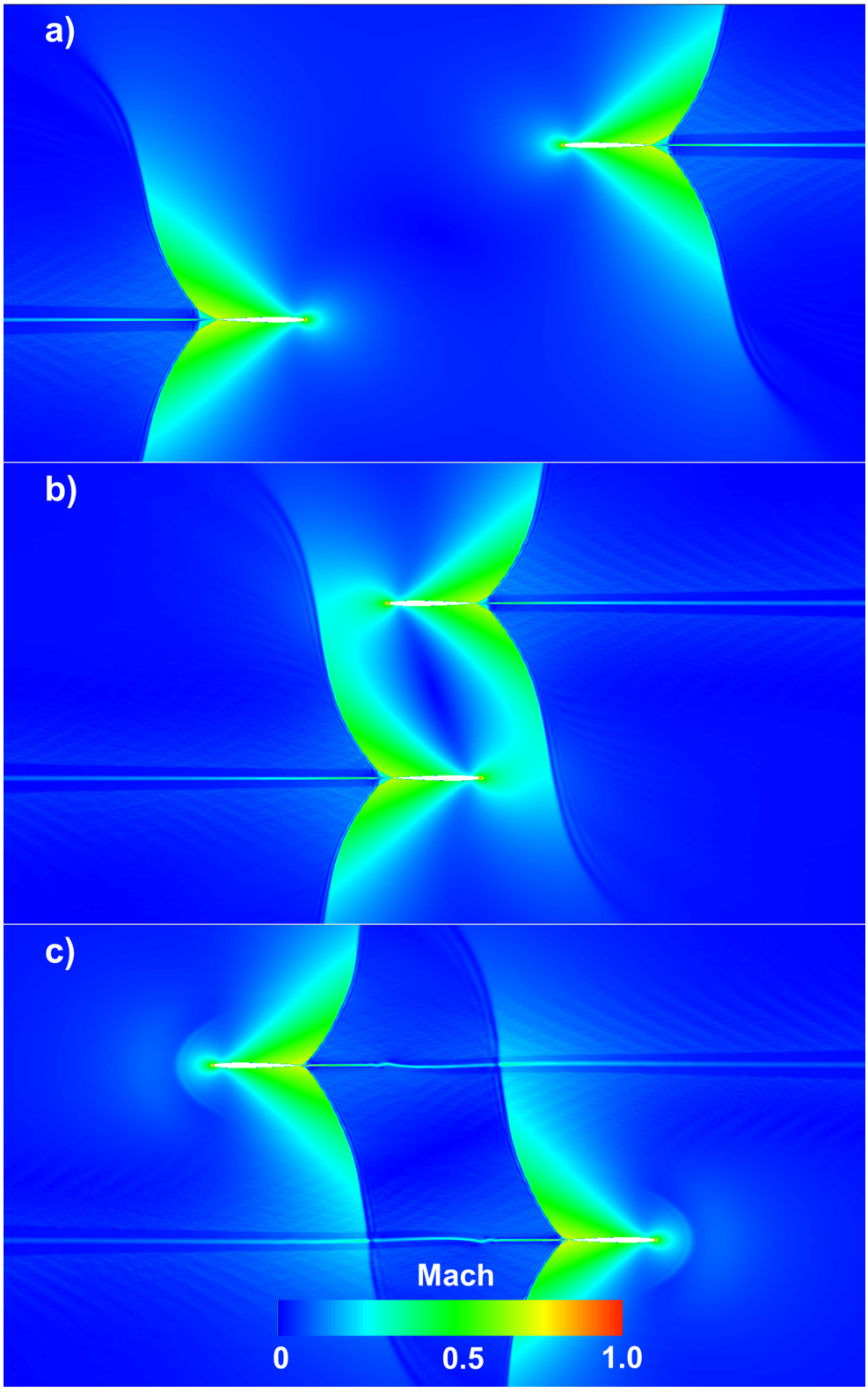

Figure 2.22: Mach contour of two airfoils crossing a) before, b) at, and c) after overlap (M = 0.90, α = 0°, and S/c = 4.0 (S = 2.0 ft, c = 0.5 ft)).

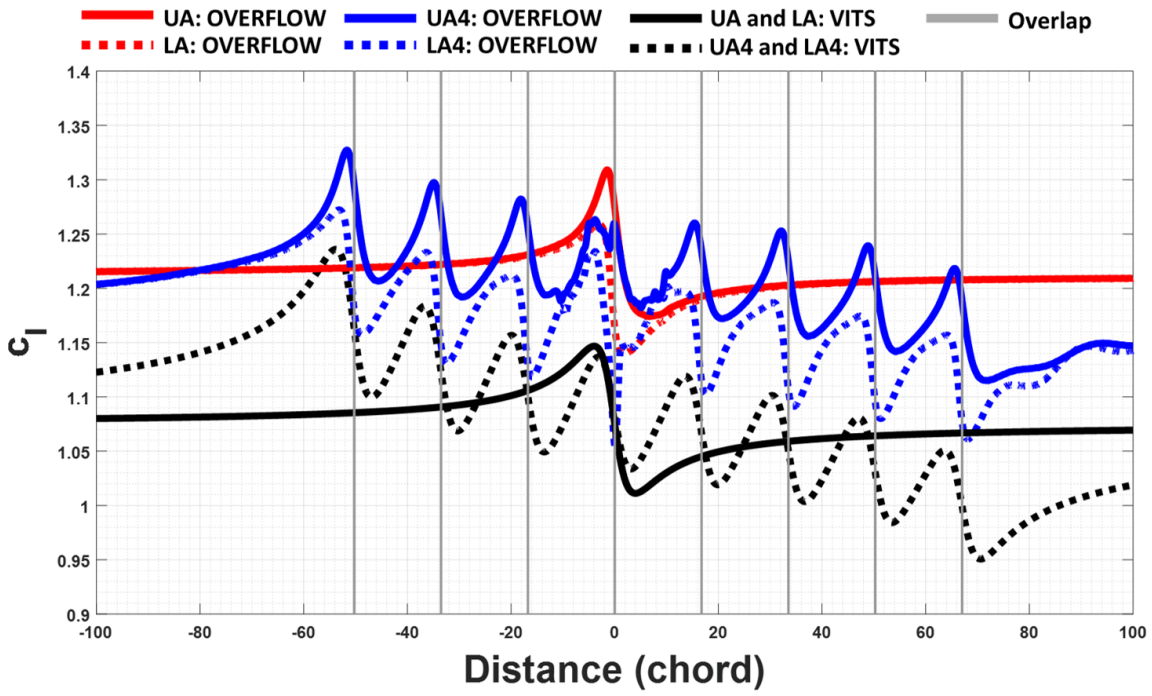

Figure 2.23: VITS (inviscid) and OVERFLOW (inviscid) calculations of two airfoils and two trains of eight airfoils crossing, c_l versus distance to overlap in chords (M = 0.25, α = 9.8°, and S/c = 4.0 (S = 2.0 ft, c = 0.5 ft), and D/c = 33.51).

0.25, α = 9.8°, and S/c = 4.0 (S = 2.0 ft, c = 0.5 ft), and D/c = 33.51, see Table 2.8.

Deposited shed vorticity was not represented in VITS calculations. To explore the effect of shed vorticity, OVERFLOW y-vorticity contours are shown. Inviscid flow field disturbances dissipate at a slow rate, because of this the shed vorticity can be preserved and further analyzed. Each effect and simulation is discussed and compared in terms of c_z, c_x, and c_m versus distance to airfoil overlap, coefficient of pressure contour (C_P), and y-vorticity contour.

The vertical separation distance of the two airfoils is equal to the horizontal distance between the two rotors of a coaxial rotor. To model the blade phase angle in 2D, the distance between two airfoils (e.g. $UA3$ and $UA4$) was set to the circumferential distance between adjacent blade the tips (or specified r/R location) of the modeled rotor (see Fig. 2.9). A total of eight airfoils was simulated and the 4th airfoil in the trains ($UA4$ and $LA4$) was chosen to ensure that the aerodynamics influence from the airfoils ahead and behind were

Figure 2.24: Multiple airfoil simulation illustration at time of overlap of $UA4$ and $LA4$.

captured. Further investigation regarding the total number of airfoils is necessary to ensure a converged solution for the middle airfoil in the train, which was not performed in this dissertation.

Two trains of eight airfoils traveling in opposite directions were simulated in order to investigated the effect of blade crossing, shed vorticity and downwash as depicted in Figs. 2.7 m), n), o), and p). Figure 2.24 shows a train of eight airfoils representing the upper rotor blades and eight airfoils representing the lower rotor blades. Airfoils are labeled by vertical position (upper or lower) and horizontal position. For example, upper airfoil four and lower airfoil four are denoted as $UA4$ and $LA4$. Figure 2.24 shows the positions of a multiple airfoil simulation when $UA4$ and $LA4$ are overlapped (the quarter-chord location of each airfoil coincide). All results shown are when $UA4$ and $LA4$ are overlapped. The full time history for the multiple viscid airfoil simulation $UA4$ and $LA4$ over time with labeled crossings (M = 0.25, α = 9.8°,V_i = 31 ft/s, S/c = 4.0 (S = 2.0 ft, c = 0.5 ft), and D/c = 33.51) are shown in Fig. 2.25. By the time $UA4$ and $LA4$ overlap, $UA4$ has already overlapped with $LA1$ through $LA3$, while $LA4$ has overlapped with $UA1$ through $UA3$.

Figure 2.26 shows viscid and inviscid isolated airfoil, two airfoils crossing at crossing (UA/LA), single train of eight airfoils ($A4$), and two trains of eight airfoils at crossing ($UA4$/$LA4$) with and without downwash for c_z versus distance (M = 0.25, α = 9.8°,V_i = 31 ft/s, S/c = 4.0 (S = 2.0 ft, c = 0.5 ft), and D/c = 33.51). Figures. 2.27 and 2.28 show c_x and c_m versus distance for the same condition for viscid simulations only. For the same conditions, the flow field in terms of C_P contour are shown in Fig. 2.29 for the isolated

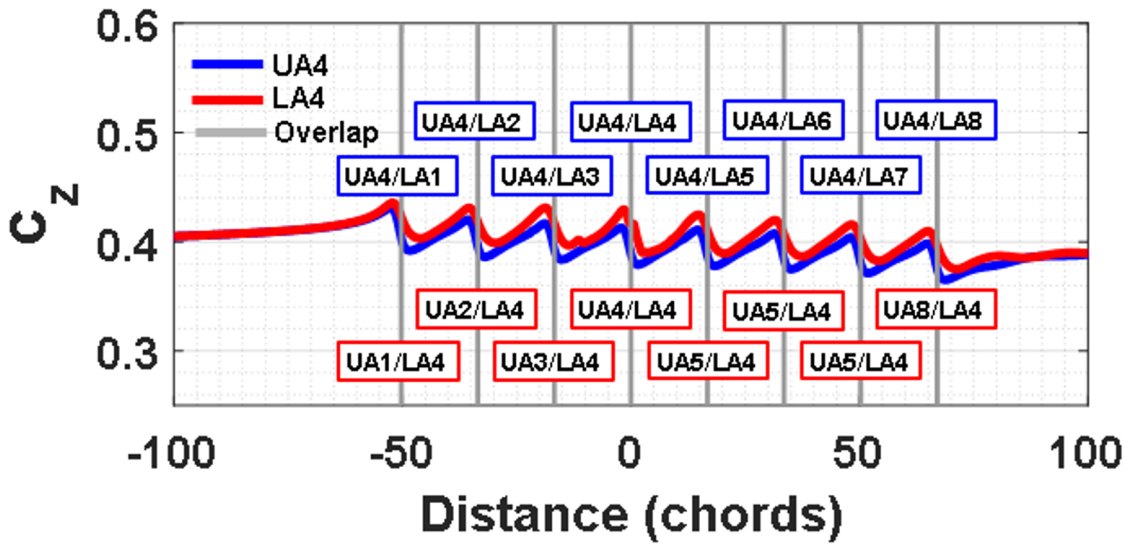

Figure 2.25: Two trains of eight airfoils crossing viscid airfoil simulation $UA4$ and $LA4$ for c_x verses distance to overlap of $UA4$ and $LA4$ with downwash (M = 0.25, α = 9.8°,V_i = 31 ft/s, S/c = 4.0 (S = 2.0 ft, c = 0.5 ft), and D/c = 33.51).

airfoil, single train of eight airfoils, and at the time of crossing of two airfoils and a train of eight airfoils crossing simulation. The C_P contour reveals a clear difference between the isolated airfoil and single train of airfoils simulations (Figs. 2.29 a) through d) and Figs. 2.29 i) through l)) compared to the simulations with crossing events (Figs. 2.29 e) through h) and Figs. 2.29 m) through p)), were the flow fields of the on coming airfoil(s) coincide. Further investigation of the flow field is performed to understand the effects of downwash and shed vorticity.

The effect of viscosity for all the different simulations (isolated airfoil, single train of eight airfoils, and at the time of crossing of two airfoils and a train of eight airfoils crossing) whether downwash is present or not, showed an increase in c_z versus distance (Fig. 2.26) for the inviscid simulations compared to the viscid simulations. Lift is higher for the inviscid calculations due to the absence of a boundary layer. Inviscid solutions for c_x and c_m are negligible due to the absence of viscosity and are not shown in Figs. 2.27 and 2.28 .

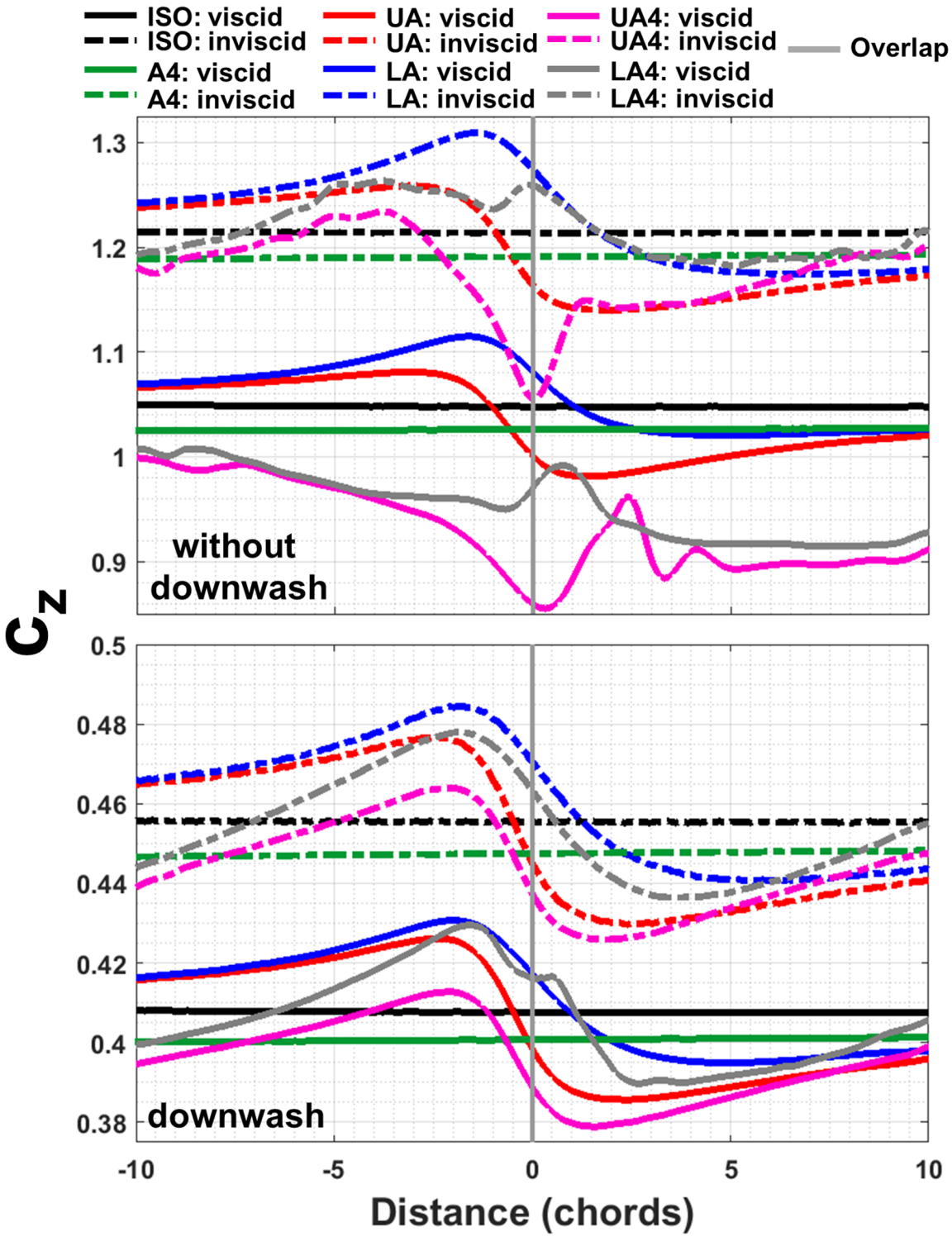

Figure 2.26: Viscid and inviscid isolated airfoil, two airfoils crossing at crossing (UA/LA), single train of eight airfoils ($A4$), and two trains of eight airfoils at crossing ($UA4/LA4$) with and without downwash c_z versus distance (M = 0.25, α = 9.8°, V_i = 31 ft/s, S/c = 4.0 (S = 2.0 ft, c = 0.5 ft), and D/c = 33.51).

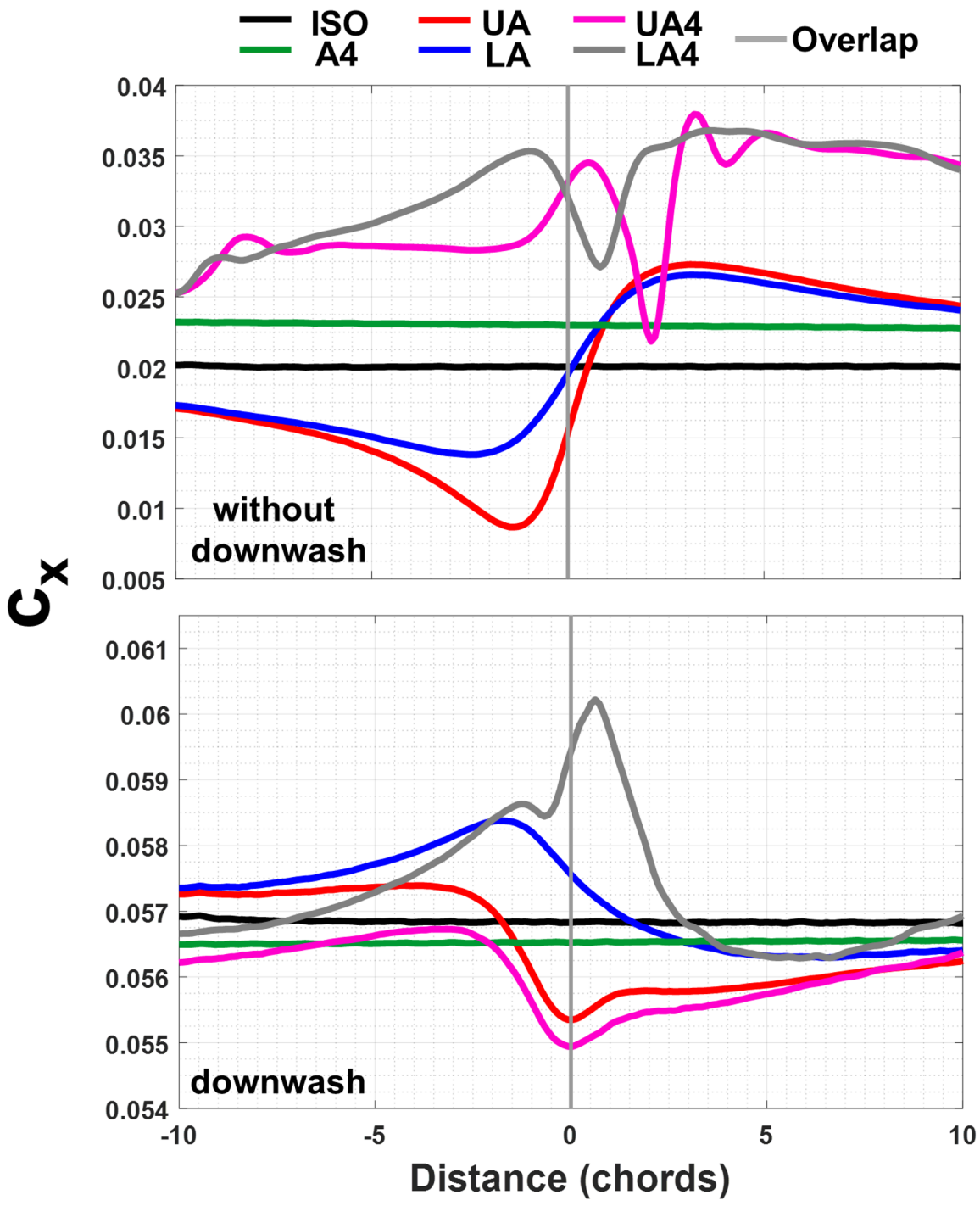

Figure 2.27: Viscid isolate airfoil, two airfoils crossing at crossing (UA/LA), single train of eight airfoils ($A4$), and two trains of eight airfoils at crossing ($UA4/LA4$) with and without downwash c_x versus distance (M = 0.25, α = 9.8°, V_i = 31 ft/s, S/c = 4.0 (S = 2.0 ft, c = 0.5 ft), and D/c = 33.51).

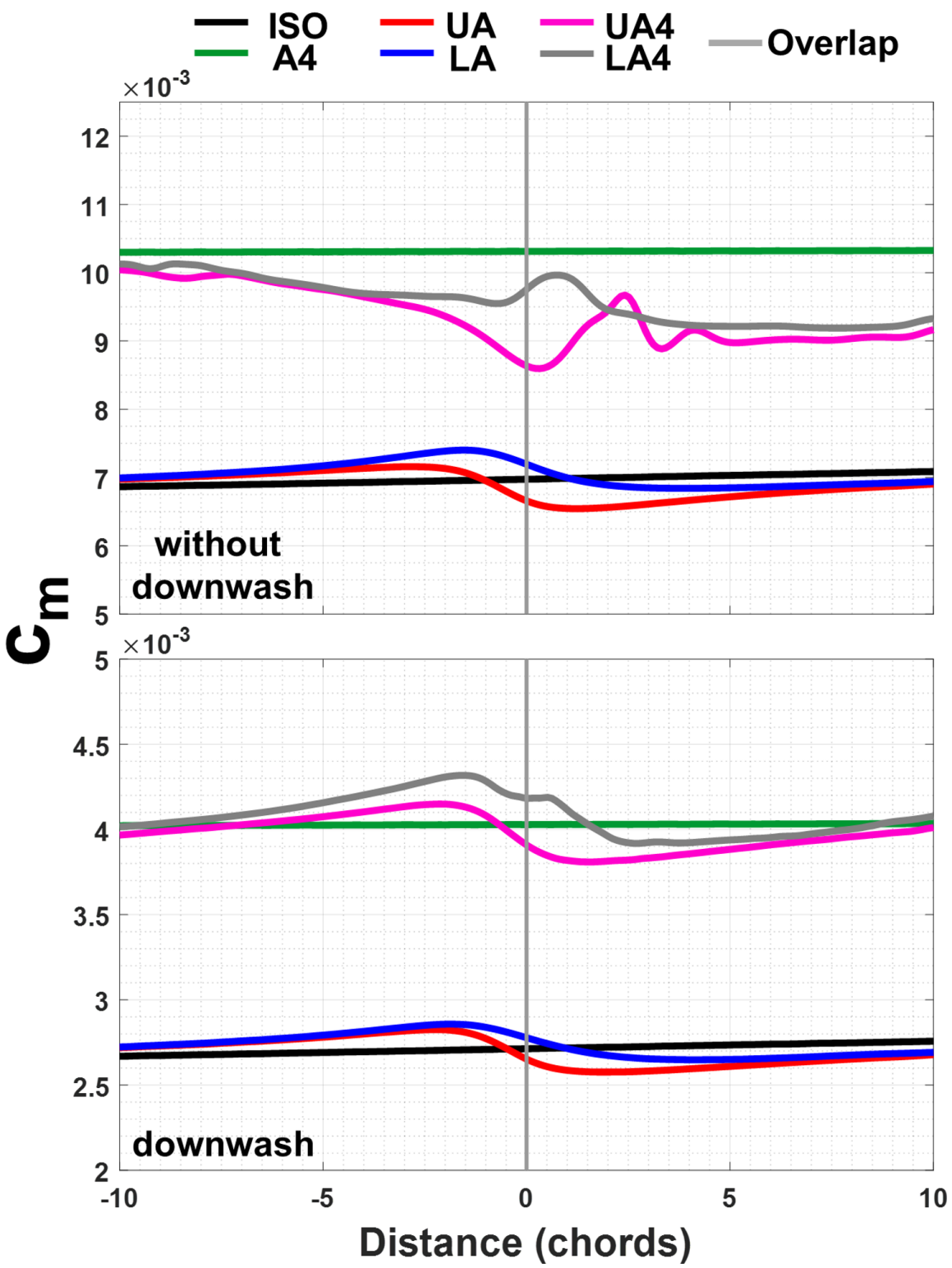

Figure 2.28: Viscid isolate airfoil, two airfoils crossing at crossing (UA/LA), single train of eight airfoils ($A4$), and two trains of eight airfoils at crossing ($UA4/LA4$) with and without downwash c_x versus distance (M = 0.25, α = 9.8°, V_i = 31 ft/s, S/c = 4.0 (S = 2.0 ft, c = 0.5 ft), and D/c = 33.51).

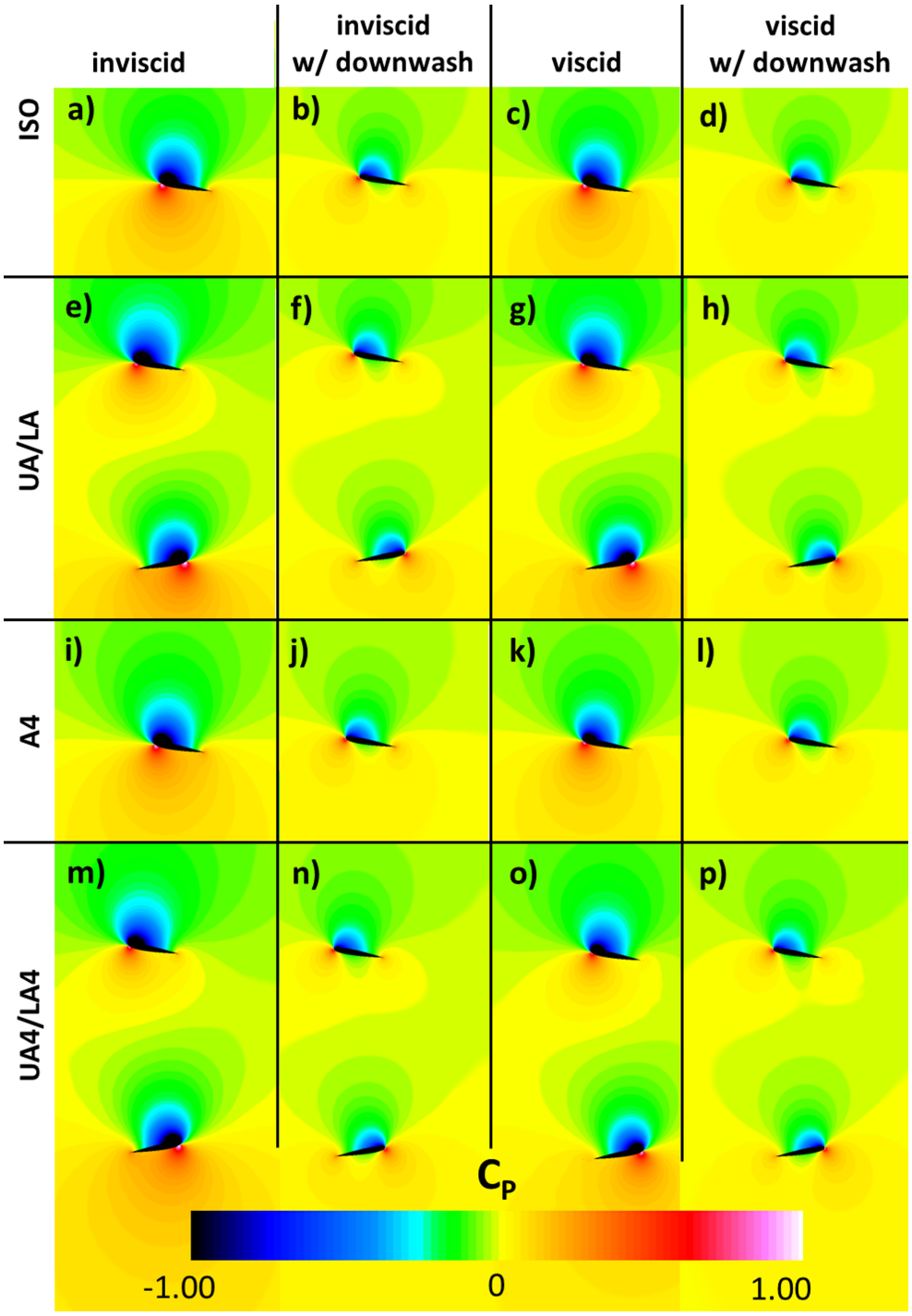

Figure 2.29: Isolated airfoil, two airfoils crossing at crossing (UA/LA), single train of eight airfoils ($A4$), and two trains of eight airfoils at crossing ($UA4/LA4$) for an inviscid no downwash (a), e), i), and m)), inviscid with downwash (b), f), j), and n)), viscid no downwash (c), g), k), and o)), and viscid with downwash (d) h) i) and p)), simulation C_P contour (M = 0.25 (V_{tip} = 280 ft/s), α = 9.8°, V_i = 31 ft/s, and S/c = 4.0 (S = 2.0 ft, c = 0.5 ft)).

Isolated airfoil

As shown in Figs. 2.26 through 2.28 for an isolated airfoil, a larger lift is observed for inviscid calculations compared to viscous calculations. For an isolated airfoil, C_P and y-vorticity contour is shown in Figs 2.30 and 2.31 for a) viscid no downwash, b) viscid with downwash, c) inviscid, no downwash, and d) inviscid, downwash simulation (M = 0.25 (V_{tip} = 280 ft/s), α = 9.8°, V_i = 31 ft/s).

The pressure above the viscid and inviscid isolated airfoils without downwash (Figs. 2.30 a) and c)) is lower compared to the simulations with downwash (Figs. 2.30 b) and d)), while below the inviscid airfoils without downwash the pressure is larger compared to the simulations with downwash, because of this lift for viscid and inviscid airfoils without downwash is greater. The simulated downwash decreased overall lift for the inviscid and viscid solution and increased drag for the viscid simulation. Comparing the flow field of the viscid and inviscid airfoils without downwash (Figs. 2.30 a) and c)) little information between the two simulations can be discussed, because of this the y-vorticity contour of the flow field is analyzed.

The y-vorticity contour further reveals the differences between the inviscid and viscid without (Figs. 2.31 a) and c)) and with downwash (Figs. 2.31 b) and d)) simulations. The inviscid and viscid simulation with downwash show a downward y-vorticity at the trailing edge of the airfoil pattern to the simulation without downwash, this is due to the vertical velocity (V_i) of 31 ft/s. Viscid solutions have higher y-vorticity due to the presence of a boundary layer (viscosity). Furthermore, the addition of downwash decreases lift, the vertical velocity decreases the angle-of-attack causing an decrease in lift, while drag and moment is increased.

Two airfoils crossing

A second airfoil traveling in the opposite direction was added to the isolated airfoil simulation. Compared the isolated airfoil results all simulations of two airfoils crossing show a

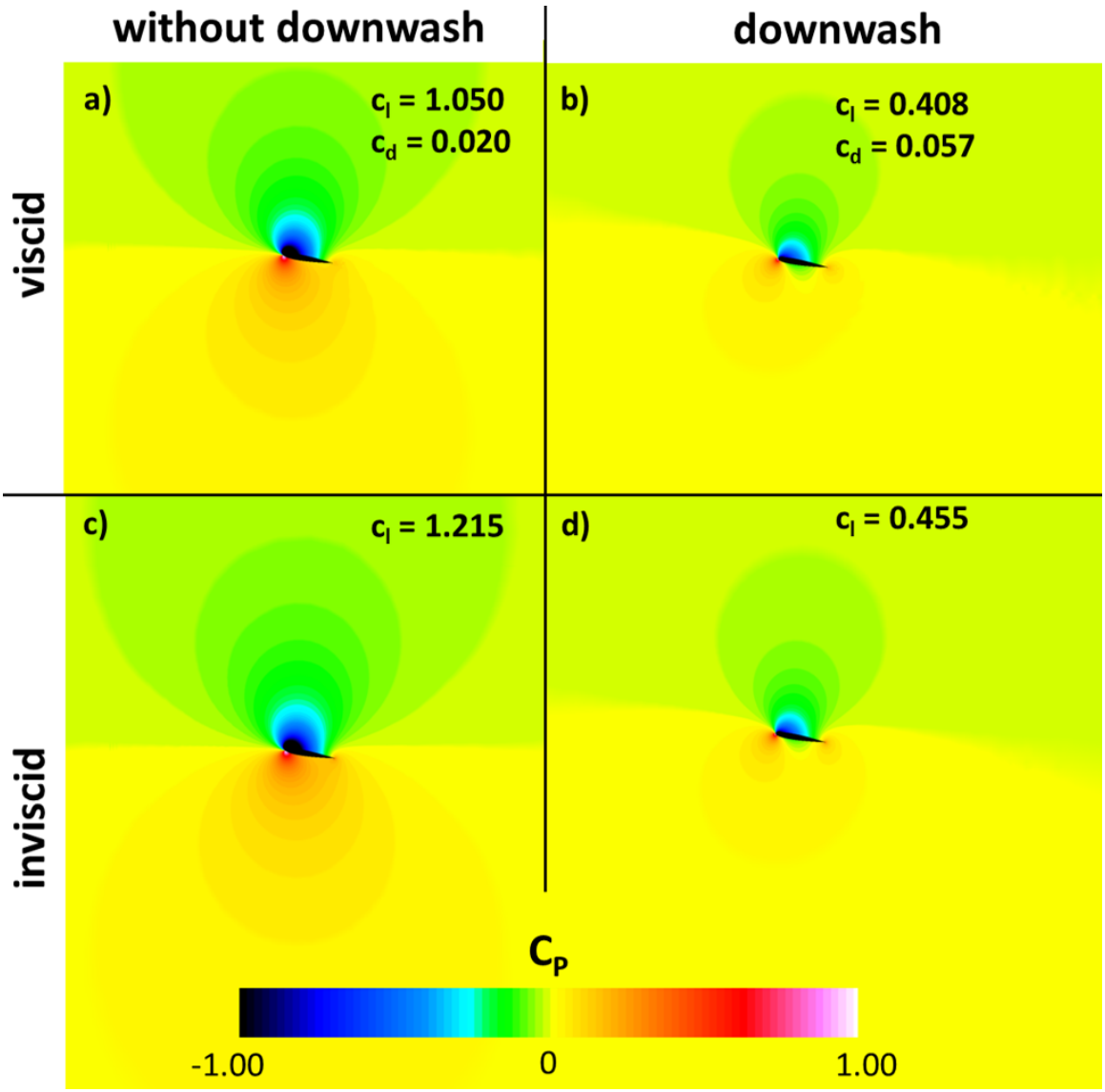

Figure 2.30: An isolated NACA 0012 airfoil C_P contour for a) viscid no downwash, b) viscid with downwash, c) inviscid, no downwash, and d) inviscid, downwash simulation (M = 0.25 (V_{tip} = 280 ft/s), α = 9.8°, V_i = 31 ft/s). Note: abrupt changes in contour levels is due to changing grid densities and numerical issues.

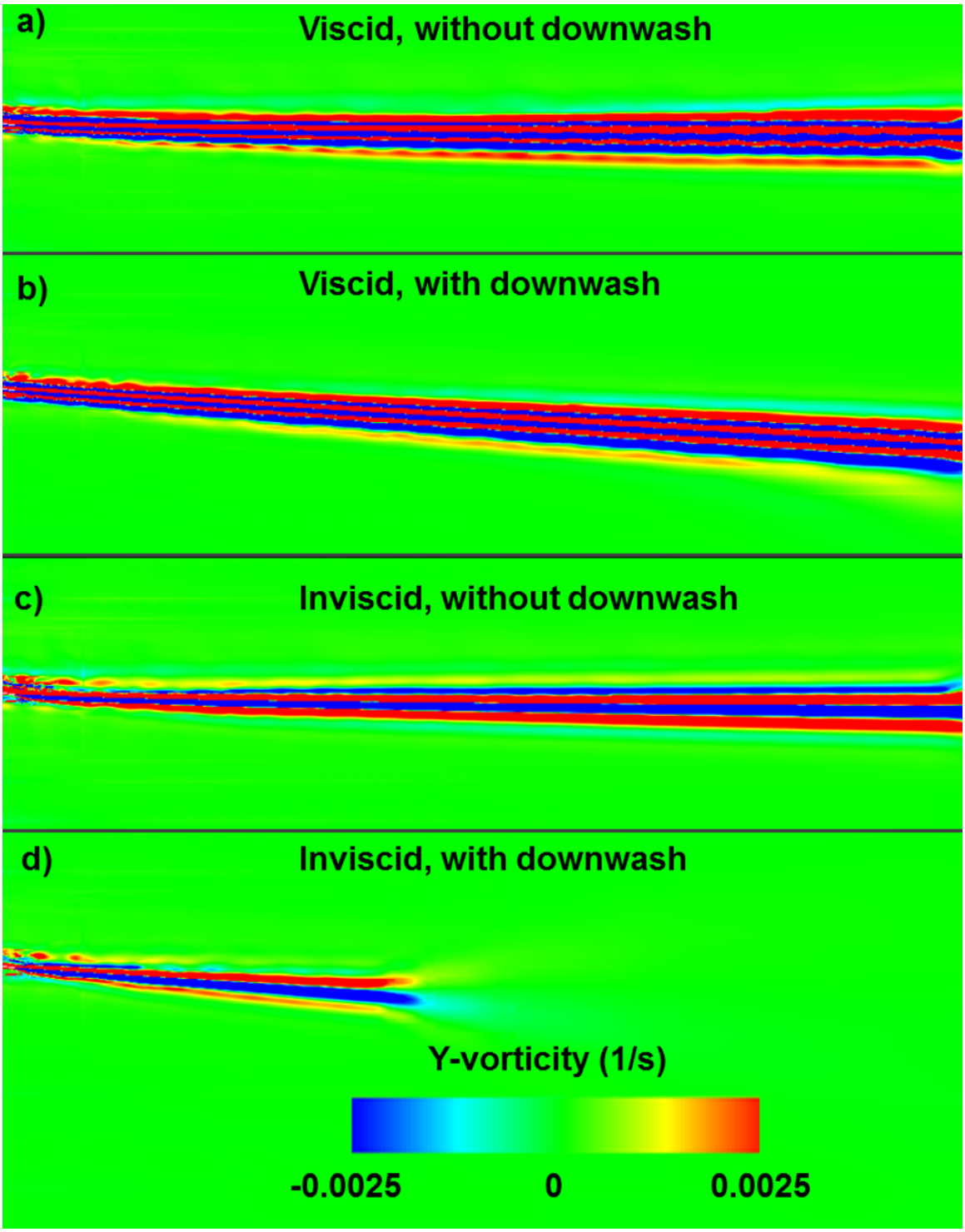

Figure 2.31: An isolated NACA 0012 airfoil wake y-vorticity contour for a) viscid no downwash, b) viscid with downwash, c) inviscid, no downwash, and d) inviscid, downwash simulation (M = 0.25 (V_{tip} = 280 ft/s), α = 9.8°, V_i = 31 ft/s).

change in c_z, c_x, and c_m before and after time of overlap (Figs. 2.26 through 2.28). The change in c_z, c_x, and c_m is caused by the interaction of the flow fields of each airfoil. Viscid flow field C_P contours for two NACA airfoils crossing before, at, and after with downwash are shown in Fig. 2.32 (M = 0.25 (V_{tip} = 280 ft/s), α = 9.8°, V_i = 31 ft/s, and S/c = 4.0 (S = 2.0 ft, c = 0.5 ft)). As previously shown in Fig. 2.4 and shown in Fig. 2.32, as the two airfoils approach each other the flow field between the two airfoils start to interact, which results in a change in angle-of-attack of both airfoils due to the induced velocity (see Fig. 2.5).

Figure 2.33 shows vorticity contours of the flow field of two NACA 0012 airfoils after time of crossing. Viscid and inviscid results are shown, with and without a vertical velocity imposed (M = 0.25 (V_{tip} = 280 ft/s), α = 9.8°, V_i = 31 ft/s). Similar to the isolated airfoil (Fig. 2.31), the vorticity behind the airfoil travels downward due to the imposed vertical velocity (Figs. 2.33 b), d)).

The effect of shed vorticity is highlighted after the airfoils cross each other at the location of overlap, as shown in Fig. 2.33. Inviscid calculations with and without downwash reveal deposited vorticity at the location of overlap (Figs. 2.33 c) and d)), while viscid solutions are harder see due to the presence of viscosity (Figs. 2.33 a) and b)). The addition of downwash reduces the angle-of-attack for each airfoil, resulting in less shed vorticity in the overlap region.

Single train of eight airfoils

The change in airfoil circulation with time ($-d\Gamma/dt$) was calculated from the airfoil lift time history in order to investigate shed vorticity. The circulation calculations were first performed for an isolated airfoil and the upper airfoil (UA) of a two airfoil simulations, as shown in Fig. reffig:gamma (HC1: M = 0.47 (V_{tip} = 500 ft/s), α = 7°, and S/c = 6.21 (S = 2.33 ft, c = 0.375 ft)). The horizontal axis is in terms of chord distance to overlap; negative and positive values correspond to before and after airfoil overlap, respectively. The vertical

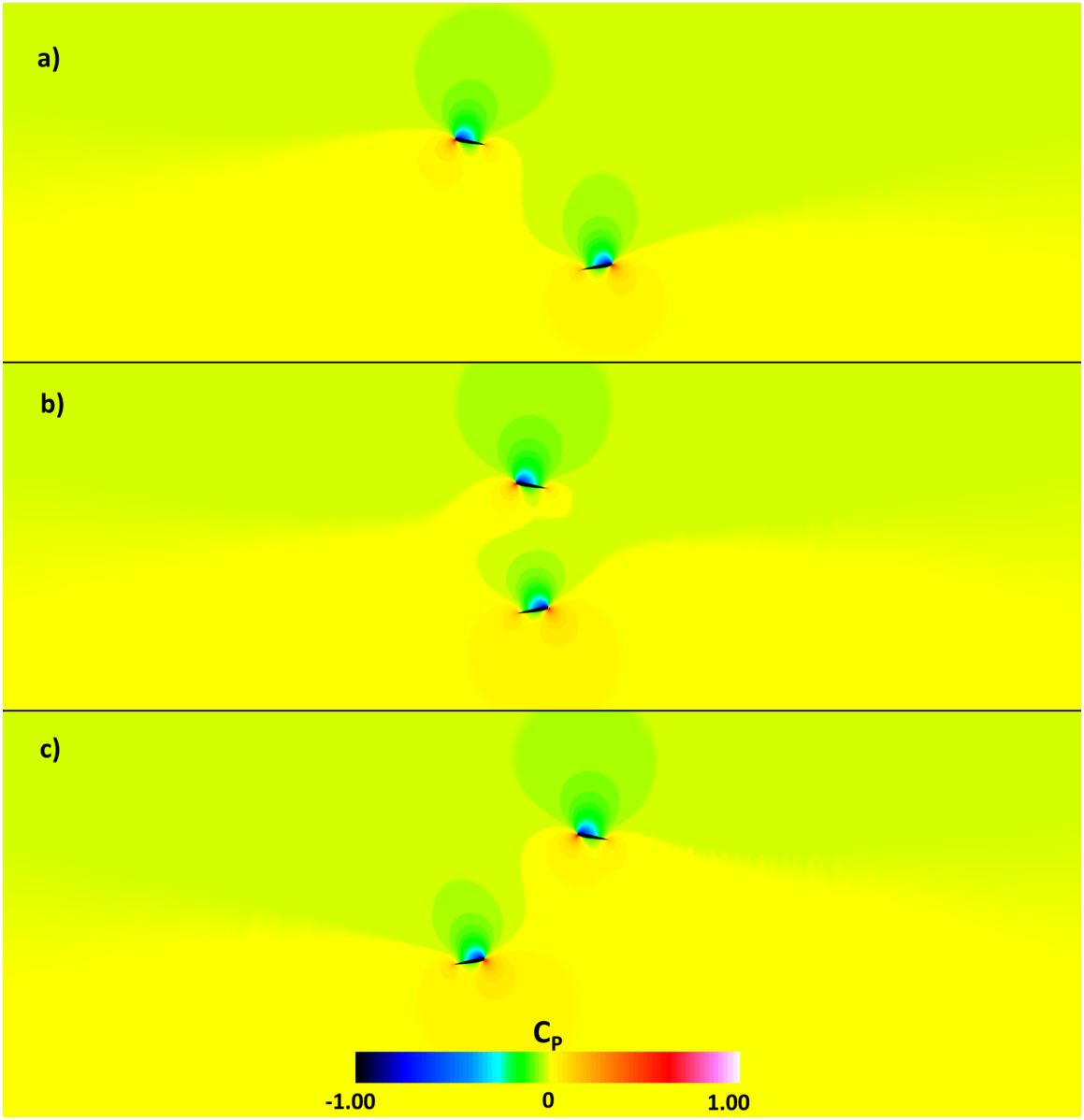

Figure 2.32: Viscid flow field C_P contour of two NACA 0012 airfoils crossing a) before, b) at, and c) after with downwash (M = 0.25 (V_{tip} = 280 ft/s), α = 9.8°, V_i = 31 ft/s, and S/c = 4.0 (S = 2.0 ft, c = 0.5 ft)).

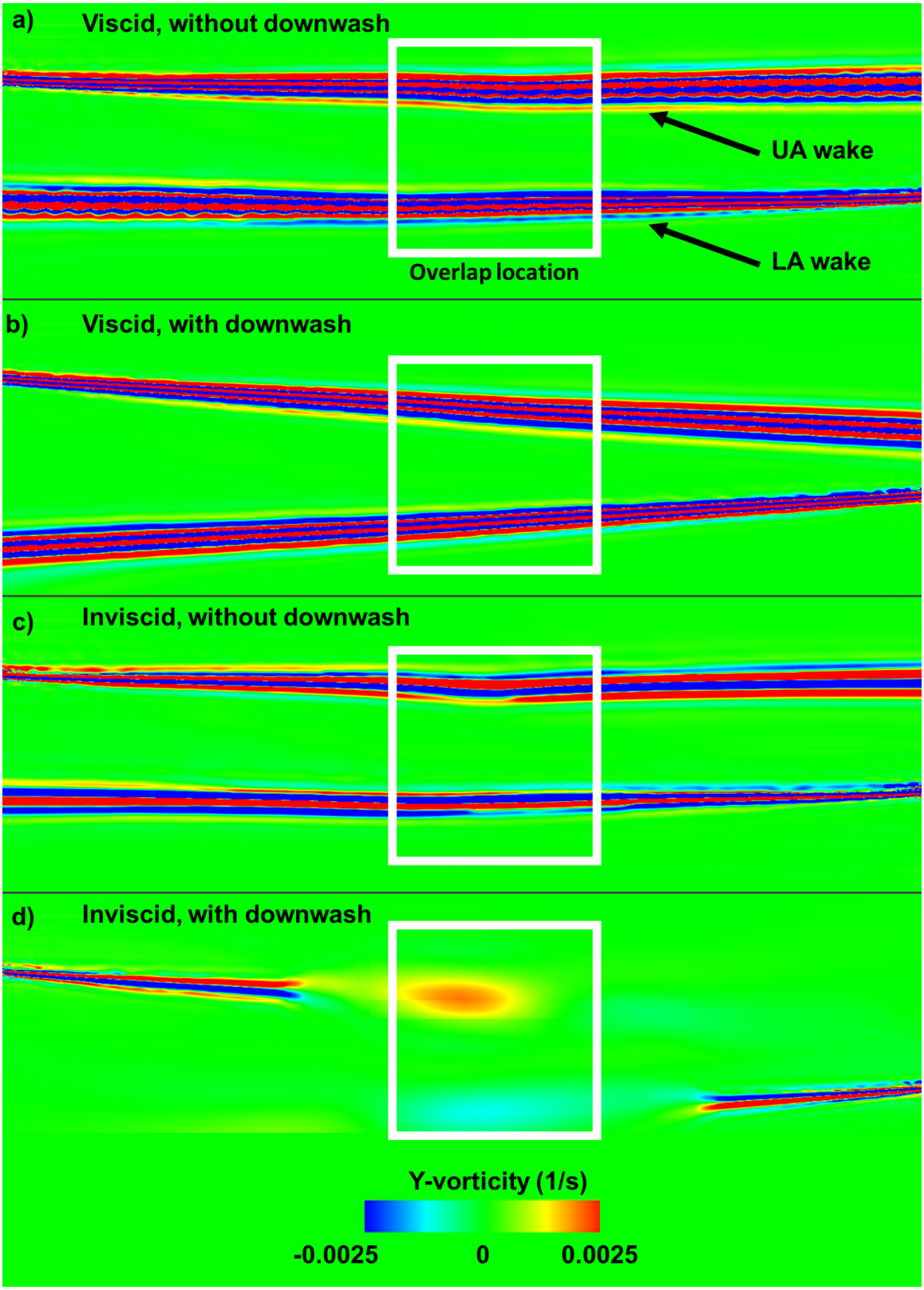

Figure 2.33: Two NACA 0012 airfoils y-vorticity contour after time of crossing for a) viscid no downwash, b) viscid with downwash, c) inviscid, no downwash, and d) inviscid, downwash simulation (M = 0.25 (V_{tip} = 280 ft/s), α = 9.8°, V_i = 31 ft/s, and S/c = 4.0 (S = 2.0 ft, c = 0.50)).

gray line the location where the quarter-chord of the upper and lower airfoils overlap. The c_z results are converted to circulation (Γ) (Fig. 2.34 b)), then the negative time derivative of circulation is computed to obtain shed vorticity ($-d\Gamma/dt$) (Fig. 2.34 c)). The circulation is negated to satisfy Kelvins circulation theorem (conservation of body forces), and the derivative of circulation is taken with respect to time (distance) due to the time varying loads. There is an increase in shed vorticity beginning about ten chords before overlap, peaking just before overlap, and then decreasing back to zero approximately ten chords after overlap. In order to simulate the effect of shed vorticity, a train of airfoils is modeled to investigate the impact of deposited shed vorticity on an airfoil in the middle of the train (analogous to a rotor with multiple blades).

When airfoils are added ahead or behind an isolated airfoil, each airfoil will encounter the wakes of the preceding airfoils. Rapid changes in airfoil lift and drag, due to wake interactions, will result in shed vorticity deposited into the fluid medium. Any ensuing airfoils that impinge on these shed vortices are susceptible to additional airload fluctuations.

A single train of eight airfoils were simulated in order to investigate the effect of shed vorticity as depicted in Figs. 2.7 i), k), j), and l). A train of eight airfoils was chosen to ensure that there was sufficient aerodynamic influence from airfoils preceding and following the airfoil of interest. The 4th airfoil in the train was selected for analysis and is noted as $A4$.

Comparing $A4$ to the isolated airfoil, the difference in c_z shows an overall small decrease in lift for all inviscid and viscid calculations with and without downwash (Fig. 2.26), while a small increase in viscid c_x calculations is observed (Fig. 2.27). An overall increase in viscid c_m calculations is observed for $A4$ compared to the isolated airfoil simulations with and without downwash (Fig. 2.28).

Vorticity contours for $A4$ are shown in Fig. 2.35. The wakes from the airfoils preceding $A4$ are clearly shown in Figs. 2.35 a), b), and c), where as in Fig. 2.35 d) the wakes are not seen. The presence of downwash pushes the wake from the preceding two ($A2$, $A3$)

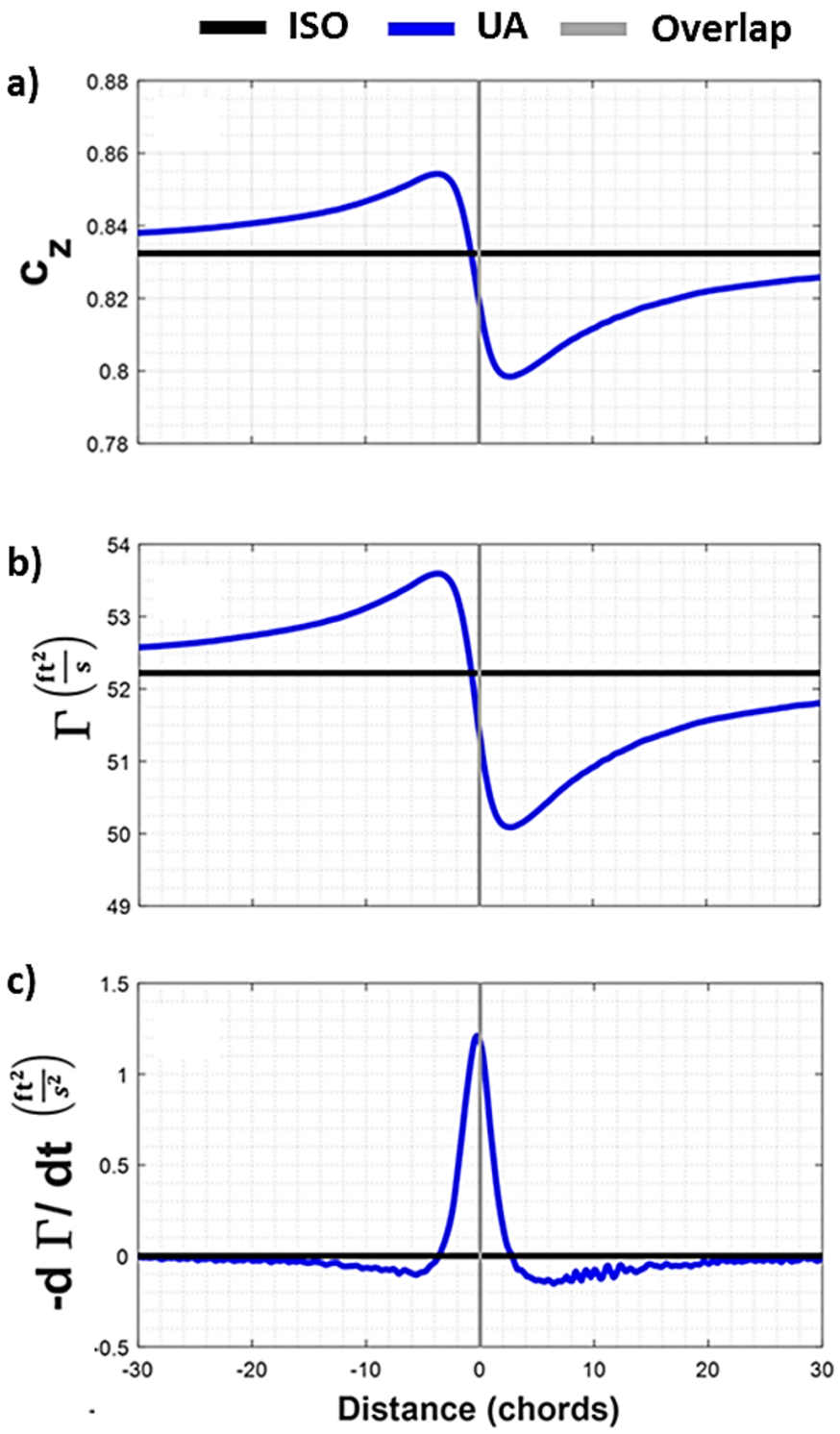

Figure 2.34: Results for an isolated airfoil and the upper airfoil of the two airfoils crossing case a) c_z, b) Γ, and c) -$d\Gamma/dt$. Horizontal axis is distance to overlap for the upper airfoil (UA) (HC1: M = 0.47 (V_{tip} = 500 ft/s), α = 7°, and S/c = 6.21 (S = 2.33 ft, c = 0.375 ft)).

airfoils ahead of $A4$ into proximity of $A4$ (Fig. 2.35 b)), the wake is not seen in the inviscid simulation (Fig. 2.35 d)) due to the absence of viscosity.

Two trains of eight airfoils crossing

The final configuration studied was two eight-airfoil trains. The addition of the second train should capture all effects explored thus far: circulation, thickness, compressibility, viscosity, downwash. The 4th airfoils of the upper train and lower trains, $UA4$ and $LA4$, respectively, were analyzed. The two airfoils, $UA4$ and $LA4$, experienced lower lift, higher drag and higher moment compared to the case of two airfoils (UA, LA) crossing, with and without downwash (Figs. 2.26 through 2.28). As $UA4$ and $LA4$ encounter an overlap, the deposited shed vorticity builds upon previous deposited shed vorticity from overlapping occurrences, resulting in lower lift, higher drag and higher moment.

A comparison of vorticity fields of UA/LA and $UA4$/$LA4$ with downwash is shown in shown in Figs. 2.37 a) and b), respectively. The addition of airfoils further complicates the flow. Although the downwash pushes the wake and deposited shed vorticity downward, in Fig. 2.37 b) the oncoming lower airfoil ($LA4$) encounters the wake of $UA3$. Figure 2.36 shows c_z versus distance to overlap of $UA4$ and $LA4$, where $UA4$ and $LA4$ are overlapping $LA1$-$LA8$ and $UA1$-$UA8$, respectively. Also shown in Fig. 2.36 are viscid calculations with downwash for an isolated airfoil (ISO), two airfoils crossing (UA,LA), and a single train of eight airfoils crossing ($A4$). Comparing $UA4$ and $LA4$ to the other simulations, the mean lift decreases after each overlapping occurrence. The decrease in lift is due to the deposited shed vorticity.

2.3.6 Modern coaxial and single rotor design comparison: hover

Comparisons were made between a modern single rotor and a coaxial rotor was performed to highlight aerodynamic differences (see Table 2.2 for 2D analog). A single train of eight airfoils was used to simulate a single rotor in hover, as shown in Fig. 2.7 o). Two trains of

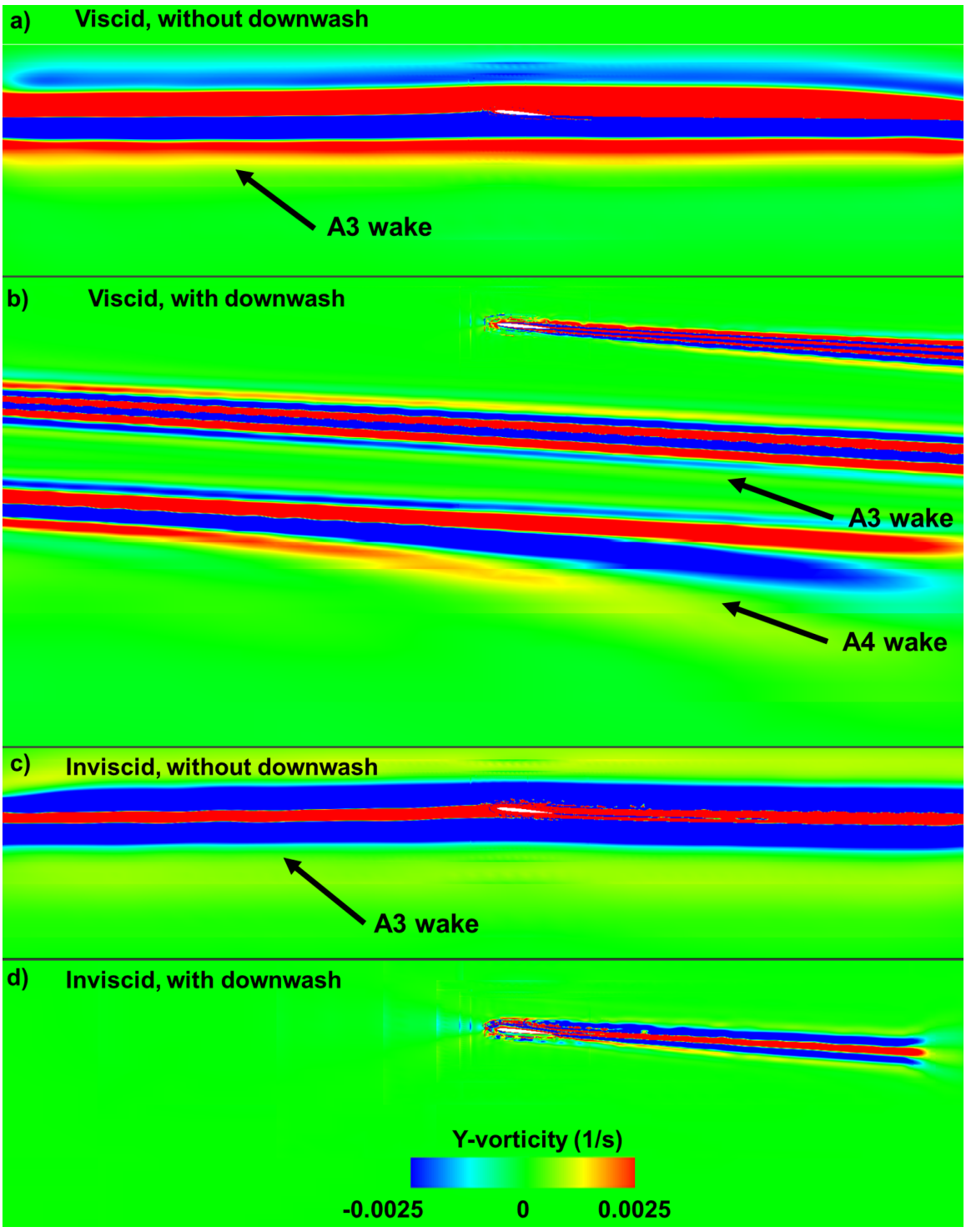

Figure 2.35: Vorticity contours for $A4$ (4th airfoil in a train of eight airfoils) for a) viscid no downwash, b) viscid with downwash, c) inviscid, no downwash, and d) inviscid, downwash simulation (M = 0.25, α = 9.8°,V_i = 31 ft/s, and D/c = 33.51).

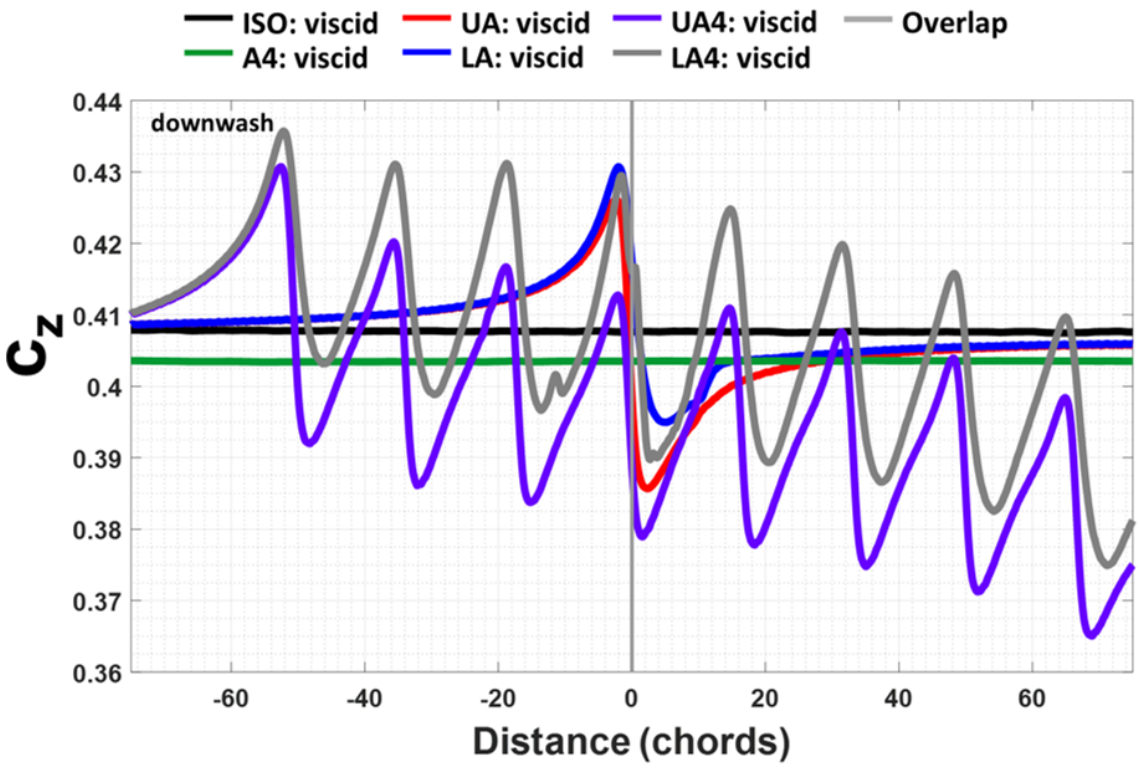

Figure 2.36: Viscid calculations with downwash for an isolated airfoil, two airfoils crossing, single train of eight airfoils crossing ($A4$), and two trains of eight airfoils crossing ($UA4$ and $LA4$), c_z versus distance to overlap (M = 0.25, α = 9.8°,V_i = 31 ft/s, S/c = 4.0 (S = 2.0 ft, c = 0.5 ft), and D/c = 33.51).

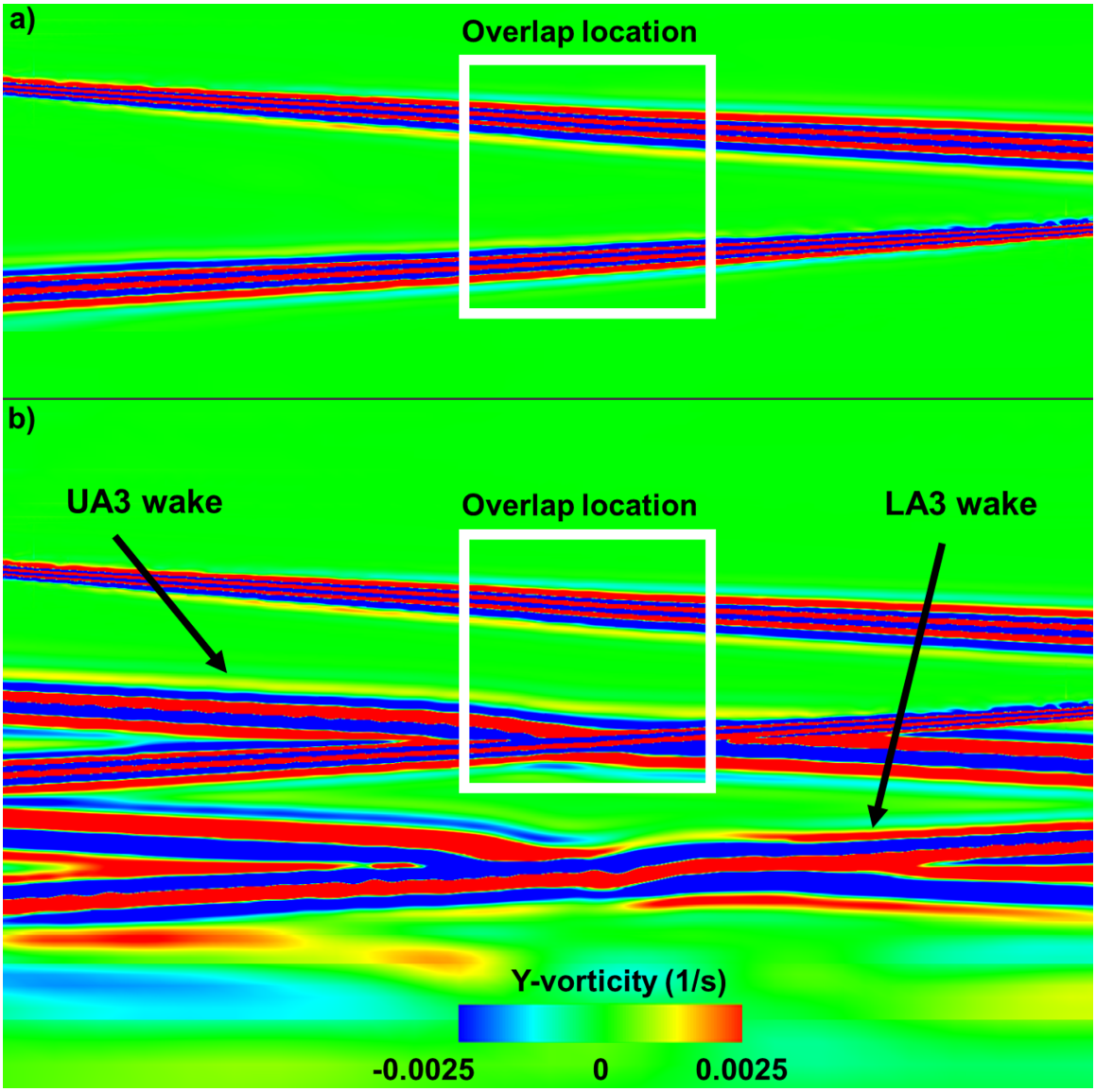

Figure 2.37: Vorticity contour with downwash viscid simulation of a) two airfoils (UA/LA) crossing and b) two trains of eight airfoils crossing after time of overlap of upper and lower airfoil four ($UA4/LA4$) (M = 0.25, α = 9.8°,V_i = 31 ft/s, S/c = 4.0 (S = 2.0 ft, c = 0.5 ft), and D/c = 33.51).

Table 2.8: 2D representation of a coaxial and single rotor r/R location.

r/R	R (ft)	D/c	$V_{r/R}$ (ft/s)	M	θ_{tw} (°)	α (°)	Re #
0.13	2.7	11.142	93.1	0.083	4.94	11.94	3.0x10^5
0.25	5.0	20.944	175	0.157	4.00	11.00	5.6x10^5
0.40	8.0	33.510	280	0.251	2.80	9.80	8.9x10^5
0.50	10.0	41.888	350	0.313	2.00	9.00	1.1x10^6
0.60	12.0	50.265	420	0.376	1.20	8.20	1.3x10^6
0.75	15.0	62.832	525	0.470	0.00	7.00	1.7x10^6
0.80	16.0	67.021	560	0.502	-0.40	6.60	1.8x10^6
0.85	17.0	71.209	595	0.533	-0.80	6.20	1.9x10^6
0.90	18.0	75.398	630	0.564	-1.20	5.80	2.0x10^6
0.95	19.0	79.587	665	0.596	-1.60	5.40	2.1x10^6
1.00	20.0	83.776	700	0.627	-2.00	5.00	2.2x10^6

eight airfoils simulation was used to simulate the coaxial modern rotor in hover (Fig. 2.7 n)).

For a constant chord of 0.5 ft, Table 2.8 shows the 2D representation of a coaxial and single rotor based on radial span r/R location. A varying horizontal distance spacing (D/c), twist (θ_{tw}), and α were used based on span wise location. A downwash of 31 ft/s was applied to the coaxial rotor simulation, as shown in Fig. 2.8, with a rotor separation distance of 2.0 ft.

The modern single rotor in hover 2D representation for airfoil four ($A4$) a) Δ c_l and b) Δ c_d versus distance to overlap is shown in Fig. 2.38 for r/R = 0.25 through 1.00. The mean value of c_l and c_d is subtracted from c_l and c_d to get Δ c_l and Δ c_d. The coaxial rotor hover 2D representation $UA4$ and $LA4$ a) Δ c_l and b) Δ c_x for b) $UA4$ and $LA4$, versus distance to overlap is shown in Fig. 2.39. Spanwise locations for the single and coaxial modern rotors include r/R locations of 0.25, 0.40, 0.50, 0.60, 0.75, 0.80, 0.85, 0.90, 0.95, and 1.00.

Comparing Fig. 2.38 and 2.39 a clear difference is seen with the Δ c_l and Δ c_d between the single and coaxial modern rotor. The single rotor does not change over time, where as the coaxial modern rotor shows an increase before overlap and decrease after overlap for Δ c_l versus distance and vice versa for Δ c_d. The fluctuations in Δ c_l and Δ c_d are due

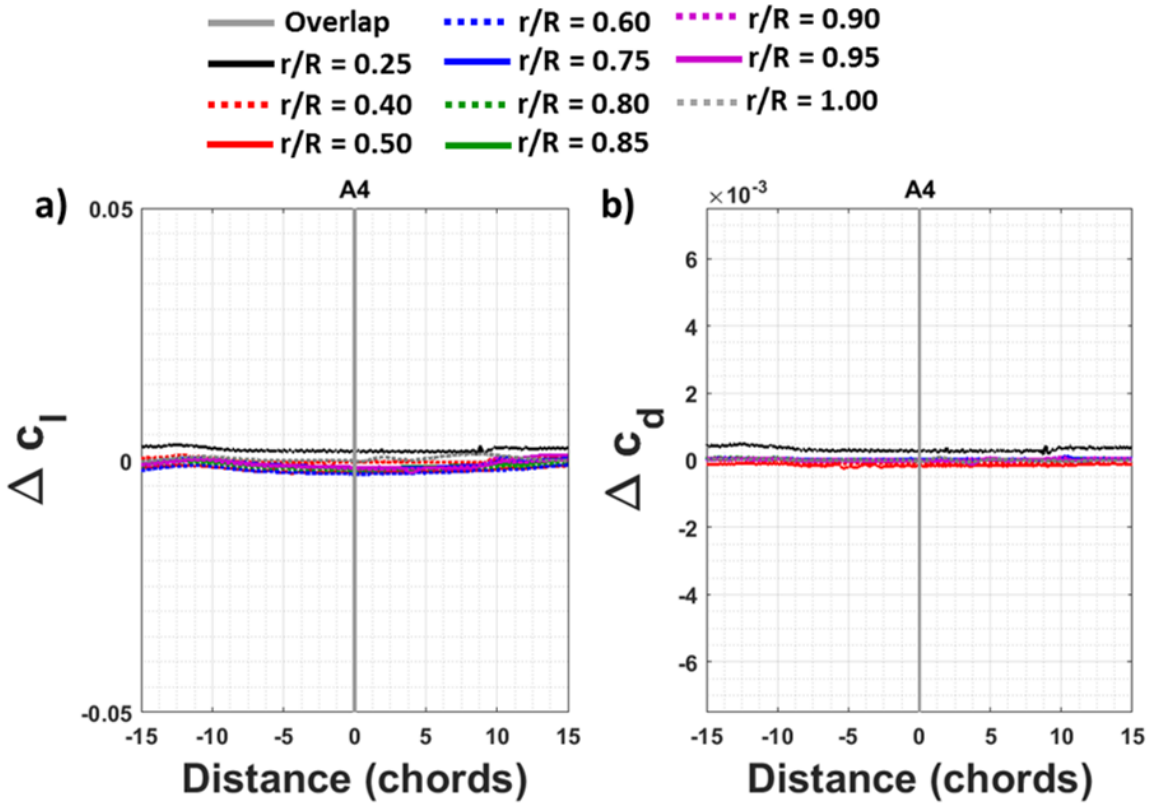

Figure 2.38: Modern single rotor in hover 2D representation for $A4$ a) $\Delta\ c_l$ and b) $\Delta\ c_d$ versus distance to overlap (r/R = 0.25 through 1.00).

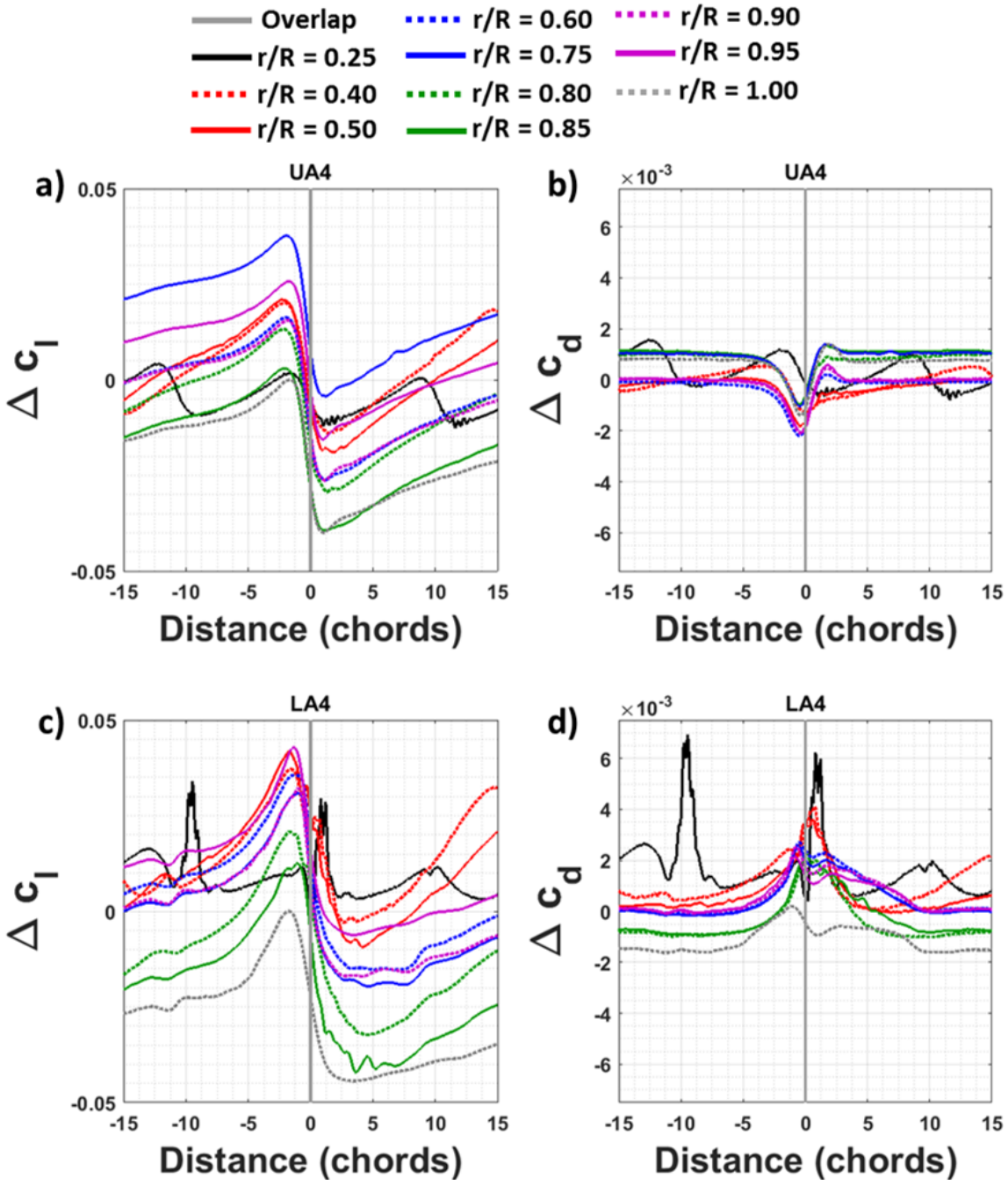

Figure 2.39: 2D representation of modern coaxial rotor in hover a) $\Delta\ c_l$ and b) $\Delta\ c_x$ for b) $UA4$ and $LA4$, versus distance to overlap (r/R = 0.25 through 1.00). Results shown for airfoil four ($A4$).

to the blade crossing occurrences. Results for the single and coaxial modern rotor will be stacked and analyzed to understand the acoustic signature difference between the single and coaxial rotor.

2.4 Summary

A potential and compressible flow computational code was used to understand coaxial rotor specific aerodynamic phenomena in 2D. The effects due to thickness, circulation, compressibility, downwash, and shed vorticity were investigated. The potential code (VITS) was used to understand the flow field during a blade crossing event, where compressibility and downwash are not accounted for. VITS revealed that the lift of both the upper and lower airfoil, increased before overlap, followed by a decrease in lift after overlap. Before overlap, the upper airfoil sees an increase in angle-of-attack due to the upwash from the lower airfoil, while the opposite occurs after overlap.

OVERFLOW 2.2k was used to model an isolated airfoil, two airfoils crossing, single train of eight airfoils, and two trains of eight airfoils crossing. A Mach number sweep for an isolated airfoil is simulated to understand the fundamental aerodynamic effects. The crossing of two airfoils in 2D, offset vertically and traveling in opposite directions are simulated while the angle-of-attack, airfoil thickness, vertical spacing between the airfoils, and Mach number (including transonic and compressible cases) were individually varied to isolate the effects of circulation, thickness, and compressibility. To dissect the effect of downwash and shed vorticity an isolated airfoil, two airfoils crossing, single train of eight airfoils, and two trains of eight airfoils crossing are simulated to isolate each effect. A vertical velocity is simulated to analyze downwash. Furthermore, the difference between viscid and inviscid solutions are compared to analyze shed vorticity to further understand the effect of shed vorticity from a blade crossing event.

The effect of circulation was explored by comparing results for three angles-of-attack with the same symmetrical airfoil, low-speed, and separation distance in order to eliminate

any large effects due to thickness or compressibility. Furthermore, three angles-of-attack with the same symmetrical airfoil, separation distance, but at compressible speeds was explored for comparison. In terms of circulation for low- and high-speed conditions, when comparing angles-of-attack of -7, 0, and 7°, an angle-of-attack of -7 and 7° resulted in a change in c_z (lift), c_x (drag), and c_m (moment) before and after overlap. Comparing -7 and 7°, results showed an equal results for c_x, but and equal and opposite result for c_z and c_m.

Thickness effects are explored by first comparing two different airfoils at a constant low-speed, separation distance, and angle-of-attack flight condition. Furthermore, thickness effects were explored by comparing three different separation distances at a constant low-speed with the same airfoil flight condition, which eliminated large effects of circulation and compressibility. Both comparisons are also explored at a compressible speed. Comparing the two airfoils revealed that at low- and high-speed conditions, thickness effects due to the airfoil were negligible. The same conclusion can be said for separation distances above an S/c of two (or S/D = 0.07), modern day coaxial rotors have an S/c greater than two to avoid thickness effects.

Effects of compressibility are explored by performing a speed sweep (M = 0.50 through 1.20) with the same symmetrical airfoil, angle-of-attack, and separation distance to eliminate any large effects of circulation. As Mach number on the surface of the airfoil increases to Mach 1.0, a large change in c_z, c_x, and c_m is observed due to compressibility and the onset of weak shocks forming.

The effect due to downwash resulted in all viscid and inviscid calculations to see a decrease in lift. For all viscid simulations the addition of downwash increased drag, and decreases moment; the increase in drag is due to the additional force vector that has a direct result on drag.

The single train of eight airfoils showed negligible difference compared to the isolated airfoil, a greater difference is observed when comparing the two trains of eight airfoils crossing, due of the presence of deposited shed vorticity at the location of overlap. Com-

paring the two airfoils crossing to the two trains of eight airfoils crossing, when more airfoils are ahead and behind each other the difference between the two will become significant due to the presence of shed vorticity. By simulating viscid and inviscid y-vorticity contours, it was found that the deposited shed vorticity was pushed downward by the vertical downwash velocity; in turn, the deposited shed vorticity from the upper airfoils directly impacts the lower airfoils.

In conclusion, in terms of circulation, thickness, and compressibility effects the prominent aerodynamic source at low-speed conditions is circulation when two airfoils are crossing in opposite direction. When downwash was introduced the result due to shed vorticity becomes negligible for the upper airfoil, but the lower airfoil is introduced to the upper airfoils deposited vorticity. The addition of downwash reduced the angle-of-attack, and in result minimizes circulation effects for positive angles-of-attack.

CHAPTER 3
3D COAXIAL ROTOR SIMULATION

The performance of a helicopter is dependent on the power of the engine(s) and the lift/thrust that the rotor(s) produce. Compared to a single rotor, the addition of a second rotor results in two wakes interacting, and therefore further complicates the aerodynamic flow field. As discussed in Chapter 2, the 2D simulations for a hovering single rotor and coaxial rotors gave further insight into thickness, circulation, compressibility, shed vorticity, and downwash effects. However, 3D performance effects and forward flight were not explored. In this chapter, a combination of momentum theory and a computational hybrid fluid dynamics (CFD) tool aided in uncovering aerodynamic and acoustic sources based on performance characteristics not revealed in the 2D simulations.

3.1 Rotor Unstructured Navier-Stokes (RotUNS) Performance Validation

Rotor Unstructured Navier-Stokes (RotUNS) operates within the RotCFD Integrated Design Environment (IDE) [62, 63]. RotCFD offers a bridge between comprehensive rotorcraft analysis and CFD analysis. RotUNS is one of several flow solvers within RotCFD, which also includes a geometry module, a semi-automated grid generation module, a rotor module, and a flow visualization and analysis module, all integrated in one environment. Within the RotCFD IDE, grid generation and problem set-up are quickly executed, facilitating parametric sweeps of rotor conditions and problem geometry. RotCFD balances ease of use and practical resource constraints with accurate physical representation of the global flow field.

RotUNS uses 3D incompressible Unsteady Reynolds Averaged Navier-Stokes (URANS) equations and an unstructured grid [62, 63]. Two options are available to model the rotor: actuator disk and discrete blade. Both options rely on user-provided tables of two-

dimensional airfoil coefficients for a range of angle-of-attack and Mach number. Using the computed velocity field and blade element momentum theory, the local angle-of-attack and the Mach number at each blade element section is computed and the aerodynamic coefficients are retrieved from the airfoil tables. For the discrete blade model of the rotor, the section forces and moments are then converted to source terms that are added to the momentum equations at grid points where the blade intersects.

The discrete blade model comprises an individual lifting line representing each blade, in contrast to the disk rotor model. The lifting-line changes location with time. In order to calculate the time-varying rotor sources, the instantaneous location of each rotor blade is found, followed by the calculation of the time-accurate rotor force that the blades exert on specific regions of the flow. Each rotor blade is divided into about 100 source locations and the azimuth position of the blade is assumed to vary linearly with time. At each time step, the starting and ending azimuthal position of a rotor blade are computed and used to find the coordinates of the blade sections and the intersections with the grid cells. The rotor sources are computed similar to the disk model and added to the momentum equations for the grid cell. The solution is then advanced in time.

All performance predictions presented in this chapter were calculated using CAMRAD II and the disk rotor model of RotUNS. The RotUNS calculated pressure fields were generated using the lifting-line (discrete blade) rotor model to assess the effect of individual blades.

3.1.1 CAMRAD II

CAMRAD II [61] is a rotorcraft analysis tool that includes a combination of advanced technologies, including steady calculations. multibody dynamics, nonlinear finite elements, and rotorcraft aerodynamics. The rotor structural-dynamics model is based on beam theory. The rotor-aerodynamics model is based on second-order lifting-line theory (steady two-dimensional airfoil characteristics plus vortex wake), with unsteady aerodynamic forces

from thin airfoil theory, and corrections for yawed flow and swept blades. In CAMRAD II, the rotors were trimmed to zero flapping while adjusting the collective pitch and the lateral and longitudinal cyclic of each rotor with a fixed shaft pitch angle. The HC1 rotor blades were modeled using 17 aerodynamic panels in CAMRAD II, with the panel width ranging from 8% R at the root to 3% R at the tip. Unlike the RotUNS blade model, that used the airfoil distribution shown in Fig. 3.1, the CAMRAD II blade model used a constant NACA 0012 airfoil section. Additional details of the HC1 CAMRAD II model are available from [61].

3.1.2 Harrington single rotor 1 (HS1) and coaxial rotor 1 (HC1)

The performance and aerodynamics of the Harrington single rotor 1 (HS1) and coaxial rotor 1 (HC1) were predicted using RotUNS with the rotor disk model. Comparisons with the Harrington data serve to validate RotUNS for a coaxial rotor system. Although the experimental data for hover [13] and forward flight [16] are available, rotor control setting information is not. Disk model rotor calculations were explored to qualitatively understand the characteristics of the HS1 and HC1 flow field.

Geometry description

The geometry for HS1/HC1 is provided in Table 3.1 and the blade planform as modeled in RotUNS is shown in Fig. 3.1. The difference between the blade geometry of the Harrington experiment [13] and Fig. 3.1 is that the Harrington blades have a continuously varying non-linear distribution of airfoil thickness. At this time, RotUNS does not allow a continuously varying airfoil thickness distribution, so nine NACA airfoils with varying thickness ratios were used to simulate the blades for HS1 and HC1 (see Fig. 3.1). The airfoil tables are interpolated at changing r/R location to determine airfoil sectional c_l, c_d, and c_m as a function of angle-of-attack and Mach number. Airfoil tables were generated using RotCFD's airfoil table generator (AFTGen), which generates airfoil tables in the standard C81 format

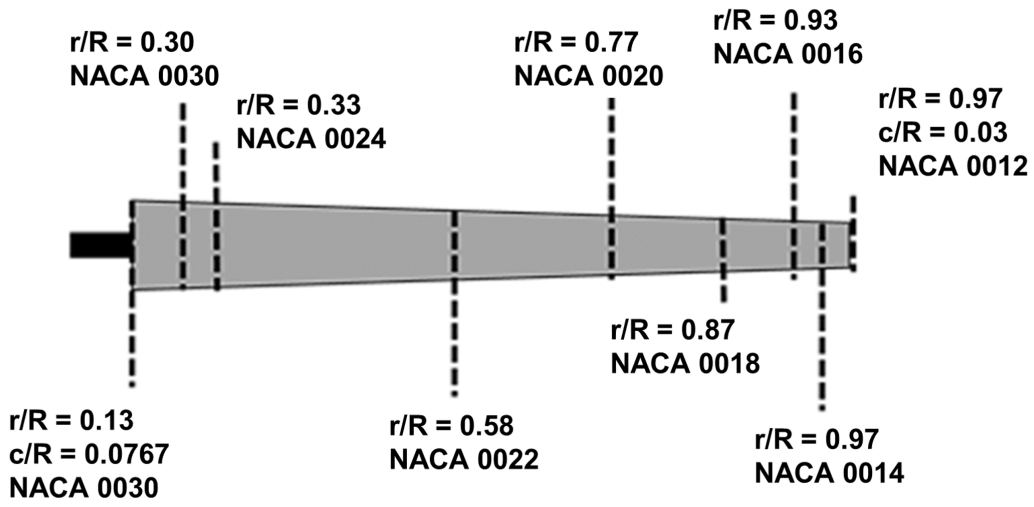

Figure 3.1: HS1/HC1 blade planform geometry as modeled in RotUNS.

using geometry and user prescribed airfoil inputs. AFTGen is used for all RotUNS and BEMT calculations.

3.1.3 Harrington single rotor 1 (HS1) hover performance

Figure 3.2 shows RotUNS, BEMT, and CAMRAD II hover calculations compared with measurements by Harrington [13] for the HS1 rotor for a collective pitch range from 1.5° to 9°. The BEMT predictions are based on Leishman's single-rotor blade element model [12]. In Fig. 3.2, BEMT is under-predicting thrust for high values of power due to BEMT assumptions [64]. The RotUNS and CAMRAD II calculations compare well with the Harrington [13] data.

3.1.4 Harrington coaxial rotor 1 (HC1) hover performance

Figure 3.3 compares performance measurements [13] with predictions from RotUNS, RotUNS: Grid Adaption (GA), CAMRAD II, and the BEMT analysis for the HC1 system. Grid adaption, based on vorticity, was used for a few of the cases in anticipation of the complex interaction between the upper and lower rotor. The use of GA redefines and re-

Table 3.1: HS1/HC1 parameters [13].

Parameter	Harrington rotor 1
R, Radius (ft)	12.5
Number of blades (per rotor)	2
c, Chord (ft)	varying
Z, rotor separation (ft)	2.33
V_{tip}, Tip speed, hover (ft/sec)	500
Tip speed, forward flight (ft/sec)	469
Solidity	0.054
Solidity per rotor	0.027
Twist	None
Taper	linear distribution
Airfoils (thickness ratio)	non-linear distribution
Cutout radius (r/R)	0.133
Hinge offset (r/R)	0.133
Upper rotor direction (HS1/HC1)	Clockwise
Lower rotor direction (HC1)	Counter-Clockwise

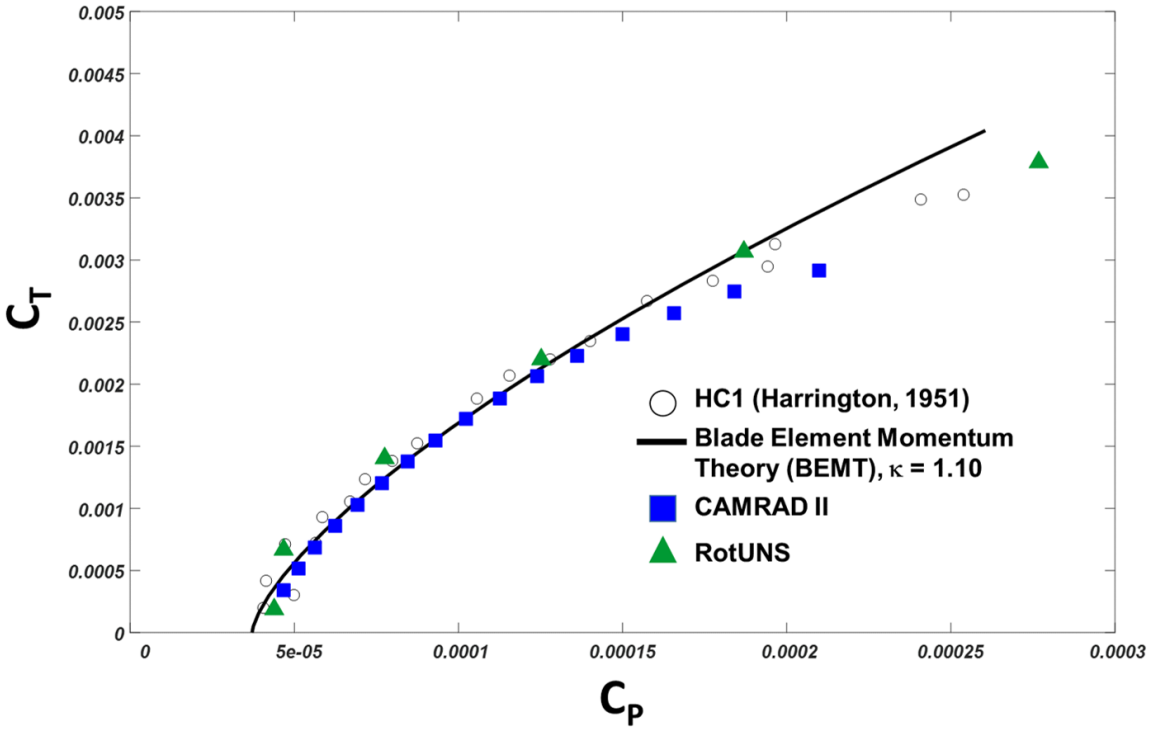

Figure 3.2: Measured and calculated performance of the single rotor, HS1 [13] in hover.

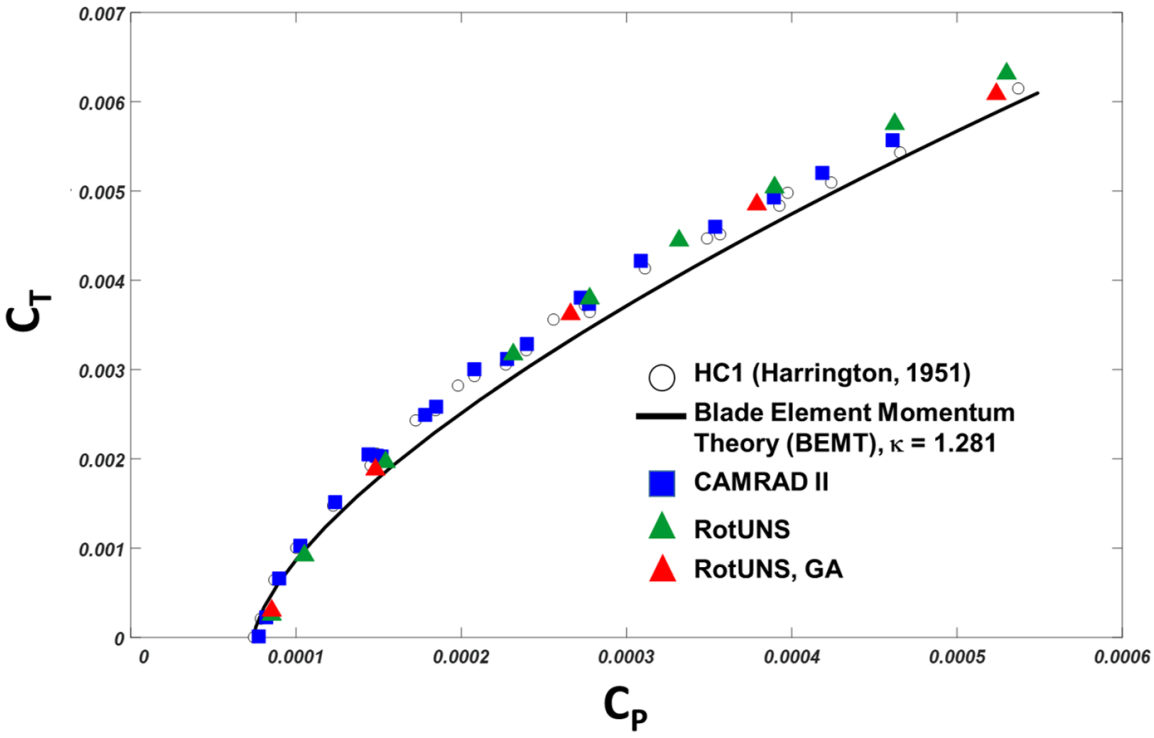

Figure 3.3: Performance of HC1[13] in hover compared with momentum theory, BEMT and RotUNS rotor disk model calculations.

fines the mesh over time, allowing flow features to be captured with greater fidelity. In Fig. 3.3, BEMT calculations under-predicted the measurements and RotUNS calculations due to the BEMT input of κ_{int} and c_d. CAMRAD II calculations were closest to the experimental data compared to RotUNS and BEMT, this is due to the addition of section profile drag that was added as part of the shaft power calculation in CAMRAD II, resulting in calculations that closely match experimental data. The BEMT calculations for HC1 and HS1 at low collective settings closely match, as collective setting increase RotUNS calculations compared better compared to BEMT calculations [12].

Collective settings for the upper and lower rotor were determined through an iterative process to achieve a torque-balanced solution. As shown in Table 3.2, torque balance was achieved for most of the cases by increasing the collective of the lower rotor by 0.2° compared to the upper rotor. Table 3.2 provides the percent torque difference between

Table 3.2: HC1 hover RotUNS rotor disk model control inputs (* with grid adaptions (GA)).

θ_U (deg)	θ_L (deg)	% diff in Q
1.5	1.5	0.28
1.5*	1.5*	0.56
3.0	3.2	0.45
5.0	5.2	0.75
5.0*	5.0*	3.28
7.0	7.2	0.19
8.0	8.2	0.19
8.0*	8.0*	2.21
9.0	9.2	0.57
10.0	10.2	0.95
10.0*	10.0*	1.27
11.0	11.0	0.38
11.9	12.0	0.91
12.0*	12.0*	0.18

the upper and lower rotors; for the present work, a difference of $< 1\%$ was considered a balanced system. The thrust for the coaxial lower rotor is less than the coaxial upper rotor which is due to the increased inflow seen by the lower rotor from the upper rotor [12].

The BEMT used the same geometry assumptions as the RotUNS calculations while using a coaxial interference-induced power factor from Leishman's Case 4a [12, 14]. Leishman's Case 4a assumes that the rotors have balanced torque with the lower rotor operating in the slipstream of the upper rotor.

RotUNS with grid adaption shows an improvement at higher collective settings, but little or no change at lower thrust. Differences between Harrington's [13] data and computational simulations can be due to blade modeling. The blades were not individually modeled but rather the rotor was modeled as a disk with distributed momentum sources. Furthermore, the actual Harrington's HS1 and HC1 had smooth airfoil (thickness to chord) transitions, unlike the geometry that was used by RotUNS and BEMT.

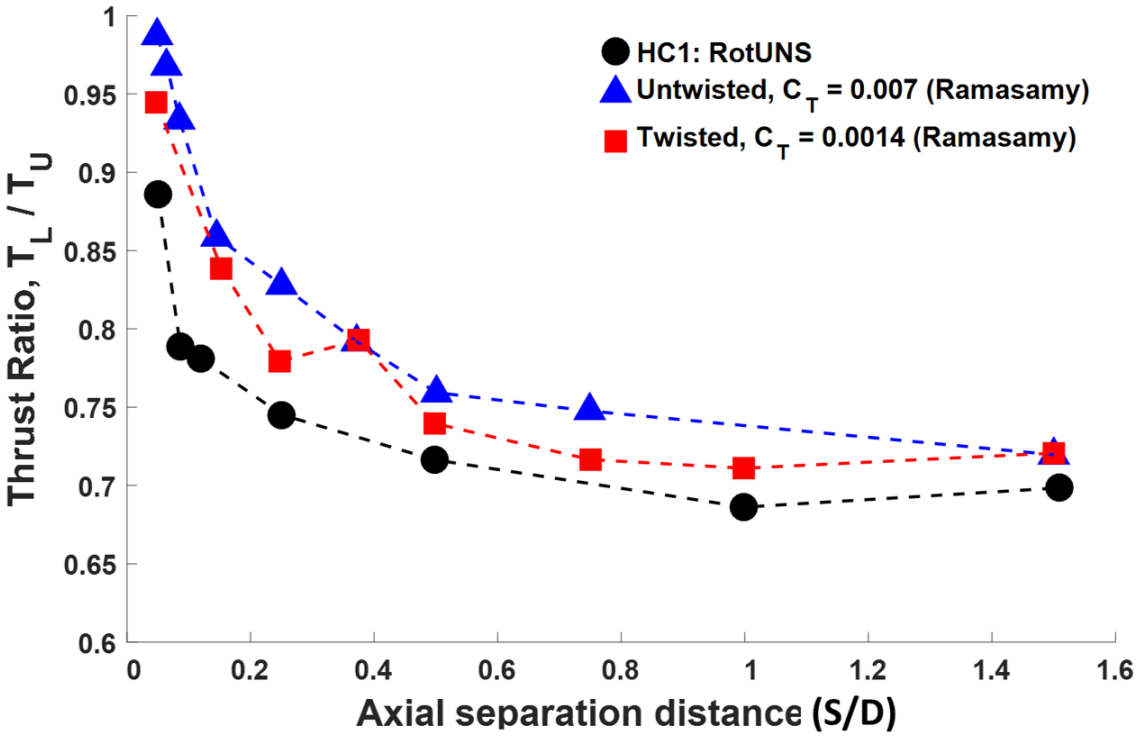

Figure 3.4: Thrust ratio versus rotor separation distance in hover comparing HC1 RotUNS rotor disk model calculations and Ramasamy's [9] experimental data for untwisted blades.

Rotor vertical separation distance variation:

The performance of HC1 was explored from 0.05 to 1.5 S/D, where S is the vertical distance between the two rotors. Figure 3.4 reveals that as separation distance increased the ratio between thrust of the lower rotor (T_L) and upper rotor (T_U) decreases, for balanced torque and constant total thrust coefficient, eventually becoming independent of separation distance. Measurements by Ramasamy [9] for two different total thrust coefficients (and blade geometry) show similar trends as the calculations, lending confidence in RotUNS prediction capability.

As previously mentioned, the RotUNS rotor collective pitch settings were determined through an iterative process to achieve a torque-balanced solution; the percent difference in torque for calculations in Fig. 3.4 is shown in Table 3.3.

Table 3.3: HC1 hover RotUNS rotor disk model control inputs for varying separation distance.

Z/D	θ_U (deg)	θ_L (deg)	% diff in Q
0.050	7.0	7.0	1.79
0.093	7.0	7.0	1.77
0.125	7.0	7.2	0.65
0.250	7.0	7.25	0.89
0.500	7.0	7.2	1.86
1.000	7.0	7.10	1.48
1.500	7.0	7.10	0.81

3.1.5 HS1 and HC1 forward flight performance

For forward flight predictions, trim settings for the HC1 rotor were required. Here, RotUNS relied on trim control solutions provided by CAMRAD II [41]; the settings are provided in Table 3.4 and Table 3.5 for HS1 and HC1, respectively for a trim target of balanced torque.

Figure 3.5 shows the measured forward flight performance of HS1 and HC1 [16] compared to CAMRAD II and RotUNS calculations. RotUNS calculations for HS1 are closer to the experimental data compared to CAMRAD II calculations, while CAMRAD II calculations for HC1 are closer to experimental data compared to RotUNS HC1 calculations. CAMRAD II and RotUNS percent error difference for HS1 and HC1 experimental data is shown in Table 3.6. Percent error is calculated using equation 3.1. CAMRAD II HS1 calculations resulted in a larger difference compared to RotUNS HSI calculations, while RotUNS HSI calculations resulted in a larger difference compared to CAMRAD II HS1 calculations.

$$\%error = \frac{|experimental - computational|}{experimental} \times 100 \tag{3.1}$$

The two analysis use different airfoil distributions with RotUNS providing an airfoil thickness distribution that is more representative of the rotor [41]. For each airfoil, a C81Gen was used to generate airfoil tables that were read by RotUNS, while CAMRAD II

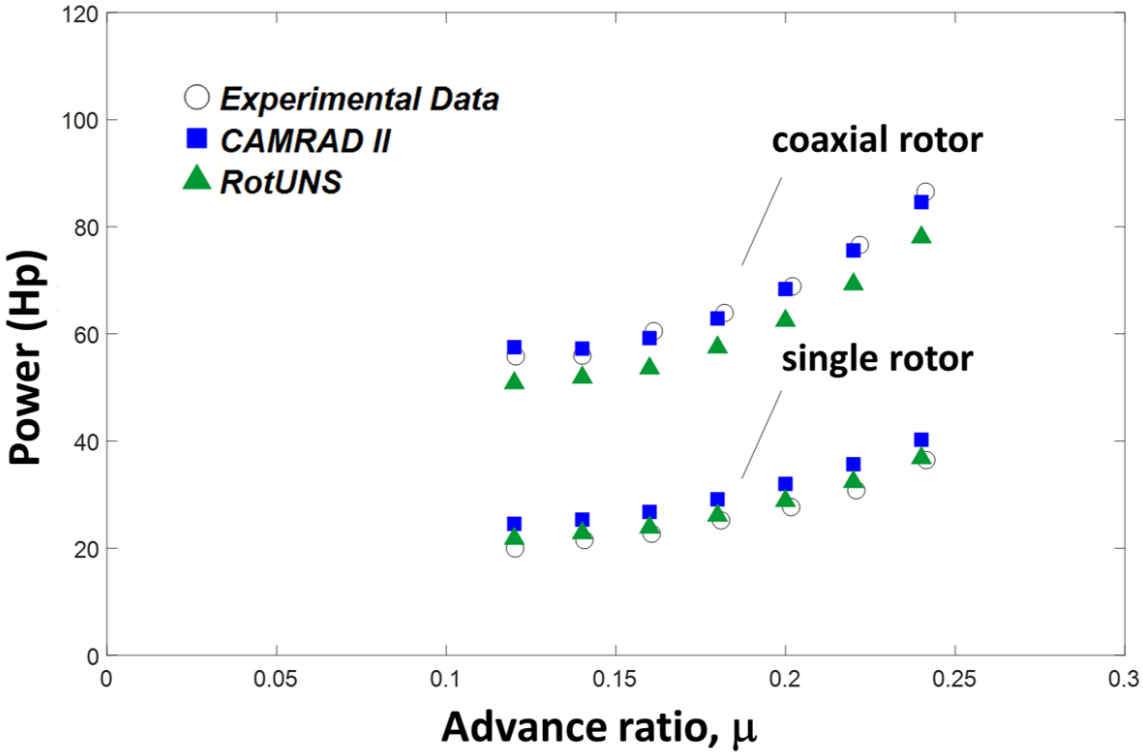

Figure 3.5: Measured performance of HS1 and HC1 [16] in forward flight compared with CAMRAD II and RotUNS calculations.

Table 3.4: HS1 forward flight RotUNS inputs using CAMRAD II control settings [41].

μ	α_S	θ	θ_{1s}	θ_{1c}
0.12	-2.18	7.31	-2.51	0.63
0.14	-2.87	7.50	-2.93	0.48
0.16	-3.66	7.82	-3.37	0.38
0.18	-4.53	8.27	-3.87	0.32
0.2	-5.48	8.83	-4.41	0.25
0.22	-6.49	9.51	-5.03	0.21
0.24	-7.57	10.33	-5.73	0.17

Table 3.5: HC1 forward flight RotUNS inputs using CAMRAD II control settings [41].

μ	α_S	θ	θ_{1s}	θ_{1c}
Lower rotor				
0.12	-2.16	7.98	-2.43	1.32
0.14	-2.85	8.03	-2.89	0.99
0.16	-3.64	8.27	-3.35	0.81
0.18	-4.51	8.67	-3.85	0.69
0.20	-5.47	9.19	-4.36	0.63
0.22	-6.46	9.85	-5.07	0.55
0.24	-7.53	10.65	-5.75	0.50
Upper rotor				
0.12	-2.16	8.07	-2.75	1.05
0.14	-2.85	8.08	-3.12	0.84
0.16	-3.64	8.31	-3.55	0.69
0.18	-4.51	8.69	-4.03	0.59
0.20	-5.47	9.21	-4.57	0.50
0.22	-6.46	9.87	-5.19	0.42
0.24	-7.53	10.68	-5.90	0.36

used a NACA 0012 airfoil table. Also, an increment to the section profile drag was added as part of the shaft power calculation in CAMRAD II. The computed torque from RotUNS for the upper and lower rotor torque for each advance ratio differed by less than 0.50%. In both RotUNS and CAMRAD II calculations the rotor shank (r/R = 0 to 0.133) is not modeled. Furthermore, CAMRAD II used a wake model, while RotUNS directly calculated the wake. Further investigation regarding the difference between HS1 and HC1 RotUNS and CAMRAD II calculations should be performed for both hover and forward flight, including induced drag, profile drag, and parasite drag differences.

Table 3.6: CAMRAD II and RotUNS percent error difference for HS1 and HC1 experimental data.

	HS1		H1C	
μ	CAMRAD II (%)	RotUNS (%)	CAMRAD II (%)	RotUNS (%)
0.12	22.69	9.32	3.00	8.88
0.14	17.71	6.17	2.21	7.27
0.16	18.01	5.02	2.27	11.55
0.18	15.66	3.61	1.65	10.16
0.20	15.89	4.48	0.70	9.19
0.22	15.76	5.06	1.29	9.45
0.24	10.77	1.26	2.33	9.91

3.1.6 Pressure distribution above and below rotor

As previously mentioned, RotUNS's discrete-blade option models the rotor blades as a lifting-line, because of this the flow field above and below the rotors are analyzed. A single rotor was analyzed first and then a coaxial rotor for hover and forward flight. The Harrington rotor 1 was simulated with all rotors (single, upper/lower rotor) set to a collective pitch of 7°.

The pressures above and below the rotor(s) are shown in Figs. 3.6 through 3.9, which represent the absolute pressure normal to the surface at the closest flow field grid point for HS1 and HC1. The figures simply illustrate the pressure change (lower or higher) as blades from the upper and lower rotors pass in opposite directions.

The absolute pressure below and above a single isolated rotor is shown in Fig. 3.6 a) when the blades are at 0° ($B1$) and 180° ($B2$). A low pressure is evident above both blades and a high pressure below the blades, providing a positive upward thrust. Figure 3.6 b) shows time histories of pressure just above and below blade $B1$ at r/R = 0.85 in the rotating frame; the pressure remains essentially constant throughout one revolution.

When a second rotor is introduced, the flow field becomes complex, as shown in Figs. 3.7 through 3.9. The absolute pressure below and above each rotor of HC1 is presented in Fig. 3.7 and 3.8. In both Figs 3.7 and 3.8, the pressure above the upper rotor is the top-left figure and the pressure below the upper rotor is the bottom-left figure. The

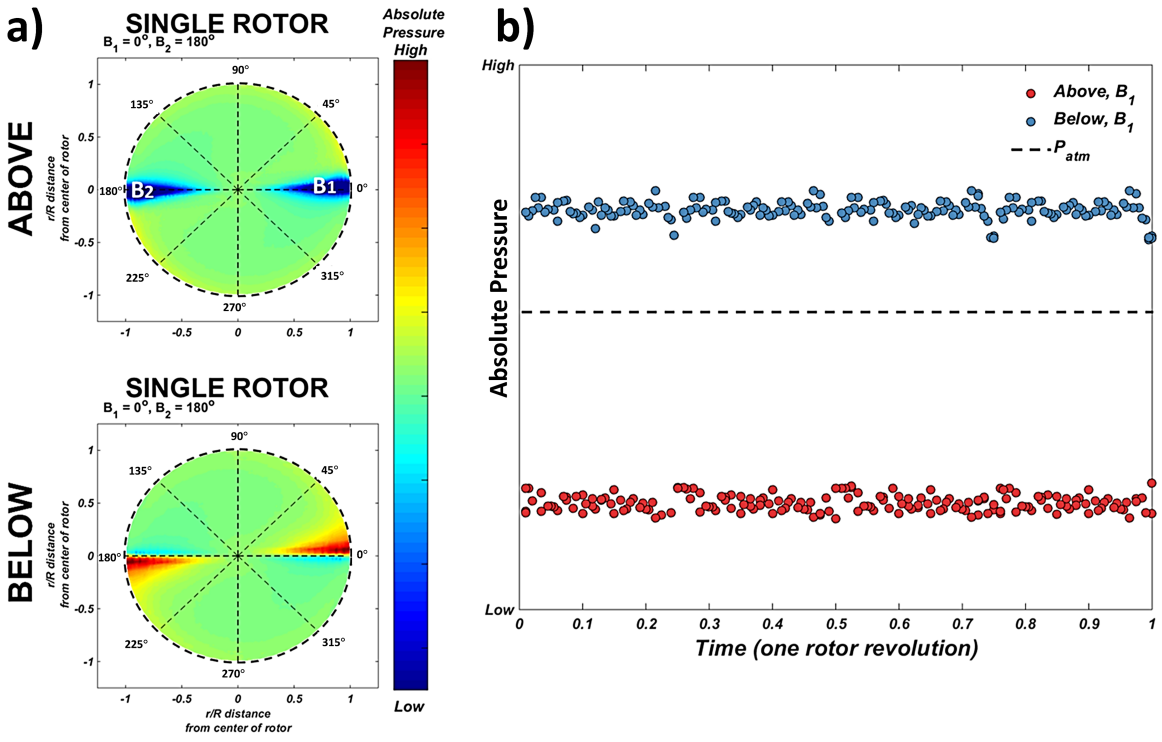

Figure 3.6: HS1 flow field absolute pressures a) below and above rotor and b) time history (one revolution) at r/R = 0.85 in hover (RotUNS lifting-line (discrete blade) rotor model calculations).

pressures above and below the lower rotor are represented by the upper- and lower-right figures, respectively.

Figure 3.7 shows an instance when the blades of the upper and lower rotor are not overlapped. The upper rotor blades are at 0° ($U1$) and 180° ($U2$) and the lower rotor blades are at 90° ($L1$) and 270° ($L2$). The presence of the lower rotor is seen at 90° and 270° in the upper rotor pressure contours, which reveals the influence of the pressure above the lower rotor. The same is also seen for the pressure above and below the lower rotor, where the pressure below the upper rotor is seen at 0° and 180°. For both upper and lower rotors, a low pressure is seen at the location of the blades above and high pressure below the rotors, giving rise to a positive upward thrust.

Figure 3.8 shows an instance when the upper and lower blades are overlapped at 45° ($U1$) and 135° ($U2$) for the upper rotor and 45° ($L1$) and 225° ($L2$) for the lower rotor. In comparison to Fig. 3.7, when the blades are not overlapped, a difference in pressure below and above is seen in Fig. 3.8. When the blades are overlapped, the pressure above the upper rotor decreases. A decrease in pressure below is also seen for the upper rotor. The opposite is seen for the lower rotor, where the pressure above and below have an increase in pressure.

The time histories of the pressure above and below the upper and lower rotor blades at r/R of approximately 0.85 in the rotating frame are presented in Fig. 3.9 for hover. The gray vertical line indicates the time of blade overlap. For both the upper and lower rotors, a change in pressure is seen at the time of blade overlap. Blade two ($U2$) of the upper rotor experiences an overall decrease in pressure due to the low-pressure field generated from Blade one ($L1$) of the lower rotor. Conversely, $L1$ experiences an increase in pressure due to the high-pressure field of $U2$. Comparing Fig. 3.9 to Fig. 3.6 b), an aerodynamic interaction is seen between the upper and lower rotor in the coaxial rotor system, unlike the single rotor.

The pressure above and below a rotor in forward flight at $\mu = 0.12$ is analyzed using the

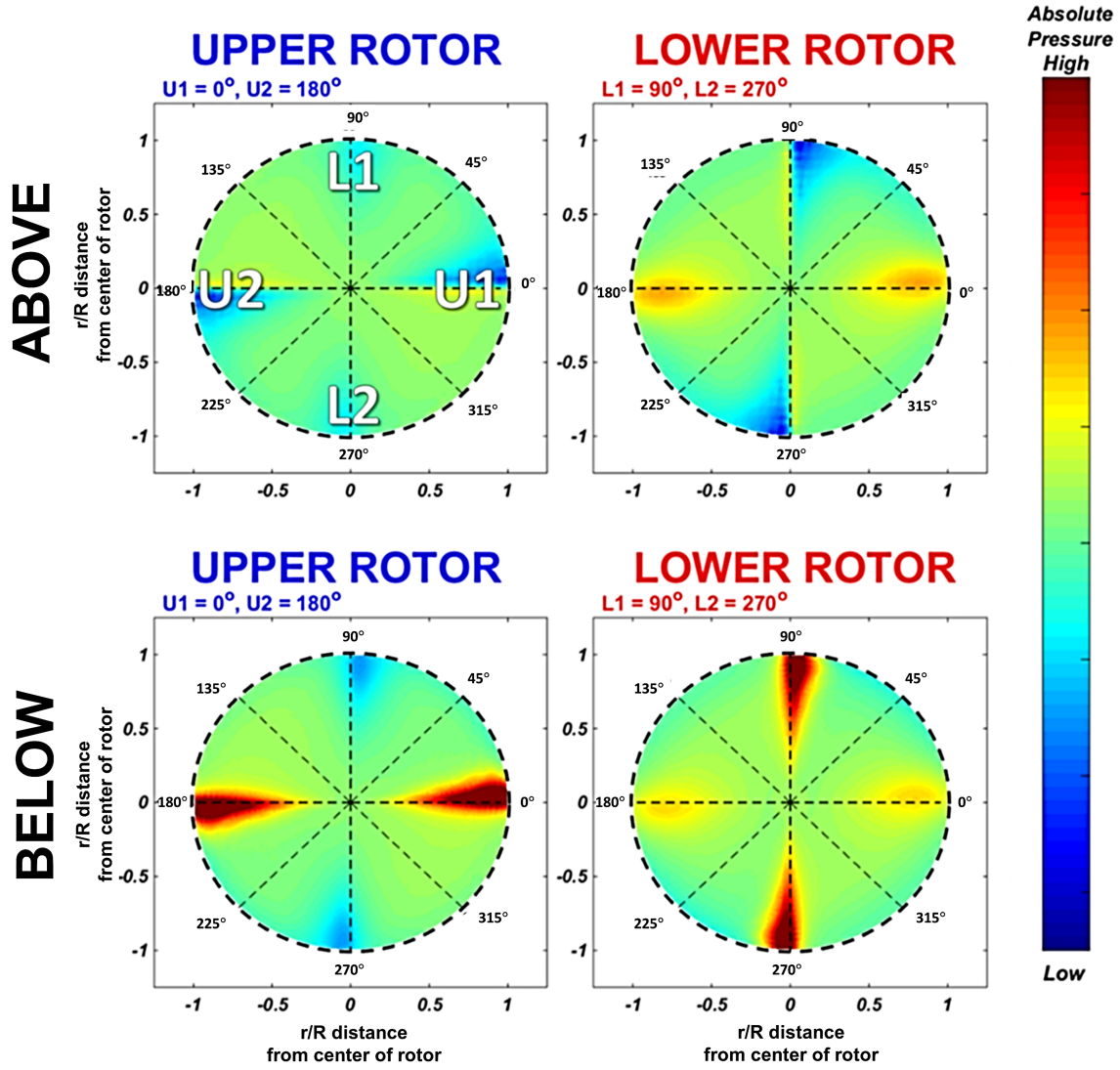

Figure 3.7: HC1 comparison of upper and lower rotor of absolute pressure below and above rotor, respectively, at non-overlap. RotUNS lifting-line (discrete-blade) rotor model calculations are presented for hover.

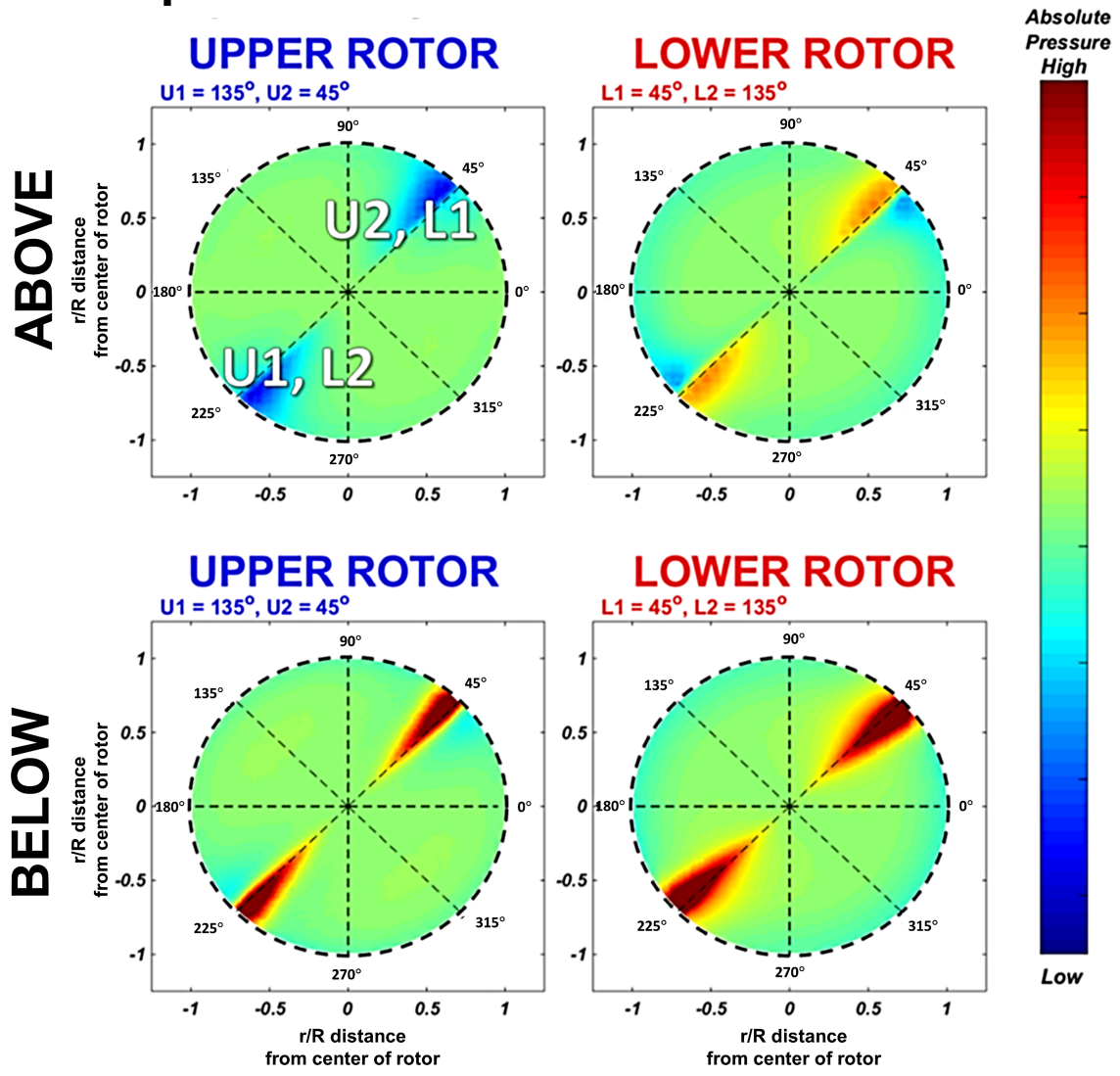

Figure 3.8: HC1 comparison of upper and lower rotor of absolute pressure below and above rotor, respectively, at overlap. RotUNS lifting-line (discrete-blade) rotor model calculations are presented for hover.

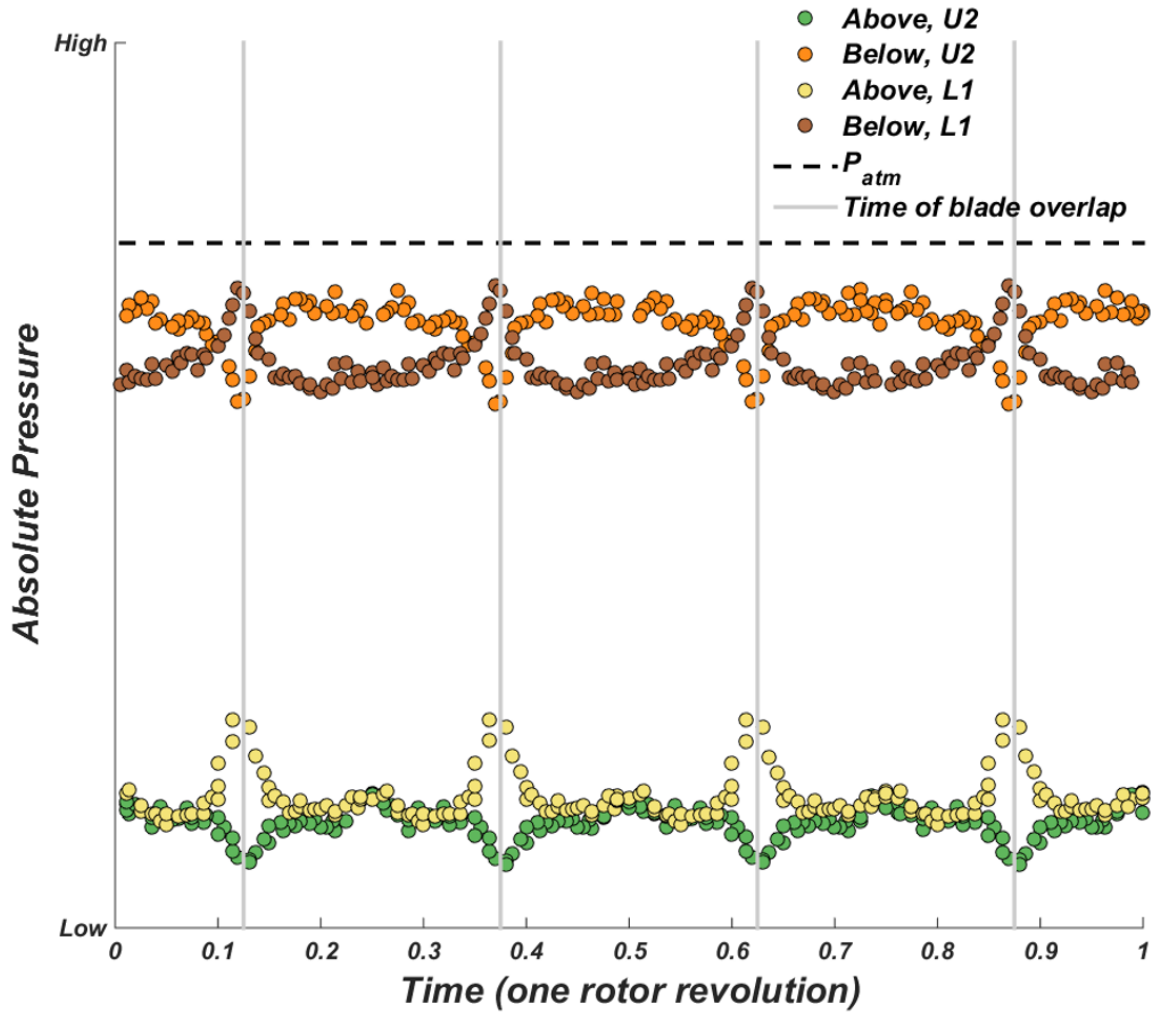

Figure 3.9: Time history (one revolution) at r/R = 0.85 for absolute pressure below and above $U2$ (upper rotor blade two) and $L1$ (lower rotor blade one) in hover.

discrete-blade option of RotUNS. HS1 was analyzed first and then HC1. Control settings for HS1 and HC1 are shown in Table 3.4 and Table 3.5.

The pressures above and below the rotor(s) are shown in Figs. 3.10 through 3.12, which represent the absolute pressure normal to the plane of the rotor at the closest flow field grid point for HS1 and HC1.

The absolute pressure below and above each rotor of HC1 is presented in Figs. 3.10 and 3.11. In both figures, the pressure above the upper rotor is the top-left figure and the pressure below the upper rotor is the bottom-left figure. The pressures above and below the lower rotor are represented by the upper- and lower-right figures, respectively.

Figure 3.10 shows an instance when the blades of the upper and lower rotor are not overlapped. The upper rotor blades are at 0° ($U1$) and 180° ($U2$) and the lower rotor blades are at 90° ($L1$) and 270° ($L2$). The presence of the lower rotor is seen at 90° and 270° in the upper rotor pressure contours, which reveals the influence of the pressure above the lower rotor. The same is also shown for the pressure above and below the lower rotor, where the pressure below the upper rotor is seen at 0° and 180°. For the upper rotor, the blades ($U1$ and $U2$) experience a lower pressure above and higher pressure below, resulting in a positive upward thrust. A similar result is shown for $L1$ and $L2$.

Figure 3.11 shows an instance when the upper and lower blades are overlapped at 45° ($U1$) and 135° ($U2$) for the upper rotor and 45° ($L1$) and 225° ($L2$) for the lower rotor. Compared to Fig. 3.10, the pressure above and below the upper rotor decreases when the blades overlap. The opposite is seen for the lower rotor, where the pressure above and below increase compared to the non-overlapped case (Fig. 3.10).

The 3D RotUNS HC1 calculations reveal that at the time of blade crossing the lower rotor blades enter a region of high pressure due to the pressure below the upper rotor (high pressure), and in turn an overall increase in absolute pressure on the lower rotor blades is seen. Also at the time of blade crossing, the upper rotor blades enter a region of lower pressure due to the pressure above the lower rotor (low pressure), the upper rotor blades

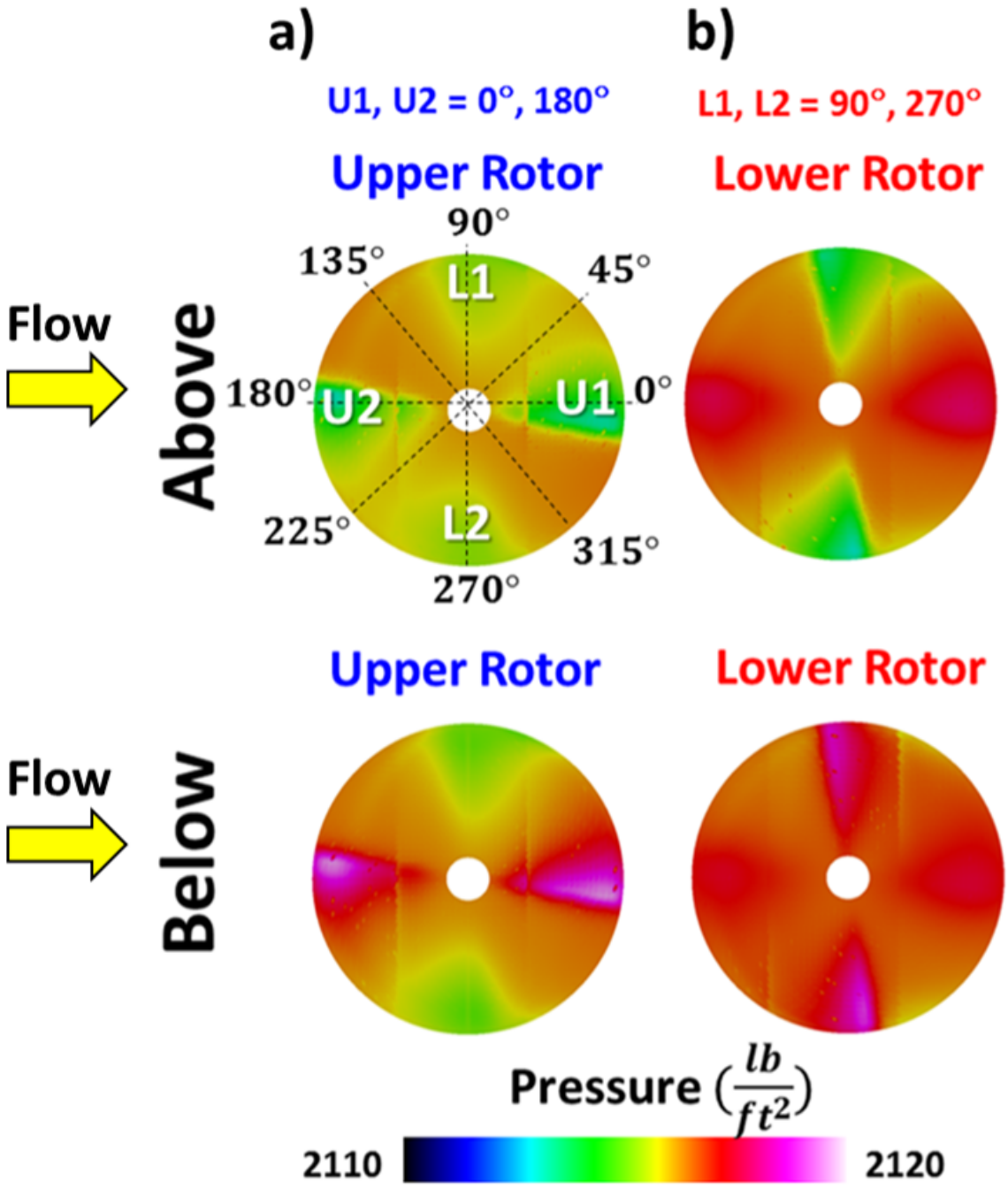

Figure 3.10: HC1 flow field absolute pressures below and above rotor at two instances in time when blades are not overlapped, for a) upper rotor where $U1$, $U2$ = 0°, 180° and b) lower rotor, where $L1$, $L2$ = 90°, 270° (RotUNS forward flight lifting-line (discrete blade) rotor model calculations) in forward flight (μ = 0.12).

see an overall decrease in absolute pressure at this time. The conclusion from the 2D OVERFLOW blade crossing simulation are consistent with the 3D results.

Previously Barbely et al. [27] analyzed the pressure distribution above and below the upper and lower rotor in hover for HC1. The pressure above the lower rotor in forward flight and hover is shown in Fig. 3.12 with the lower rotor blades were at 90° and 270°. The pressure scale for the hover and forward flight case are different. The pressure field in hover is symmetrical, while the forward flight case is not.

Wake dissipation effects:

Vortex diffusion is a critical issue with all computational simulations of rotor wakes. Being able to track the projection of the rotor wakes is needed to understand information regarding possible blade-vortex interactions (BVI). Using resolution enhancements in the grid, vortices can be preserved longer. Kim and Brown [18] conducted a computational investigation using the Vorticity Transport Model (VTM) developed by Brown while coupled with a lifting-line representation of the blade. Without the use of grid adaption in RotUNS, the tip vortices are not discernible after approximately 120 degrees of vortex age although the calculation represents 50 rotor revolutions. RotUNS was run with grid adaption (GA) for a small set of thrust/collective settings. The grid was automatically refined in areas of high vorticity and coarsened in areas of low vorticity.

The use of GA resulted in an improved agreement between rotor performance predictions and experimental data as compared to the RotUNS baseline grid results shown Fig. 3.3. However, not all of the GA cases are as well torque-balanced as the baseline grid cases. In summary, the baseline grid is sufficient for performance predictions, but a detailed study of wake interactions will require grid adaption or a finer baseline grid to investigate possible BVIs.

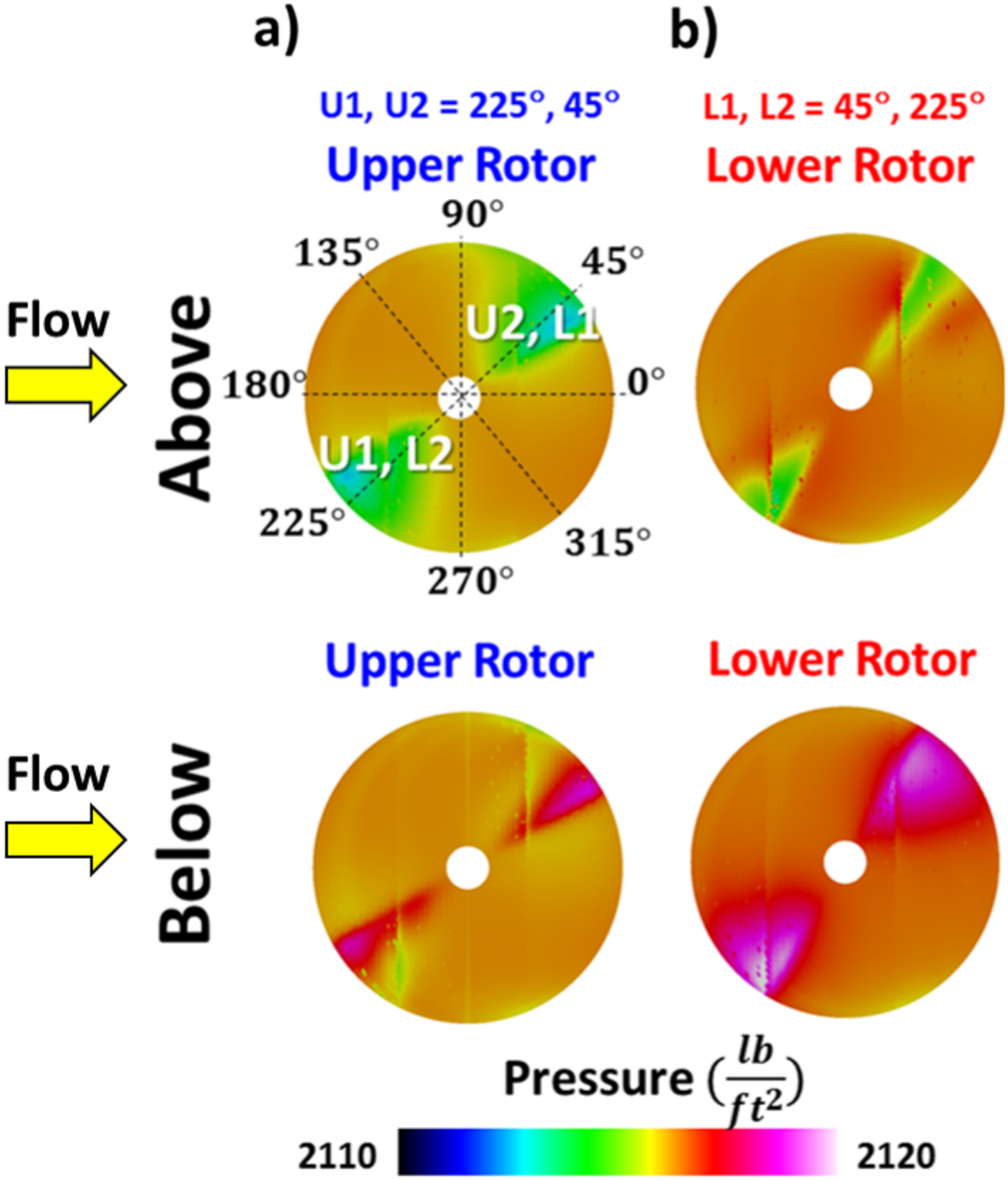

Figure 3.11: HC1 flow field absolute pressures below and above rotor at two instances in time when blades are overlapped for a) upper rotor where $U1$, $U2$ = 225° , 45° and b) lower rotor, where $L1$, $L2$ = 45° , 225° (RotUNS forward flight lifting-line (discrete blade) rotor model calculations)in forward flight (μ = 0.12).

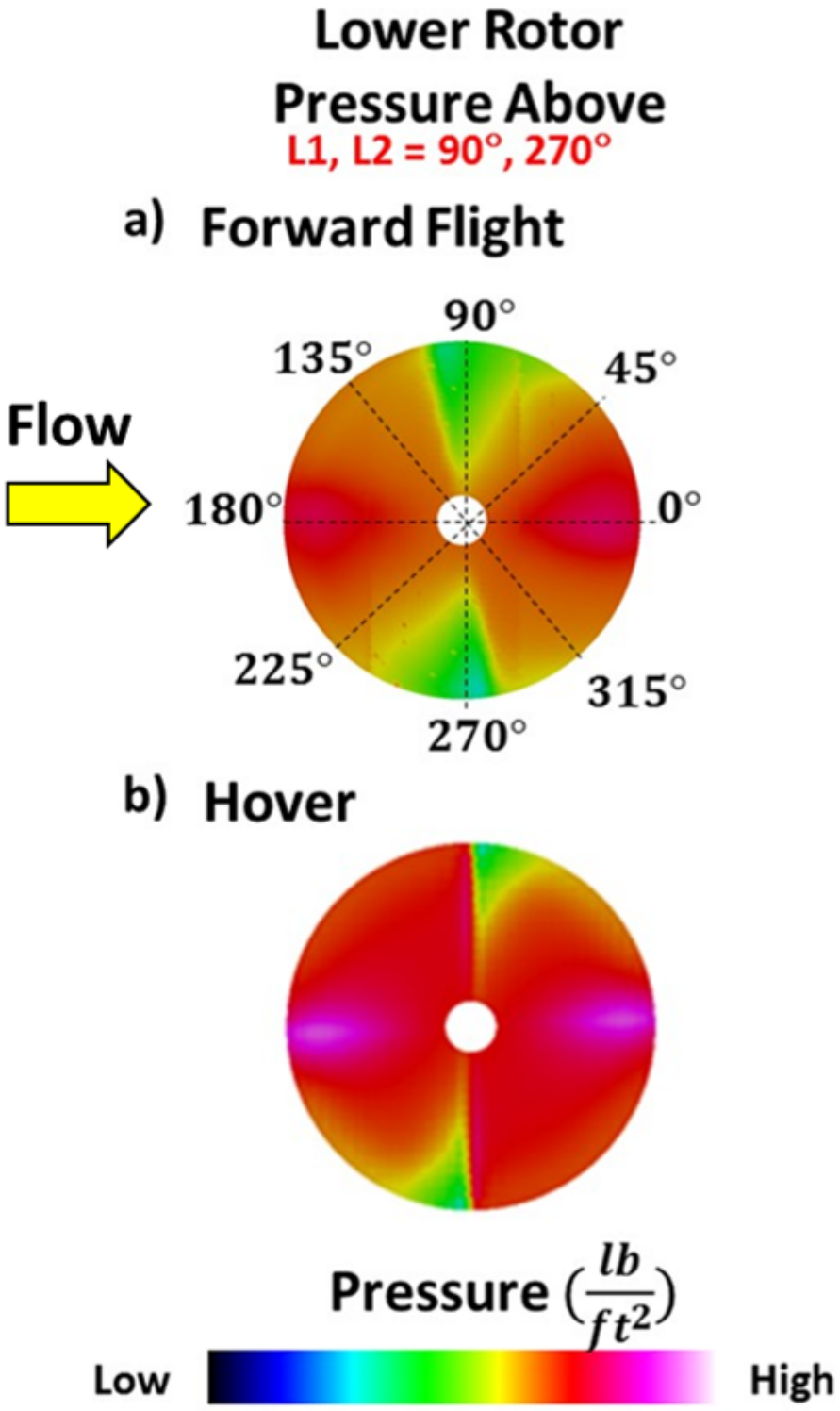

Figure 3.12: HC1 rotor flow field absolute pressures above lower rotor blades where $L1$, $L2 = 90°, 270°$ for a) forward flight and b) hover (RotUNS lifting-line (discrete blade) rotor model calculations).

3.2 Comparison of 2D and 3D results

As shown in Figs. 3.10 through 3.12, the pressure distribution above and below the rotors of the Harrington coaxial and single rotor further validates the change in aerodynamic loading on a blade when two rotor blades cross as discussed in Chapter 2. RotUNS and 2D OVERFLOW hover (Chapter 2) results for the modern rotor design are compared (see Table 2.2) at a span location of r/R = 0.90, see Fig. 3.13 for OVERFLOW c_l versus azimuth (y-axis on left in red) and RotCFD C_L versus azimuth (y-axis on left in blue). The 2D hover OVERFLOW results include shed vorticity and downwash effects. Both simulations show an increase in lift before overlap and decrease in lift after overlap. Before overlap, the upper airfoil sees an increase in angle-of-attack due to the up-wash from the lower airfoil. The angle-of-attack of the lower airfoil also increases due to the up-wash from the upper airfoil and therefore an increase in lift is experienced by both airfoils, while the opposite occurs after time of overlap. Both LA4 and L1 see a larger change in lift before overlap compared to UA4 and U1. Differences between the two simulations are seen due to the difference in airfoil/blade modeling, RotUNS models the blade at a lifting line, where as 2D OVERFLOW modeled the blade r/R location as an airfoil. RotUNS is unable to model thickness effects, but is able to calculate performance characteristics unlike 2D OVERFLOW.

3.3 Summary

RotUNS gives the ability to model a 3D coaxial rotor that gives insight into performance differences between a single and coaxial rotor, in hover and forward flight. The 2D OVERFLOW simulation only modeled a hovering rotor, whereas 3D RotUNS was able to expand to forward flight. The 2D OVERFLOW calculations gave direct 2D information regarding the aerodynamics, whereas the 3D RotUNS results gave performance calculations with minimal insight into the rotors aerodynamics. RotUNS was validated and parametric stud-

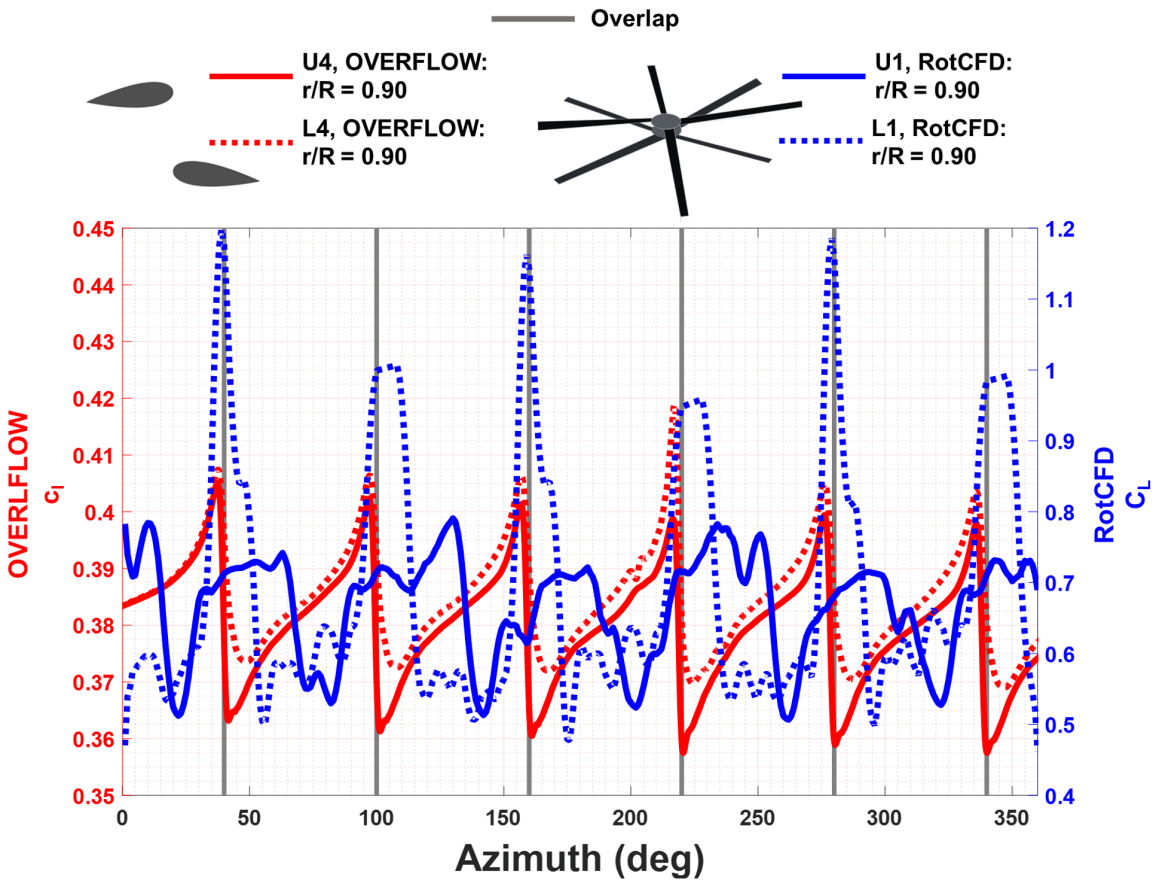

Figure 3.13: Comparison between OVERFLOW 2D and 3D RotCFD coaxial modern rotor in hover at r/R = 0.90 for upper rotor blade one (U1), lower rotor blade one (L1), upper airfoil four (UA4), and lower airfoil four (LA4) (OVERFLOW conditions: M = 0.564, α = 5.8°, S/c = 4.0 (S = 2.0 ft, c = 0.5 ft), and D/c =75.4 ft, RotCFD conditions: V_{tip} = 700 ft/s), α = 5°, and S/c = 4.0 (S = 2.0 ft, c = 0.5 ft), C_T = 0.004, C_P = 0.0003, θ_U / θ_L = 9°).

ies were performed to understand the change in power and thrust. A new approach will be discussed in the next chapter to understand the effect of BVI for coaxial rotors.

CHAPTER 4
BLADE CROSSING AND BVI LOCATION IDENTIFICATION

Compared to a single main rotor, a coaxial rotor system results in aerodynamic interactions between the upper and lower rotors. Two of these interactions include blade crossings and additional blade-vortex interaction (BVI) locations.

For a coaxial rotor, the time and location of a blade crossing occurrence is not always intuitive. As shown in Chapter 2, the occurrence of a blade crossing affects the overall aerodynamic loading on a blade. As a result, the change in loading on a blade directly affects a change in loading noise. Furthermore, the time and location of the blade-vortex interaction becomes more complex due to the additional rotor blades, and therefore more difficult to predict.

A computational tool was developed to predict the time and location of blade crossings and the time, location, and interaction angle of a BVI occurrence. By knowing information regarding blade overlap and BVI instances, further insights are given to understand coaxial aerodynamic and acoustic sources.

4.0.1 Blade crossing location identification

Unlike a 2D simulation, the exact time of blade overlap of two contra-rotating rotors, with more than one blade each, requires careful accounting. Therefore, the code RABBIT (RApid Blade and Blade-vortex Interaction Timer) was developed to predict the time and location of blade overlap. RABBIT is a MATLAB [65] code that identifies the time and azimuth at which a reference blade of the upper (or lower) rotor crosses a lower (or upper) rotor blade. RABBIT aids in pinpointing locations of interest between or in the plane of the rotors.

The upper and lower rotors can have different parameters in RABBIT including: RPM,

number of blades, blade phase, reference blade, radius, and chord. Though a constant RPM and blade phasing were used for the upper and lower Harrington [13] coaxial rotor as discussed in Chapter 1, results become less intuitive when the parameters for each rotor differ. For example, the reference blade is identified by first selecting the upper or lower rotor and then selecting the blade from that rotor. A blade crossing is recorded when a reference blade overlaps a blade from the other rotor. Figure 4.1 is an isometric view of the modern design coaxial rotor at V_{tip} = 625 ft/s, μ = 0.10, and S = 2.0 ft, α_s = 7.00°. For the modern design coaxial rotor with three blades per rotor (rotating in opposite directions), RABBIT captures six overlaps of the reference blade in one rotor revolution.

As shown in Fig. 4.1, the starting location for each blade is as follows: U_{ref} (upper rotor reference blade one, $U1$) is at 180°, $U2$ (upper rotor blade two) is at 60°, $U3$ (upper rotor blade three) is at 300°, $L1$ (lower rotor blade one) is at 240°, $L2$ (lower rotor blade two) is at 0°, and $L3$ (lower rotor blade three) is at 120°. The lower rotor blades overlap with U_{ref} in the following order for one revolution : $L3$ at 150°, $L2$ at 90°, $L1$ at 30°, $L3$ at 330°, $L2$ at 270°, and $L1$ at 210°.

For various unconventional coaxial configurations, RABBIT can predict blade crossings after one full revolution as shown in Fig. 4.2. One full revolution is defined by the time for the lowest RPM of the two rotors. Figure 4.2 a) shows an example of different spacing phase angles and two different radii and chord lengths for the upper and lower rotor. A coaxial rotor with varying RPM between the two rotors is calculated in Fig. 4.2 b). A complex combination of Fig. 4.2 a) and b) is shown in c), where the number of blades, RPM, radius, chord, and phase angle are different between the upper and lower rotor. These unconventional coaxial configurations are for educational purposes and were designed to help debug RABBIT.

The time and location of blade crossing will directly affect the acoustic signature. As shown in Chapter 2, the unsteady loading on the blade changes before, at, and after a blade crossing. The overall acoustic change will be discussed in Chapter 5 by comparing a single

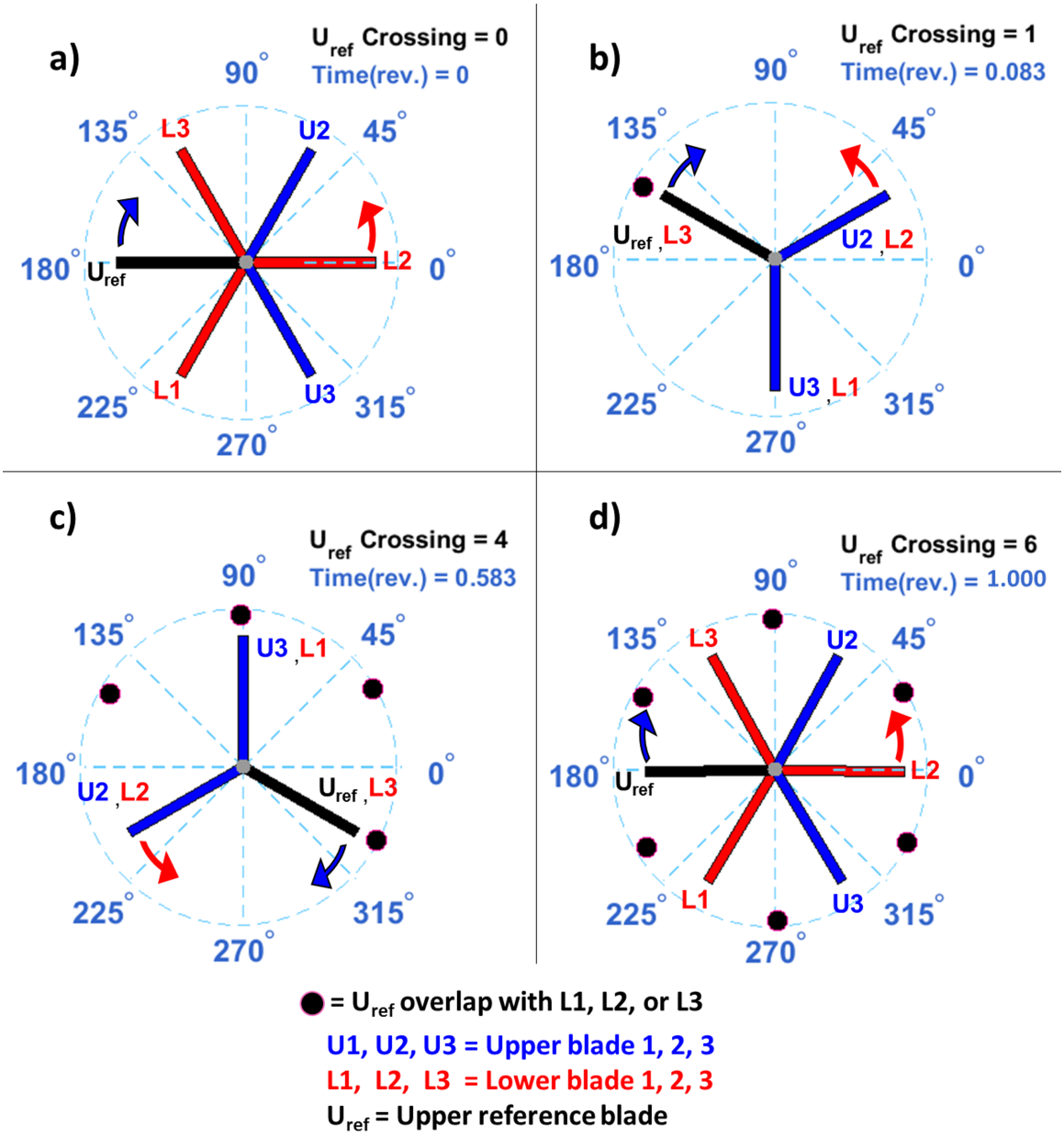

Figure 4.1: RABBIT's predictions for a six-bladed coaxial rotor blade crossing time and locations (V_{tip} = 625 ft/s, μ = 0.10, and S = 2.0 ft, α_s = 7.00°).

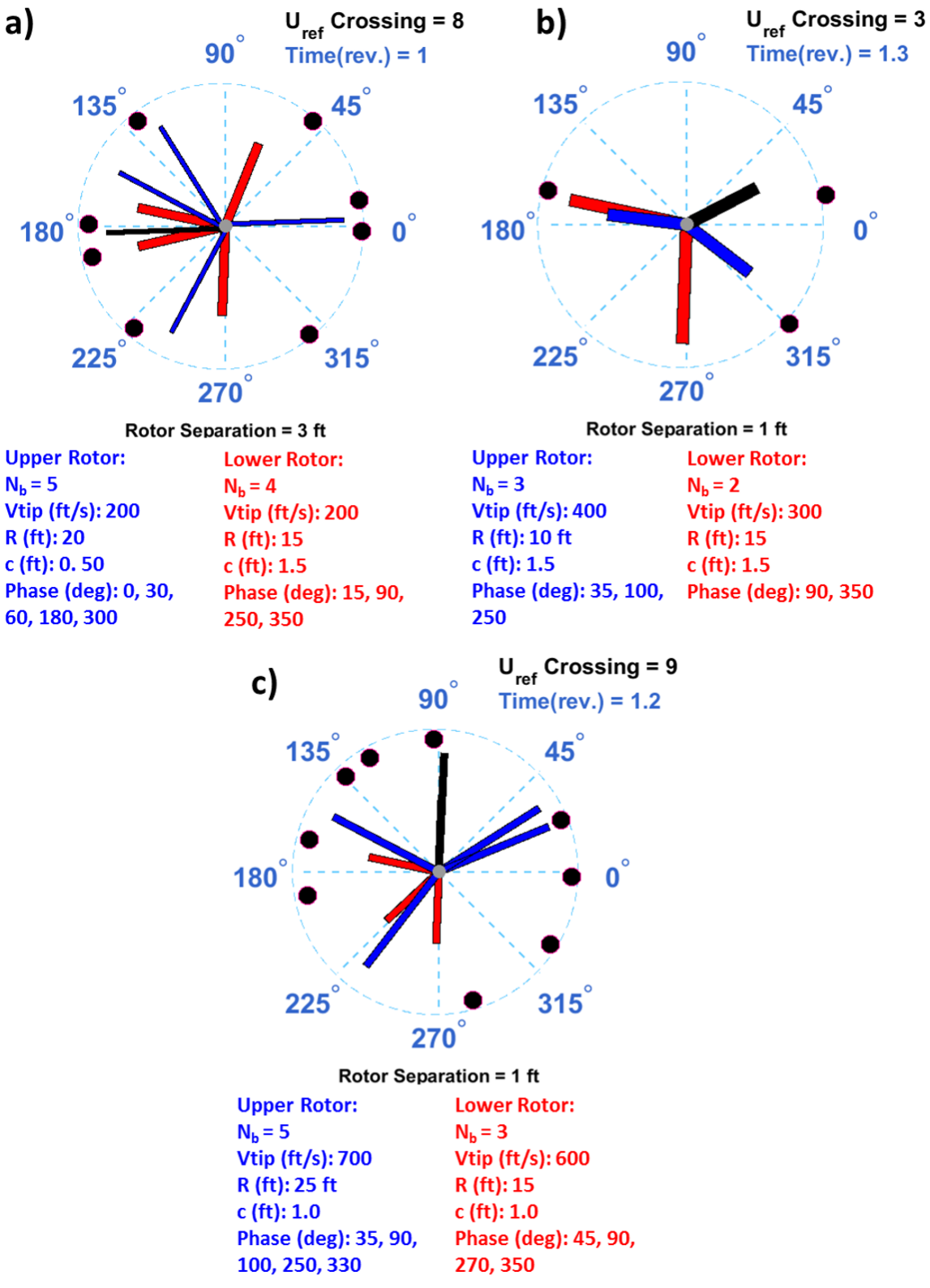

Figure 4.2: RABBIT's blade crossing predictions for three unconventional coaxial configurations.

and coaxial rotor in hover.

4.0.2 BVI location identification

For a finite wing, a tip vortex is generated due to difference in pressure between the upper and lower surface of the wing. The flow from the upper surface (low pressure) flows inboard toward the root, while the lower surface (high pressure) air flows toward the tip. A roll up is caused by the joining of the upper and lower surface at the trailing edge. A number of small vortices are formed along the span of the wing and are rolled up into two large vortices at the wings tips [59]. Due to the conservation of vorticity, the bound circulation is trailed into the wake from the blade (root to tip) [54].

For a rotor blade, the circulation and lift are often highest at the tip, whereas the velocity on the blade is highest. The trailed vorticity from the rotor blade tip is generated by the radial variation of the bound circulation. A pictorial explanation of the generation of the tip vortex for a single rotor blade is shown in Fig. 4.3 [54].

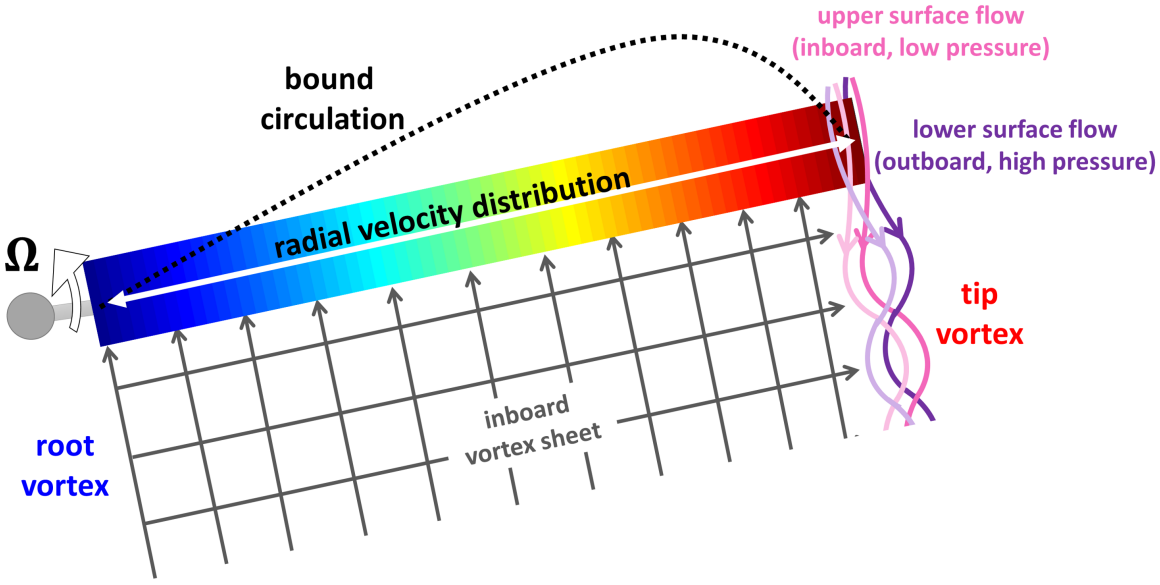

Figure 4.3: Pictorial representation of a blade tip vortex formation and the trailed and shed vorticity in wake.

The strength of the blade tip vortices is governed by tip vortex core size (blade tip

geometry) and bound circulation. The trajectory of the blade-vortex gives the opportunity for a possible vortex and blade collision, resulting in unsteady loading. The interaction between a tip vortex and a rotor blade is known as a blade-vortex interaction [54]. The effect of a direct interaction between a blade and tip vortices causes significant changes in blade loading and therefore noise. A vortex passing close to a rotor blade can also create a large change in loading. The strength of each interaction depends on the tip vortex strength, the local interaction angle between the blade and vortex, and the vertical distance between the blade and vortex [55]. For coaxial rotors, the lower rotor blades and the tip vortex from the upper rotor blades can create possible interactions [3].

The tool RABBIT, as previously mentioned, not only identifies the time and location of a blade crossing, but also the time, location, and angle of a BVI. The tip vortex trajectory model in RABBIT uses Beddoes prescribed wake [64]. The RABBIT's BVI identifier was validated using a single rotor blade study performed by Sim, George, and Yen [66]. Similar studies that identify BVI occurrences have been performed by others including Gandhi and Tauszig [67], where the wake was modeled as a free wake based on the Maryland Free Wake (MFW) algorithm. RABBIT was also validated for a coaxial rotor case using CAMRAD II.

4.0.3 Single rotor BVI location identification

Both RABBIT and Sim et al. [66] simulations incorporated Beddoes prescribed wake model that uses a correction to the rigid wake based on the vortex element location. The three locations are when the vortex element is (1) within the rotor disk, (2) between the rotor disk and wake and (3) in the rotor wake [66]. Beddoes's prescribed wake model is limited to advance ratios below 0.15 [66]. Table. 4.1 shows the operating conditions for the single rotor case study, by Sim et al., [66], that was used to validate RABBIT for a single rotor.

Predictions from the Sim et al., [66] rotor case study (Table. 4.1) were compared to

Table 4.1: Operating conditions for single rotor case study.

Variable	Value	Units
R, Radius	3.28	ft
c, chord	0.328	ft
No. of blades	1	n/a
α_s, shaft angle	2.862	deg
Airfoils	NACA 0012	n/a
V_{tip}, tip speed	656.18	ft/s
χ_{TPP}, Skew angle	73.72	deg
Forward Velocity	65.68	ft/s
μ, Advance ratio	0.1000	n/a
μ_z, Rotor axial velocity ratio	0.0050	n/a
C_T, Thrust coefficient	0.0050	n/a

RABBIT's predictions. In Fig. 4.4 the rotor tip vortex wake displacements for X, Y, and Z, nondimensionalized by the rotor radius, are shown. Figure 4.4 c) includes the Beddoes wake as calculated by [66], a free wake, rigid wake, and experimental data provided by [66]. The rigid wake model correlates least with experimental data, while the freewake and Beddoes wake (RABBIT and Sim et al.) correlate equally as well. Discrepancy between RABBIT and Sim et al., for Z/R could be due to the difference in vortex wake discretization. Sim et al., modeled the vortex wake every degree and RABBIT modeled the wake vortex every 1/5 degree.

Figure 4.5 shows the output from RABBIT after one rotor revolution and includes the location of blade-vortex interactions and the tip vortex trajectory. A comparison of the identified blade-vortex interaction locations between Sim et al., and RABBIT are shown in Figs. 4.6. As shown in Fig. 4.6, Sim et al., provides only BVI at r/R = 0.90. RABBIT's prediction for the blade azimuth angle versus r/R agree with Sim et al., results at r/R = 0.90, both analyses predicting five different BVIs at 30, 58, 81, 285, and 315 degrees.

The BVIs were calculated to determine the significance of each interaction for the case study. Important BVI strength factors include translating blade velocity (V_b), BVI angle (γ), miss distance (h), vortex strength (Γ), time (t), 2D lift curve slope (c_{l_α}), and chord (c). From this information Sim et al., calculated, a BVI impulse factor ($\overline{I}$) and the time rate of

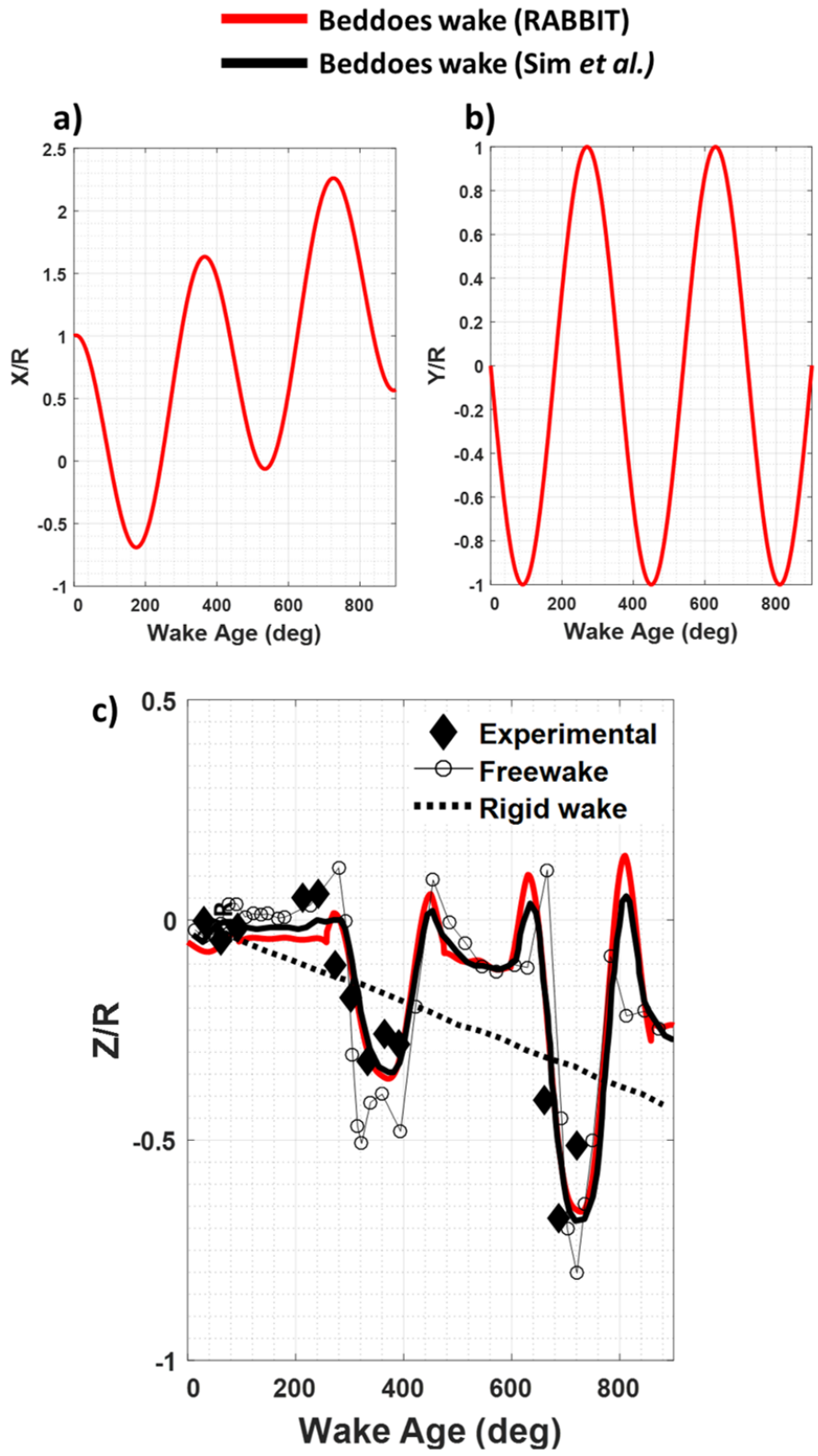

Figure 4.4: Rotor tip vortex wake displacement for a) X/R, b) Y/R, and c) Z/R.

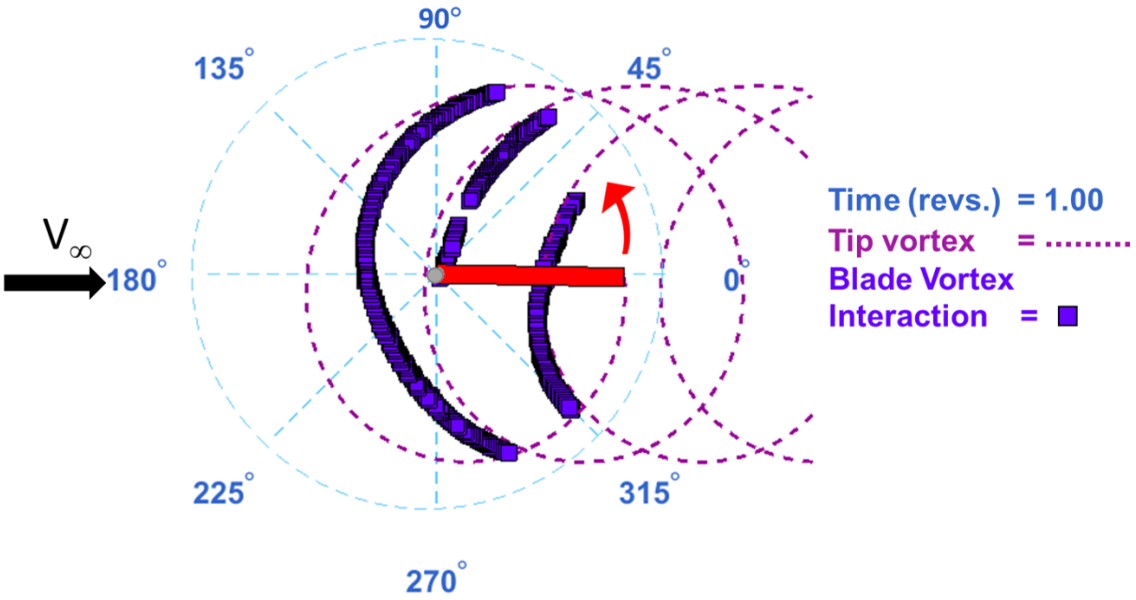

Figure 4.5: RABBIT output for single rotor case study.

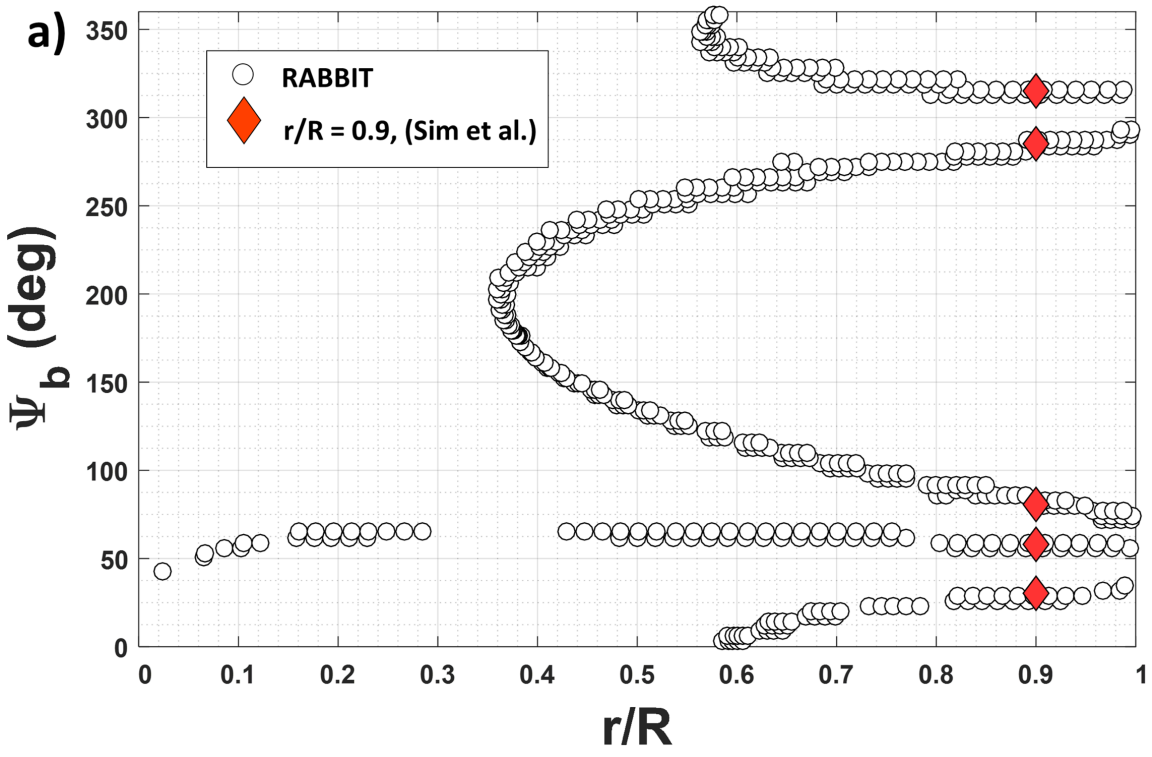

Figure 4.6: RABBIT and Sim et al., case study comparison of blade azimuth angle versus r/R locations.

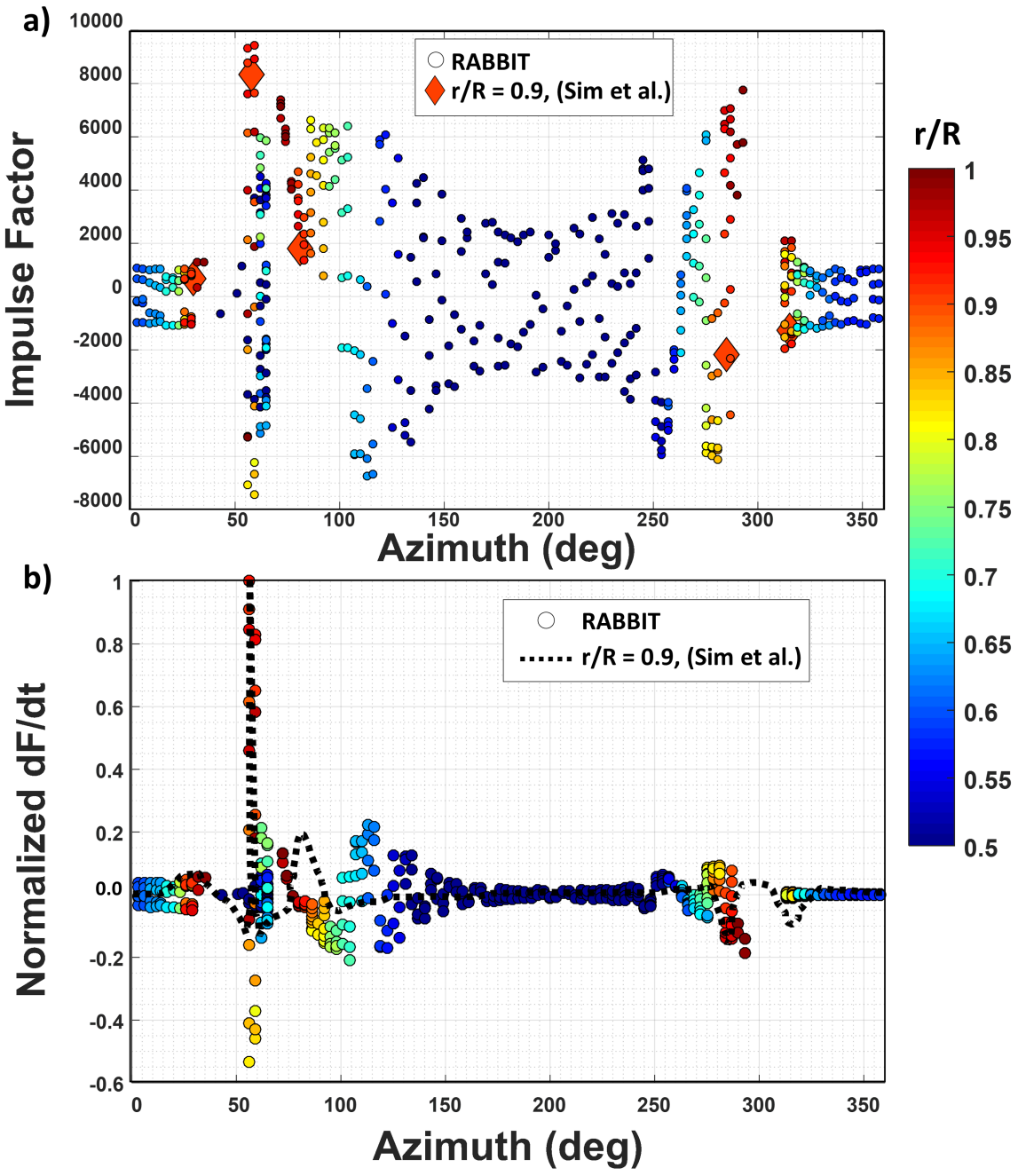

Figure 4.7: RABBIT and Sim et al., case study comparison of a) impulse factor versus azimuth angle and b) normalized $\frac{\partial F}{\partial t}$ versus azimuth angle for r/R locations.

change of loading ($\frac{\partial F}{\partial t}$). The vortex strength ($\Gamma$) is calculated by assuming a core size 5% of the chord [66]. The BVI impulse factor relates to the time rate of change of the bladess loading and is related to the magnitude of $\frac{\partial F}{\partial t}$ and noise intensity. Equations 4.2 through 4.4 are from Sim et al., [66].

The impulse factor is calculated from the translating blade velocity, BVI angle, and miss distance, see equation 4.1. The translating blade velocity is the velocity on the blade at the location of interaction, and determined by the radial and azimuthal position. The BVI angle is the angle at which the vortex hits the blade, and the miss distance is the vertical distance from the blade tip to the vortex. The product of the vortex strength factor ($\overline{\Gamma}$) and shape function ($\overline{X}$) are then used to calculate the time rate of change of loading ($\frac{\partial F}{\partial t}$), see equations 4.2 through 4.4 [66].

The impulse factor and $\frac{\partial F}{\partial t}$ normalized by maximum $\frac{\partial F}{\partial t}$ are calculated for the case study for all radial locations and shown in Figs. 4.7 a) and b), respectively. For both RABBIT and the Sim et al., calculations, the normalized $\frac{\partial F}{\partial t}$ resulted in the largest strength at 58 degrees. RABBIT was able to calculate similar values for BVI locations at 30, 58, and 285 degrees for r/R = 0.90 compared to Sim et al., but differed for BVI locations at 81 and 315 degrees. Differences between RABBIT and Sim et al., calculated impulse factor and normalized $\frac{\partial F}{\partial t}$ are due to differences seen in the Z/R wake (Fig. 4.4 c)) and vortex wake modeling, which directly influences the values of BVI angle and miss distance.

$$\overline{I} = \frac{V_b \cos\gamma}{h}, \tag{4.1}$$

$$\overline{\Gamma} = \frac{\Gamma}{2\pi h V_b} \tag{4.2}$$

$$\frac{\partial F}{\partial t} = (c_{l_\alpha} c)(\frac{1}{2}\rho V_b^2)(\overline{\Gamma})(\overline{I})\frac{1-\overline{X}^2}{(1+\overline{X}^2)^2} \tag{4.3}$$

$$where, \overline{X} = \frac{V_b \cos(\gamma)}{h} t \tag{4.4}$$

4.0.4 Coaxial rotor blade crossing and BVI location identification

RABBIT was validated against CAMRAD II [61] for a coaxial rotor by comparing an upper rotor tip vortex wake from each analysis and comparing BVI locations and times with the lower rotor blades. RABBIT's Beddoes wake model does not account for rotor-rotor wake interaction. CAMRAD II uses a non-uniform inflow free wake geometry different from the Beddoes wake model, that accounts for rotor-rotor wake interaction. Only the upper tip vortex for the reference blade was modeled for simplicity.

A descent flight condition (V_{tip} = 625 ft/s, μ = 0.0867, C_T = 0.0025, and α_S = 10.00°) for the modern design coaxial rotor was chosen to ensure a BVI location at the lower rotor. Figure 4.8 shows RABBIT's calculated blade crossing time and predicted BVI lower rotor location for upper reference blade one (U_{ref}) after one revolution.

RABBIT's capability to identify the location and time of a blade overlap was first validated against CAMRAD II. RABBIT and CAMRAD II predicted three distinct upper reference blade BVI instances with the lower rotor. Next, RABBIT's wake was compared to the wake from CAMRAD II for the same descent flight case. The wakes from each simulation are compared by overlaying the wakes and identifying possible BVIs. The two wakes are compared in Fig. 4.9 at a time of 0.786 revolutions, where a BVI occurrence is identified at the lower rotor blade one with U_{ref}. The trajectory of the CAMRAD II tip vortex for the reference blade is compared to the RABBITs tip vortex for the same reference blade for each instance in time of a BVI occurrence, as shown in Fig. 4.10. Though the wake from RABBIT and CAMRAD II are different in shape, the location and time of all BVI occurrences are the same. BVI location predictions for both RABBIT and CAMRAD II are at 91, 250, and 276 degrees and all locations are at a span location greater than r/R of 0.85. Due to the different shape of the wakes, values of BVI angle and miss distance

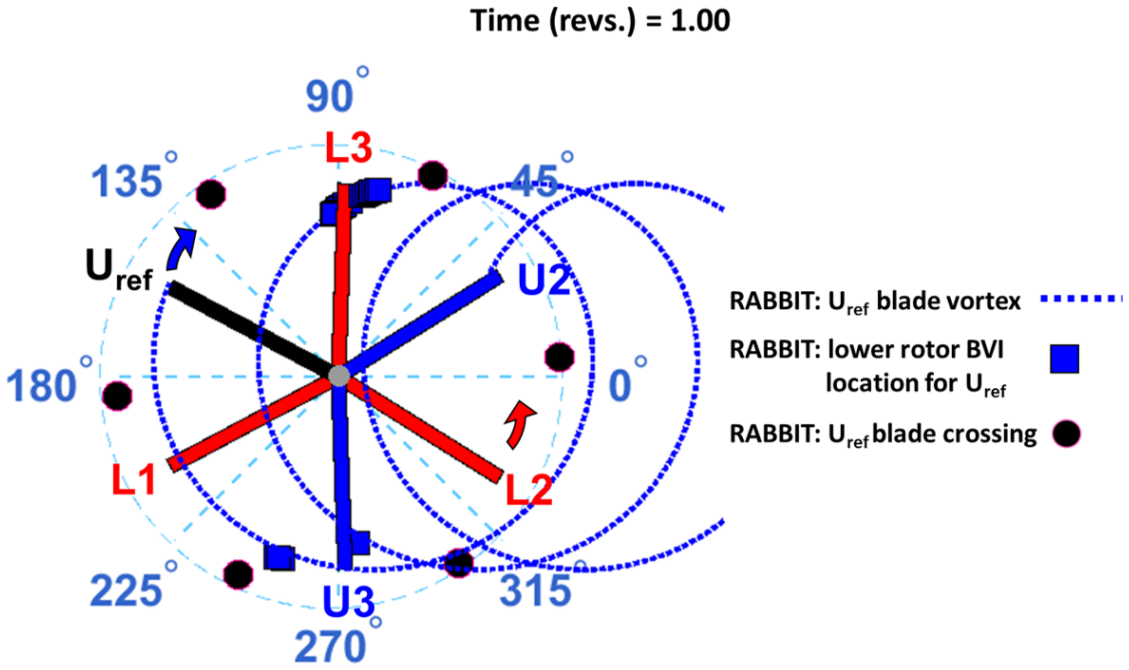

Figure 4.8: RABBIT blade crossing and lower rotor BVI predictions for a six-bladed (three upper/ three lower) coaxial rotor (V_{tip} = 625 ft/s, μ = 0.0867, and S = 2.0 ft, χ_{TPP} = 89.6°, C_T = 0.0025, α_S = 10.00°).

are expected to vary slightly between RABBIT and CAMRAD II. The BVIs at 91 degrees are strongest, in terms of impulse factor and normalized $\frac{\partial F}{\partial t}$, compared to BVIs at 250 and 276 degrees, as shown in Fig. 4.11. The BVI at 91 degrees is the strongest because the interaction location is on the advancing side of the lower rotor and so the translating blade velocity is large compared to the BVI locations of 250 and 276 degrees.

4.0.5 SUMMARY

The computational tool RABBIT was developed to predict the time and location of blade crossings and the time, location, and interaction angle of BVIs. RABBIT's capabilities are validated using the Sim et al., case study for a single rotor with one blade. The BVI location and strength were correctly predicted for the strongest BVI occurrence. CAMRAD II was used to validate RABBIT's blade crossing and BVI location, time, and angle for a modern coaxial rotor.

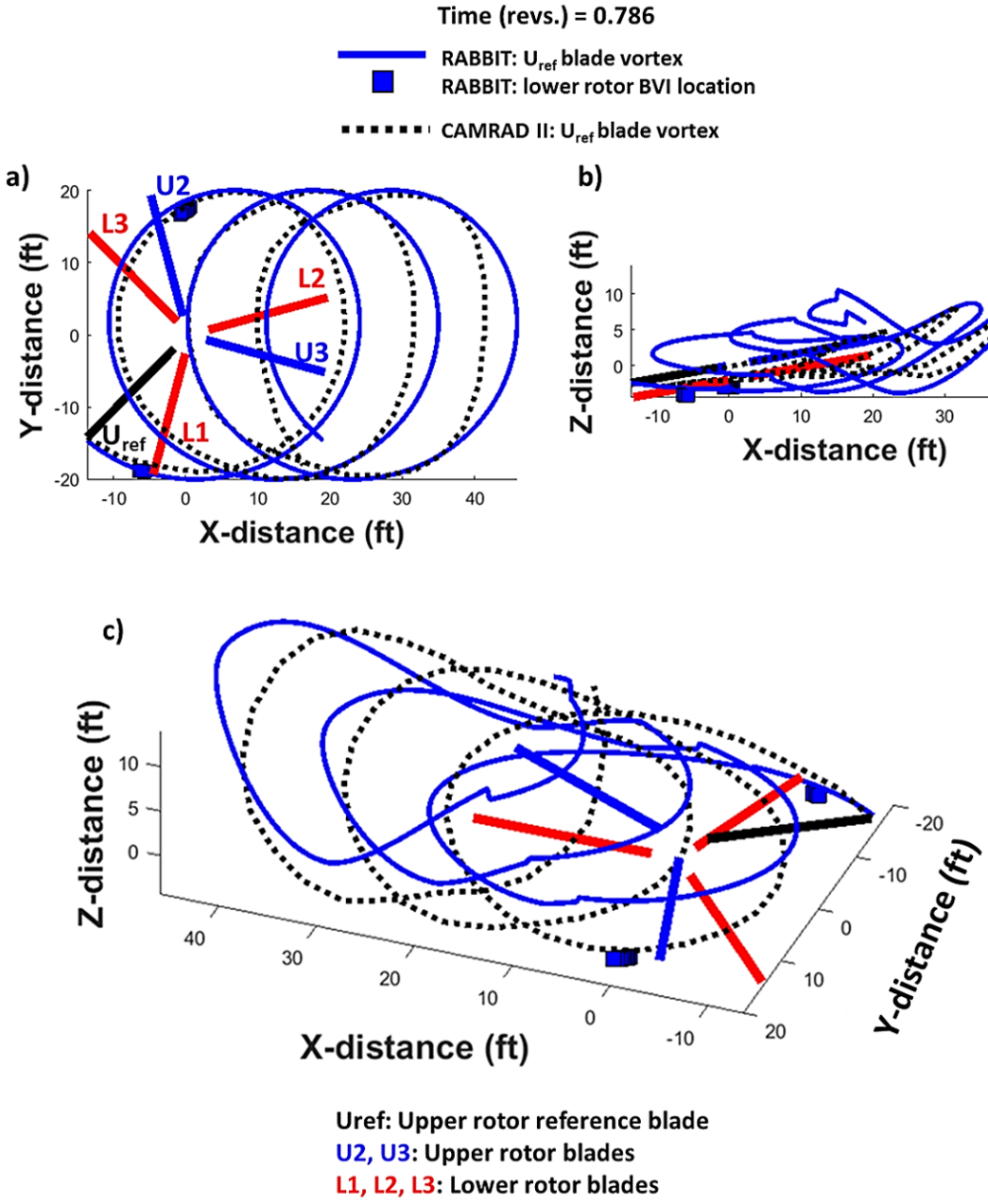

Figure 4.9: RABBIT versus CAMRAD II predictions for a six-bladed coaxial (three upper/ three lower) rotor wake comparison at time of 0.786 rev. (U_{ref}) (V_{tip} = 625 ft/s, μ = 0.0867, and S = 2.0 ft, χ_{TPP} = 89.6°, C_T = 0.0025, α_S = 10.00°).

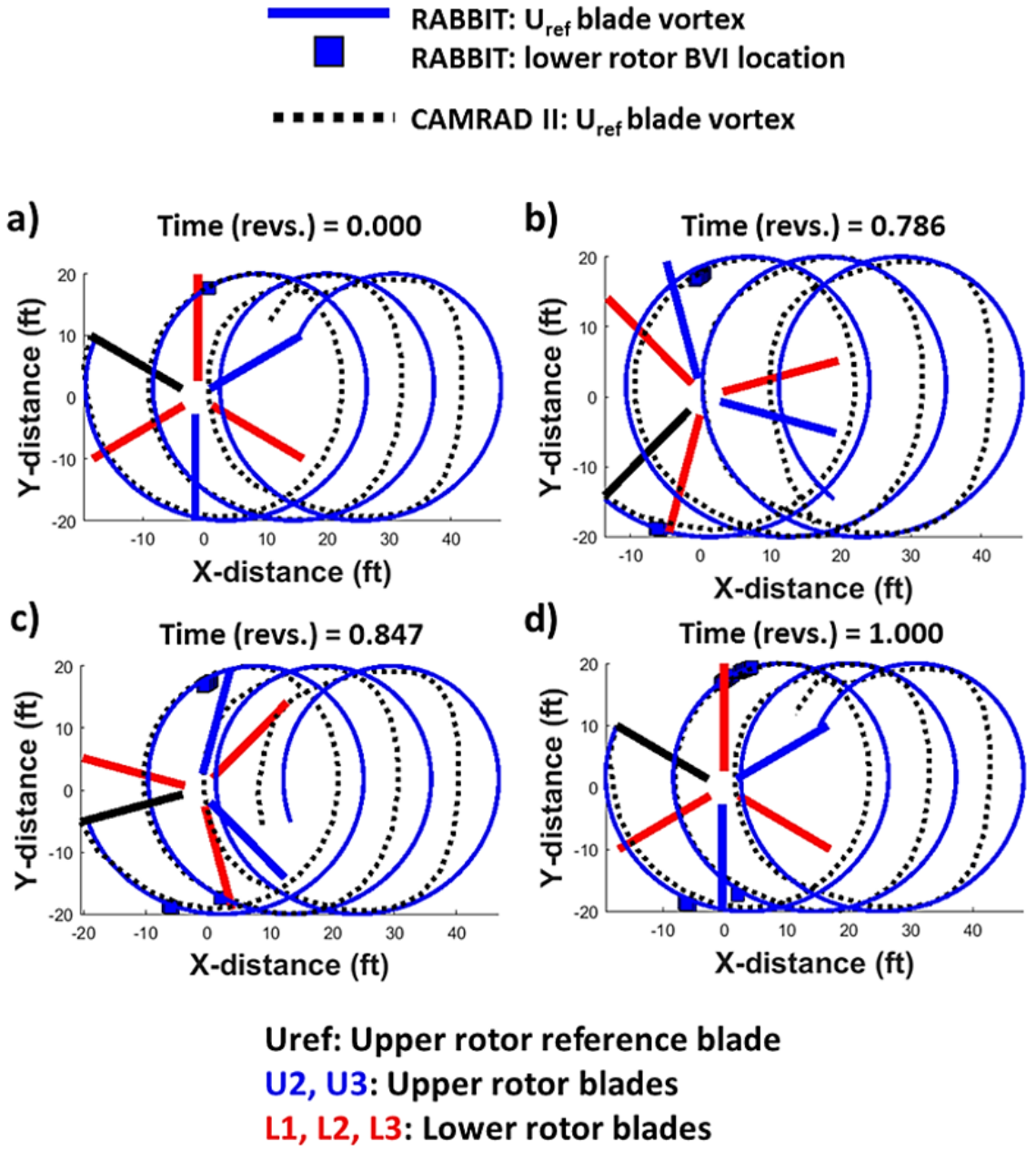

Figure 4.10: RABBIT versus CAMRAD II predictions for a six-bladed coaxial (three upper/ three lower) rotor blade crossing time and BVI lower rotor locations for U_{ref} at time of a) 0.000, b) 0.786, c) 0.847, and d) 1.000 revs. (V_{tip} = 625 ft/s, μ = 0.0867, and S = 2.0 ft, χ_{TPP} = 89.6°, C_T = 0.0025, α_S = 10.00°).

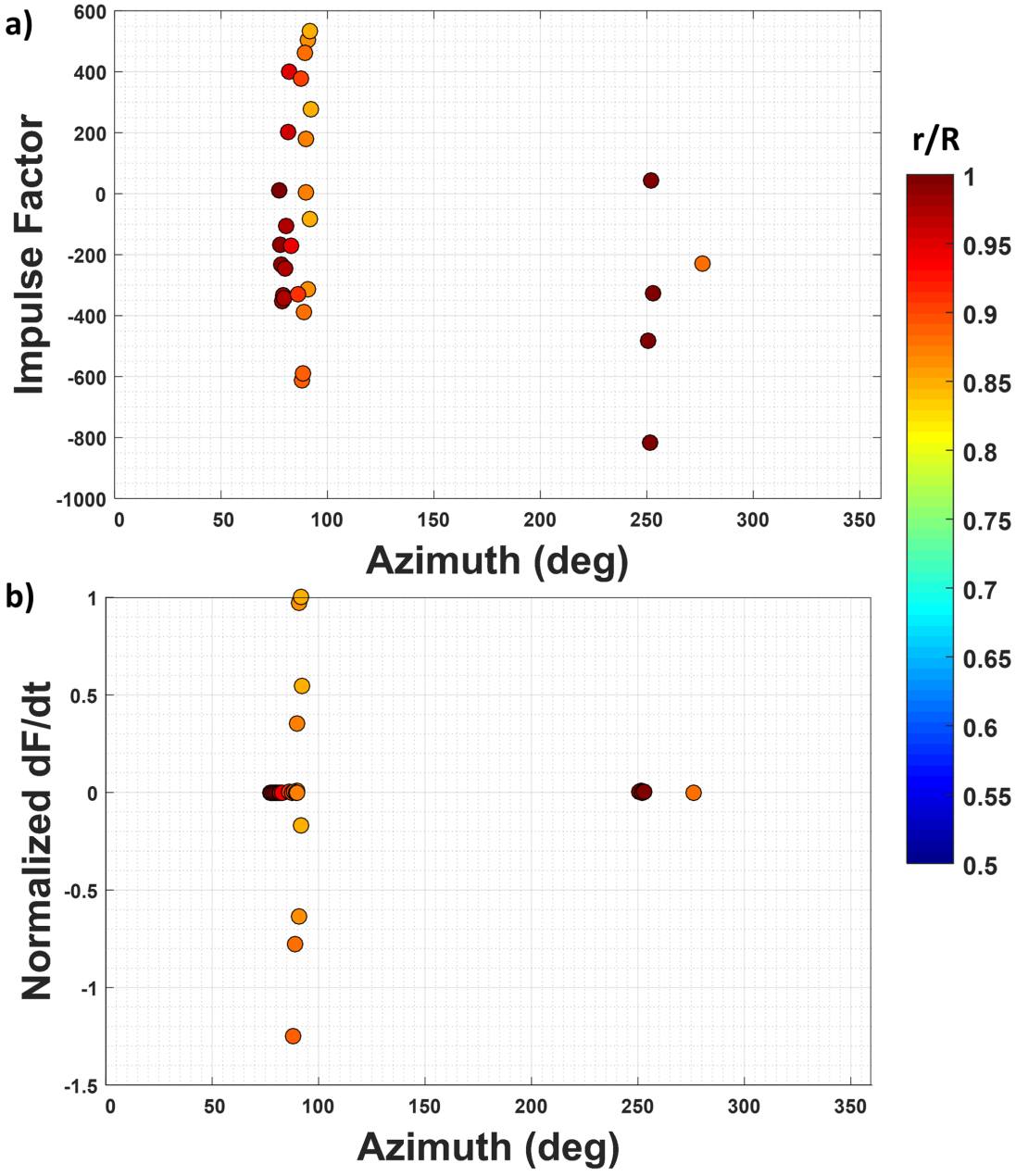

Figure 4.11: RABBIT modern coaxial lower rotor BVI predictions for U_{ref} for a) impulse factor and b) normalized $\frac{\partial F}{\partial t}$ versus azimuth angle for r/R locations (V_{tip} = 625 ft/s, μ = 0.0867, and S = 2.0 ft, χ_{TPP} = 89.6°, C_T = 0.0025, α_S = 10.00°).

CHAPTER 5

ACOUSTIC PREDICTION: THICKNESS AND LOADING NOISE

The aerodynamics of a helicopter directly effect the aeroacoustics, but lack information regarding time and radiation direction. Loads on a coaxial and single rotor in hover, along with thickness effects were computed to study the time-varying acoustic pressure signature. The coaxial and single rotor acoustic signatures were compared for various observer locations to understand acoustic response differences.

The 2D loads computed in Chapter 2 were stacked to represent the spanwise loading of a rotor blade. A tip loss factor was introduced to account for zero loading at the tip of a 3D blade. The spanwise loading was then used as input to an acoustics solver to compute the noise at specified observer locations. Both thickness and loading noise were computed.

5.1 Aerodynamics loads

OVERFLOW 2D results as shown in Chapter 2 (Fig. 2.38), were stacked together to represent the modern single rotor design in hover. A blade loading tip loss factor was applied to the loads for the single rotor and modern rotor design. Due to three-dimensional flow effects, actual blade loading is zero at the tip [68]. The difference between blade element theory and actual loading on a rotor blade is shown in Fig. 5.1. Prandtl's tip loss factor is directly applied to the calculated loads for each radial station as shown in equation 5.1.

$$F(r/R) = \frac{2}{\pi} cos^{-1}\left(exp\left(-\frac{N_b}{2}\frac{\sqrt{1+\lambda^2}}{\lambda}(1-r/R)\right)\right), \quad (5.1)$$

Figure 5.2 shows the aerodynamic loading for the single modern rotor design a), b), and c) without tip loss and d), e), and f) with a tip loss factor. The total loss of lift from

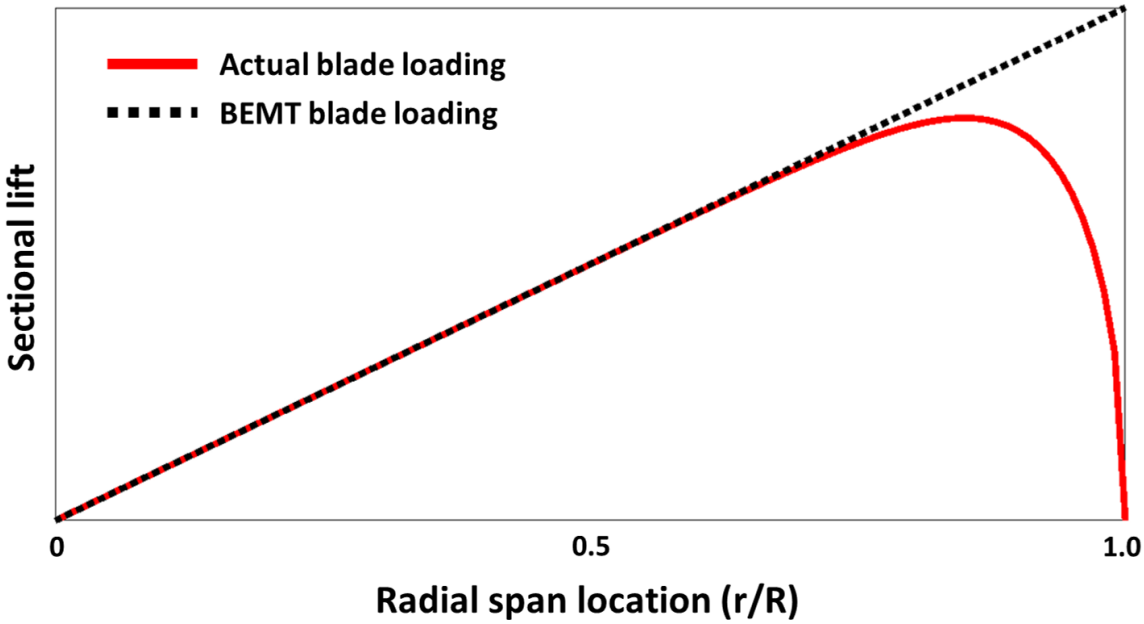

Figure 5.1: Rotor blade loading with and without tip loss.

applying a tip loss factor must be added back to the total lift, so overall lift remains the same [54]. The total lift difference with and without tip loss factor for the modern single rotor hover case is less than 0.50 $\%$ in total F_Z. OVERFLOW 2D results for the modern coaxial rotor as shown in Chapter 2 (Fig. 2.39) are also stacked with an applied tip loss factor to the lift, see Fig. 5.3. The main difference between the single and coaxial modern rotor loading distribution is the presence of pulses, due to blade overlap, for the coaxial modern rotor design. The increase and decrease in lift due to blade crossing can be seen at 45, 105, 165, 225, 285, and 345 degrees, which was predicted by RABBIT (Fig. 4.1).

5.2 Acoustic predictions: thickness and loading noise

The noise from the single and coaxial modern rotors were predicted using PSU-WOPWOP version 3.4.3 [69, 51]. The loads from the stacked OVERFLOW results as shown in Figs. 5.2 and 5.3, were used in the PSU-WOPWOP calculations to compute loading noise. Observers were placed around the rotor to understand differences in loading and thickness noise between a single and coaxial modern rotor. Differences in the acoustic pressure time

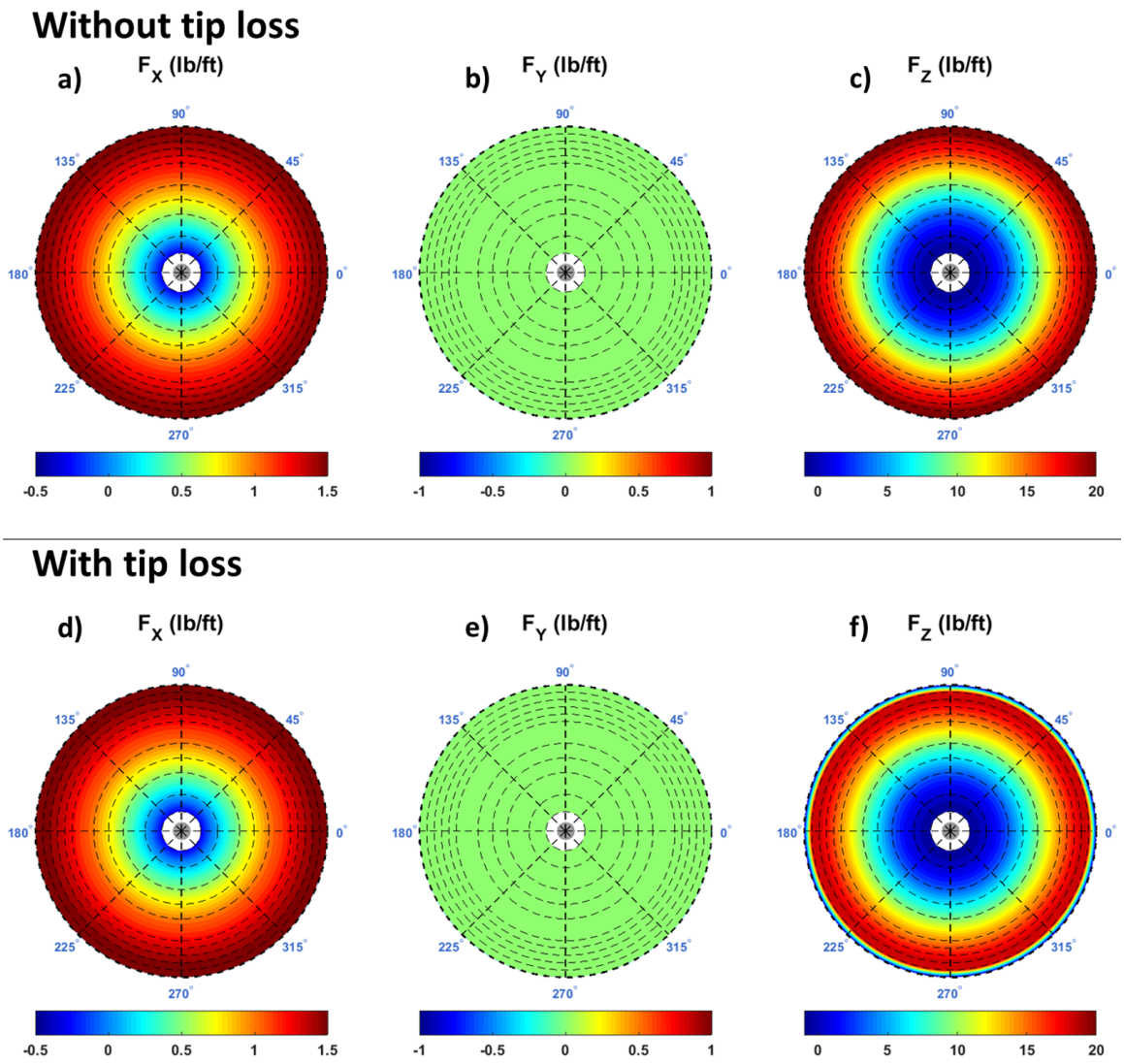

Figure 5.2: Stacked 2D OVERFLOW results for modern single modern rotor in hover without tip loss factor a) F_X, b) F_Y and c) F_Z, and with tip loss factor d) F_X, e) F_Y and f) F_Z.

history and overall sound pressure level (OASPL) are discussed.

5.2.1 PSU-WOPWOP version 3.4.3

PSU-WOPWOP [69, 51] is a rotor noise prediction code that numerically solves Farassat's Formulation 1A of the Ffowcs Williams-Hawkings equation (see equations 1.4 through 1.6 from Chapter 1). Information regarding the rotor blade motion, blade surface geometry, and

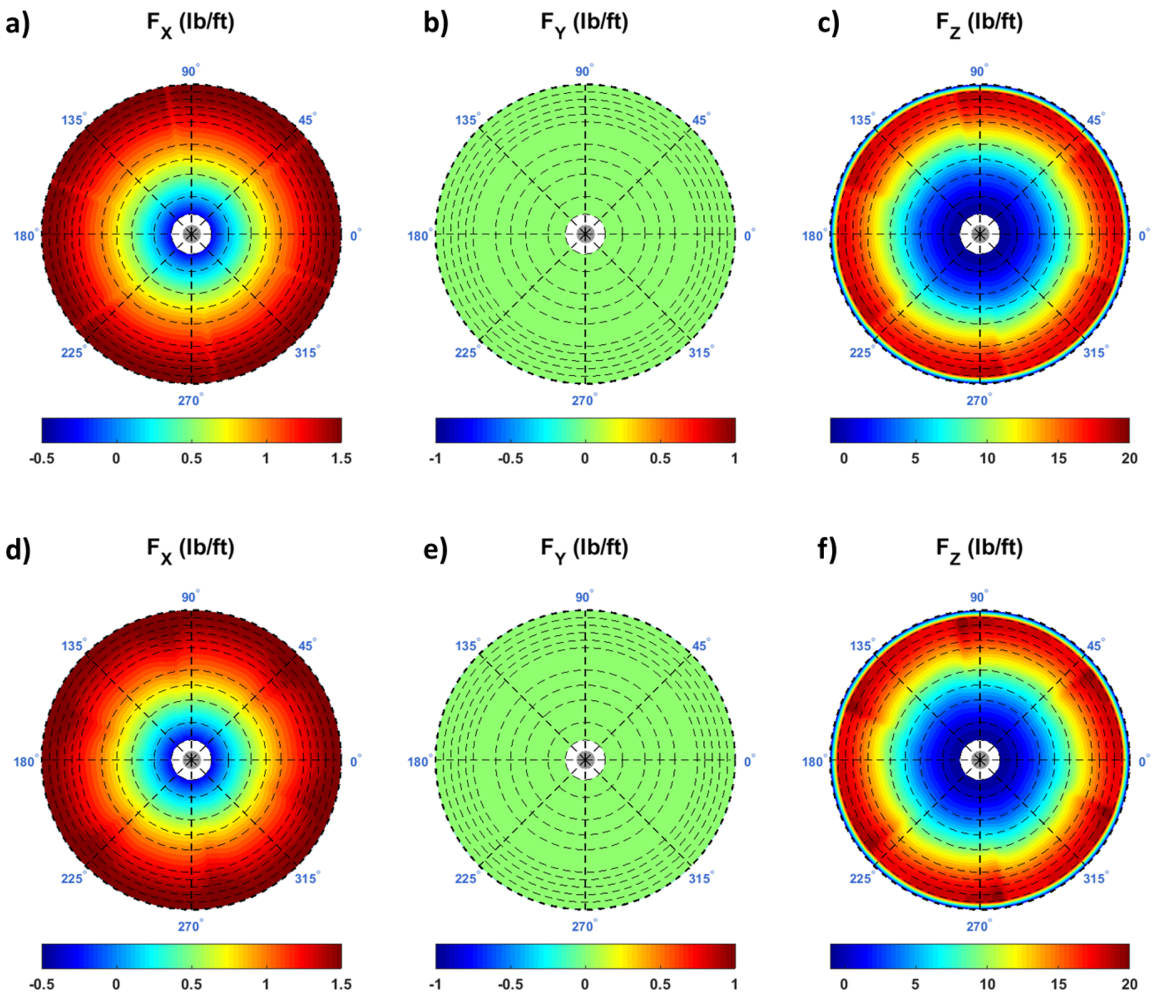

Figure 5.3: Stacked 2D OVERFLOW results for modern coaxial modern rotor in hover upper rotor a) F_X, b) F_Y and c) F_Z and lower rotor d) F_X, e) F_Y and f) F_Z.

loading are needed to compute the acoustic pressure time history, along with the observer location. PSU-WOPWOP version 3.4.3 was used for all acoustic predictions in this thesis.

5.2.2 Observer locations

Multiple observers were placed around the single and coaxial modern rotor, where the origin was at the center of the hub for the single modern rotor and at the midpoint between the two rotors for the coaxial modern rotor. Observers were placed three rotor radii away at elevation angles of 15, 0, -15, -45, and -90 degrees and azimuthally of 90, 45, 0, -45 and

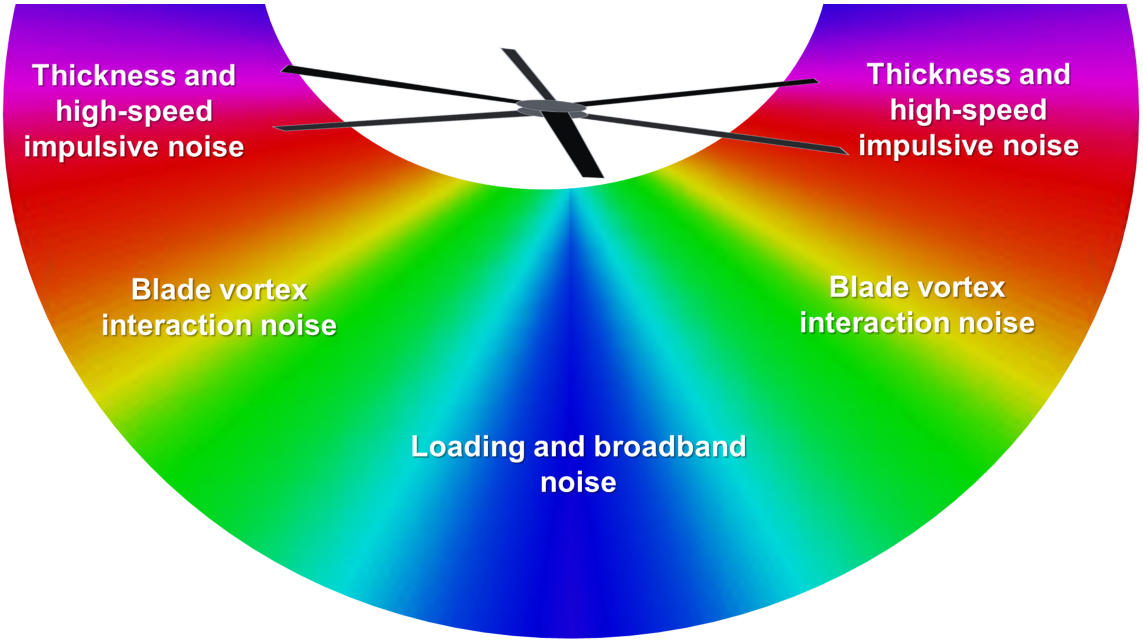

Figure 5.4: Rotor source noise directivity.

-90 degrees (Table 5.1). Observers placed in-plane or near in-plane of the rotor are intended to capture thickness effects, while observers below are intended to capture the dominating loading noise. Observers 2 and 8 are directly in-plane of the rotor where thickness noise dominates, while observer 5 is directly below the rotor where loading noise dominates. General thickness and loading noise directivity is illustrated in Fig. 5.4.

Table 5.1: Single and coaxial modern rotor observer locations.

Observer #	X/R	Y/R	Z/R	Distance (Radii)	Directivity (deg)	Perspective
1	2.90	0.00	0.75	3.00	15	elevation
2	3.00	0.00	0.00	3.00	0	elevation
3	2.90	0.00	-0.75	3.00	-15	elevation
4	2.12	0.00	-2.12	3.00	-45	elevation
5	0.00	0.00	-3.00	3.00	-90	elevation
6	0.00	3.00	0.00	3.00	90	azimuth
7	2.12	2.12	0.00	3.00	45	azimuth
8	3.00	0.00	0.00	3.00	0	azimuth
9	2.12	-2.12	0.00	3.00	-45	azimuth
10	0.00	-3.00	0.00	3.00	-90	azimuth

Loading (lift) noise dominates in the plane of the lift for the rotors, because of this

loading noise will be highest directly above and below the rotor due to the lifting force vector pointing in the direction of the observer location. Thickness (form drag) noise is highest in front of the rotor due to the motion of the blade, which is in the same plane as the drag force.

5.2.3 Single modern rotor acoustic predictions

For the single modern rotor in hover, acoustic time history and frequency spectrum for the elevation observers (observers 1 through 5) are shown in Figs. 5.5 and 5.6, respectively. Acoustic pressure time histories and frequency spectra for the azimuthal observers (observers 6 through 10) are shown in Figs. 5.7 and 5.8, respectively.

Observers 1 through 5, at elevation angles 15 to -90 degrees, show thickness noise in front of the rotor between an elevation angles of 15 to -15 degrees (Figs. 5.5 a), b), and c) and Figs. 5.6 a), b), and c)). Note that the scale for thickness noise in Figs. 5.5 and 5.6 are much smaller than the scale for loading noise. The three pulses seen in the thickness noise are due to the three blades. In Figs. 5.7 and 5.8, the observers 6 though 10 are placed in the plane of rotor from 90 to -90 degrees. Thickness noise overall sound pressure level (76.7 dB) is the same at observers 6 through 10, but the location of the blade pulses are shifted due to the different arrival times. Loading noise is highest when the observer is directly below the rotor (an elevation of -90 degrees, Figs. 5.5 e) and 5.6 e).

5.2.4 Coaxial modern rotor acoustic predictions

Acoustic pressure time histories and frequency spectra predictions for the coaxial modern rotor in hover are shown in Figs. 5.9 and 5.10, respectively, for observers 1 through 5 for elevation angles of 15, 0, -15 , -45, and -90 degrees, respectively. Figures. 5.11 and 5.12 show corresponding results for observers 6 through 10 for azimuthal angles of 90, 45, 0 , -45, and -90 degrees, respectively.

Figure 5.9 shows thickness noise in front of the rotor from an elevation angle from

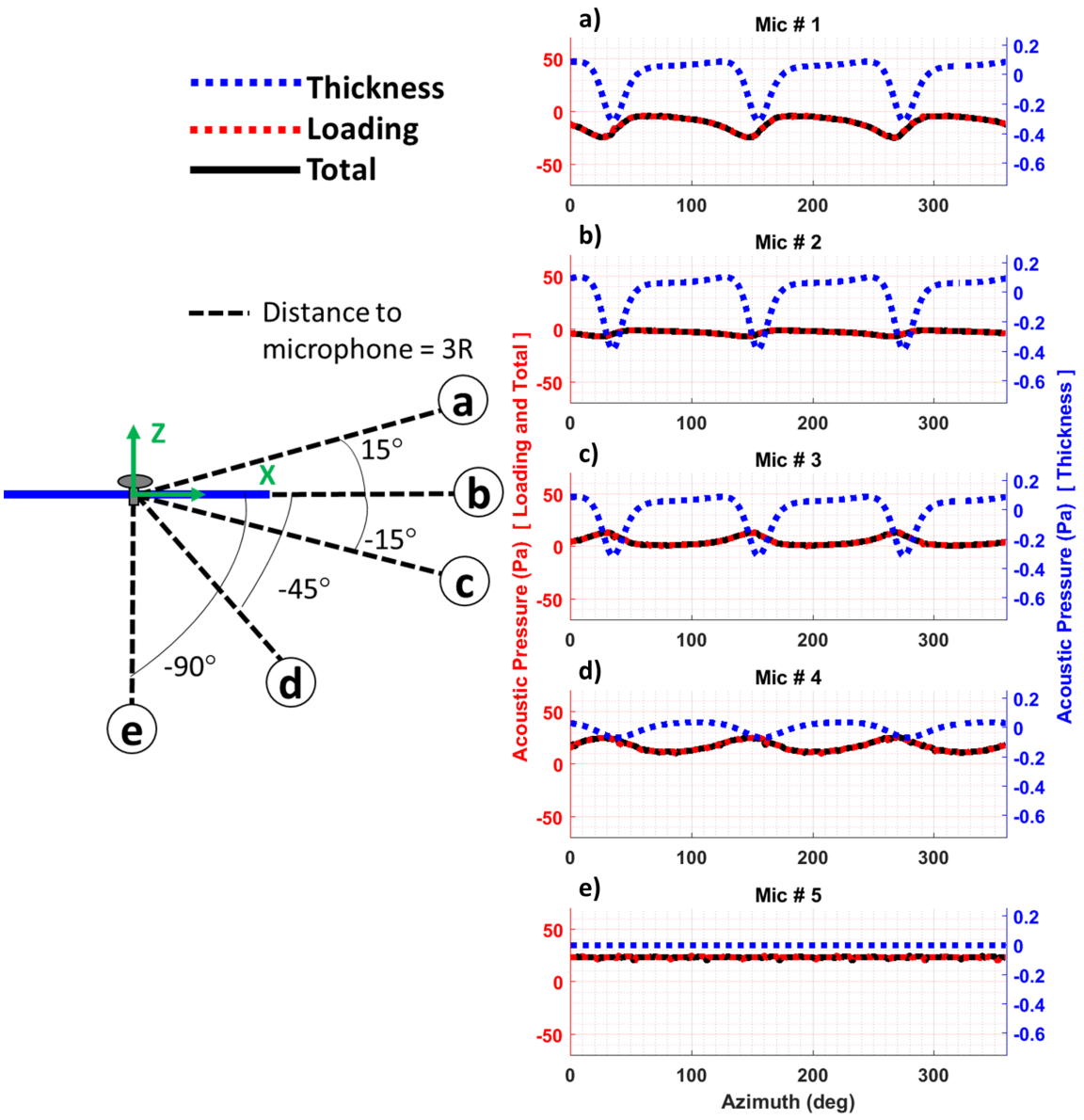

Figure 5.5: Elevation acoustic directivity in hover for single modern rotor acoustic pressure time history. The left (red) y-axis corresponds to loading and total noise, and the right (blue) y-axis corresponds to thickness noise.

15 to -15 degrees. Only three pulses are seen in Figs. 5.9 a) through b) due to the phase of the blades and observer location; in this case the noise from an upper and lower rotor blade arrive at observers 1 through 3 at the same time. For in-plane observers 6 though 10, Fig. 5.11 a) shows six distinct pulses can be seen in the thickness noise prediction, whereas in Fig. 5.11 c) only three pulses can be seen due to the phase of the blades and observer

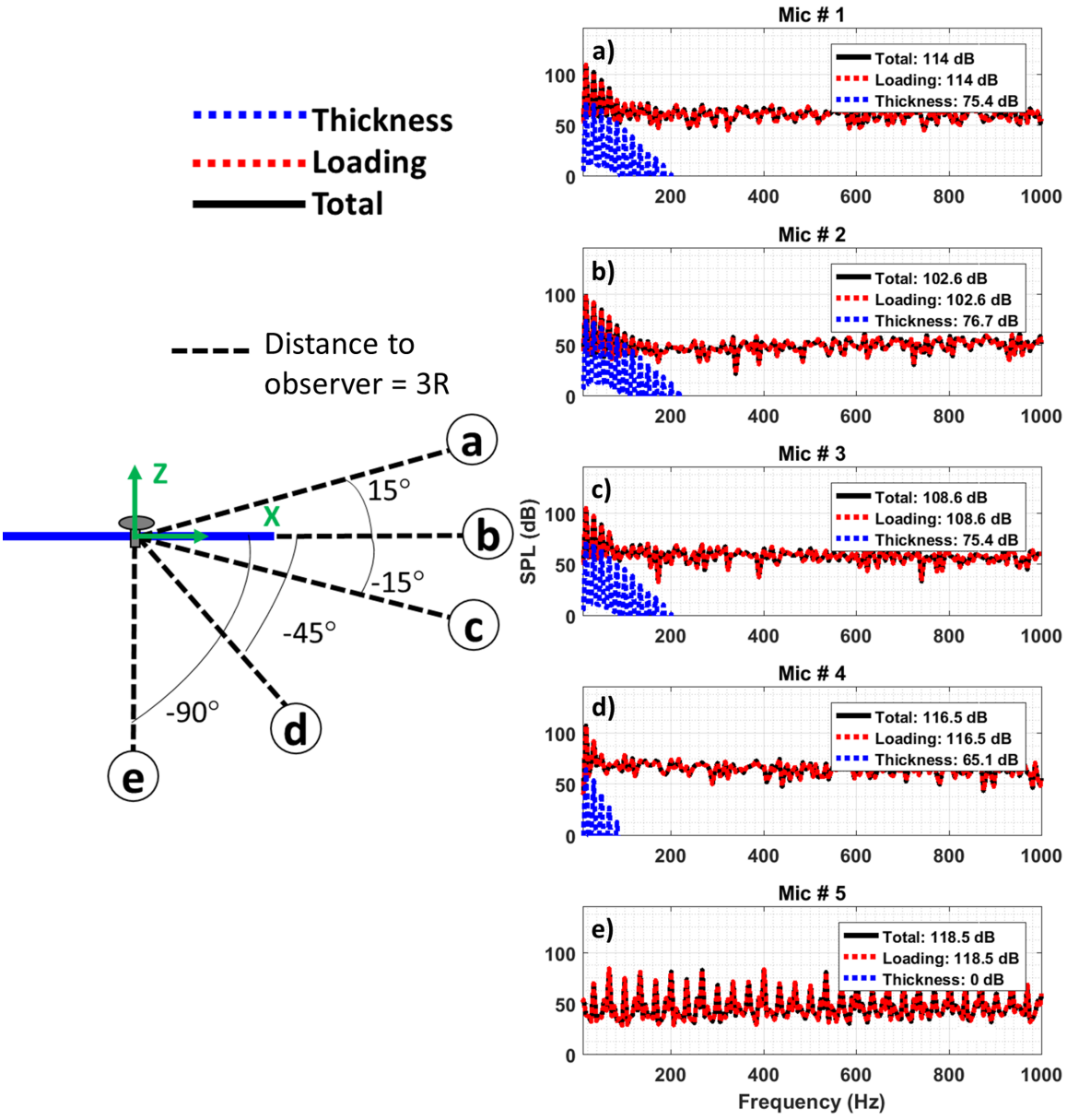

Figure 5.6: Elevation acoustic directivity in hover for single modern rotor frequency spectrum.

location.

Loading noise for the coaxial modern rotor loading is largest directly below the rotor (Figs. 5.9 e) and 5.10 e)), similar to the single rotor. The effect on loading noise due to blade overlap can be seen in Fig. 5.9 e), where six large pulses are seen at 45, 105, 165, 225, 285, and 345 degrees.

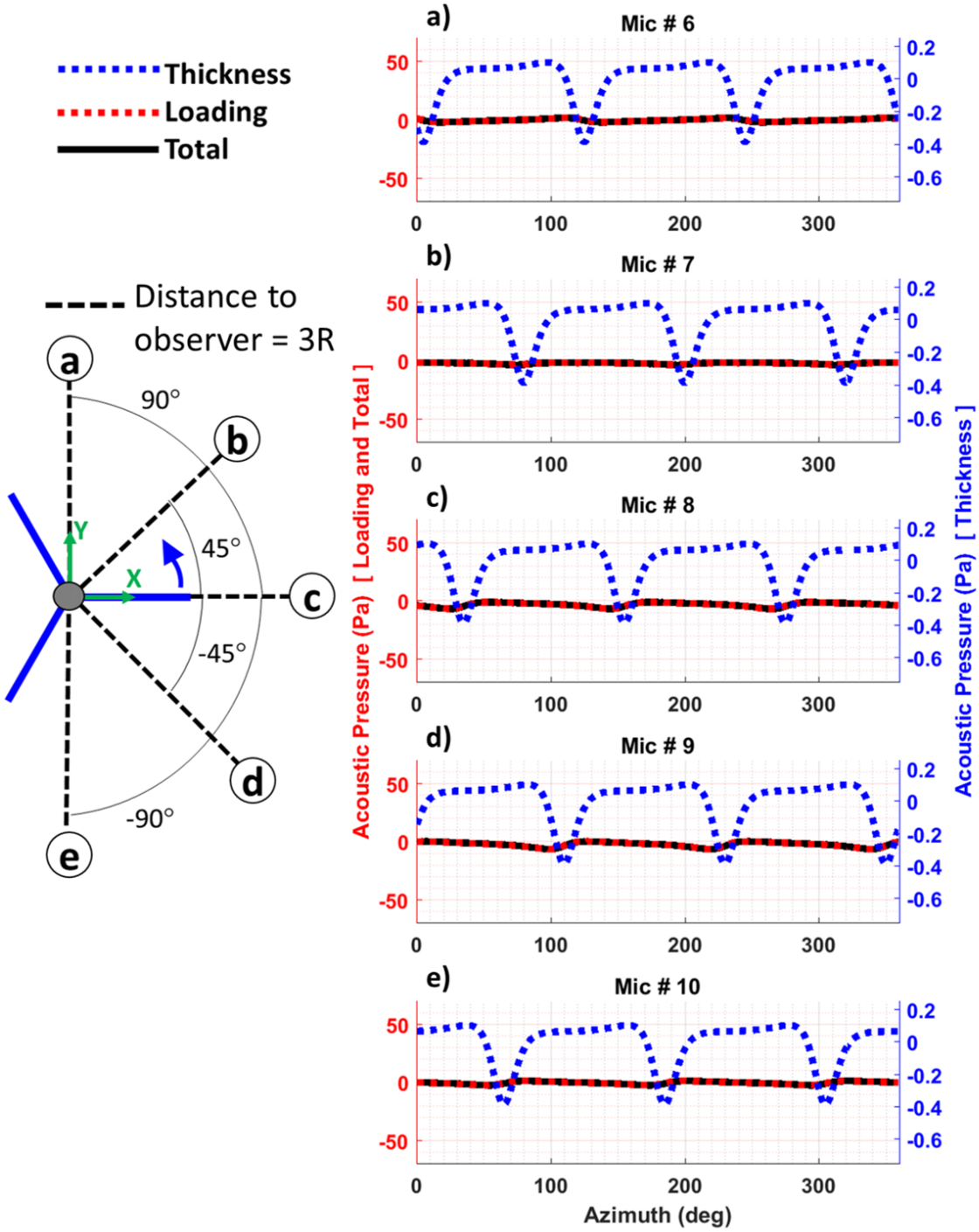

Figure 5.7: Azimuthal acoustic directivity in hover for single modern rotor acoustic pressure time history. The left (red) y-axis corresponds to loading and total noise, and the right (blue) y-axis corresponds to thickness noise.

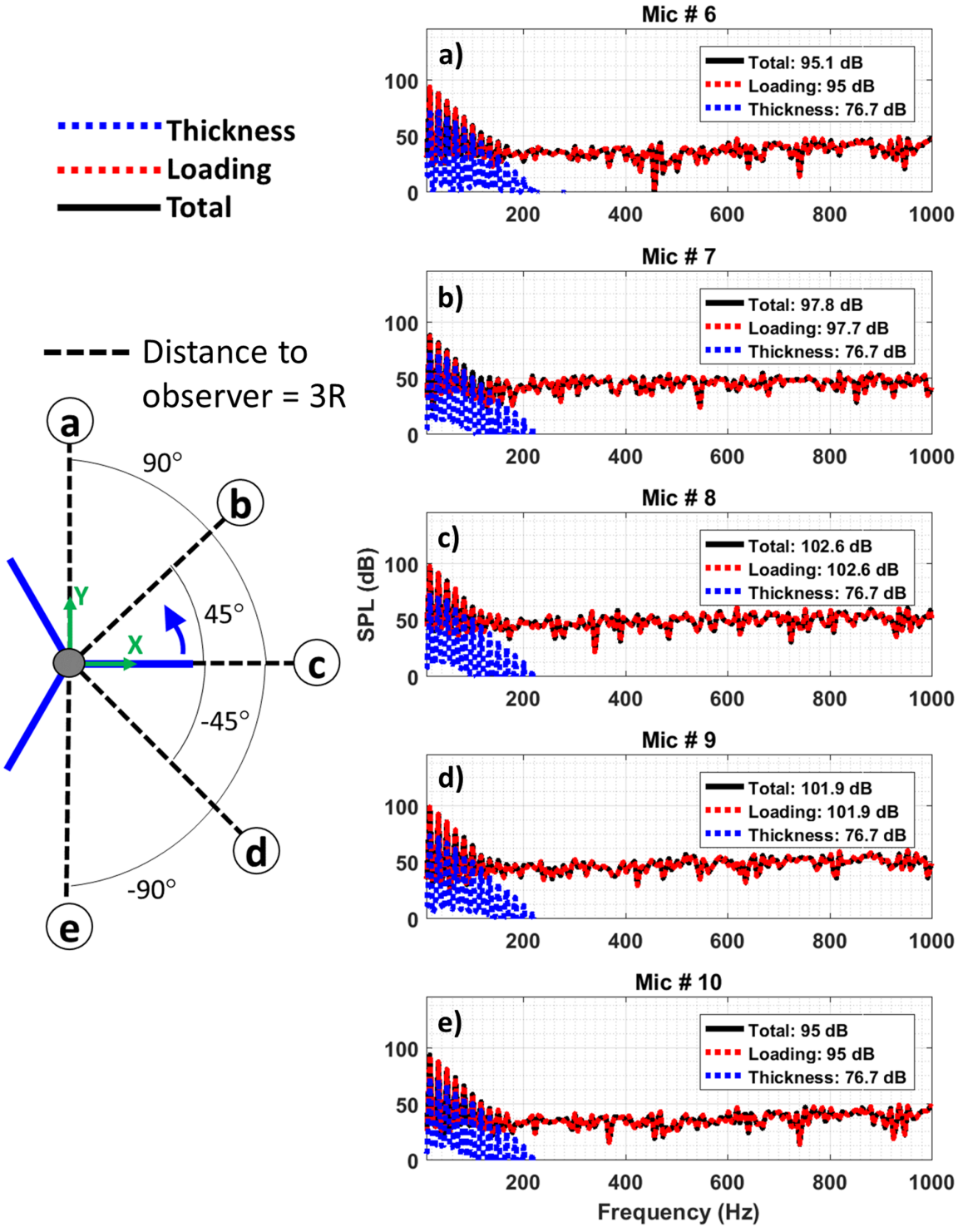

Figure 5.8: Azimuthal acoustic directivity in hover for single modern rotor frequency spectrum.

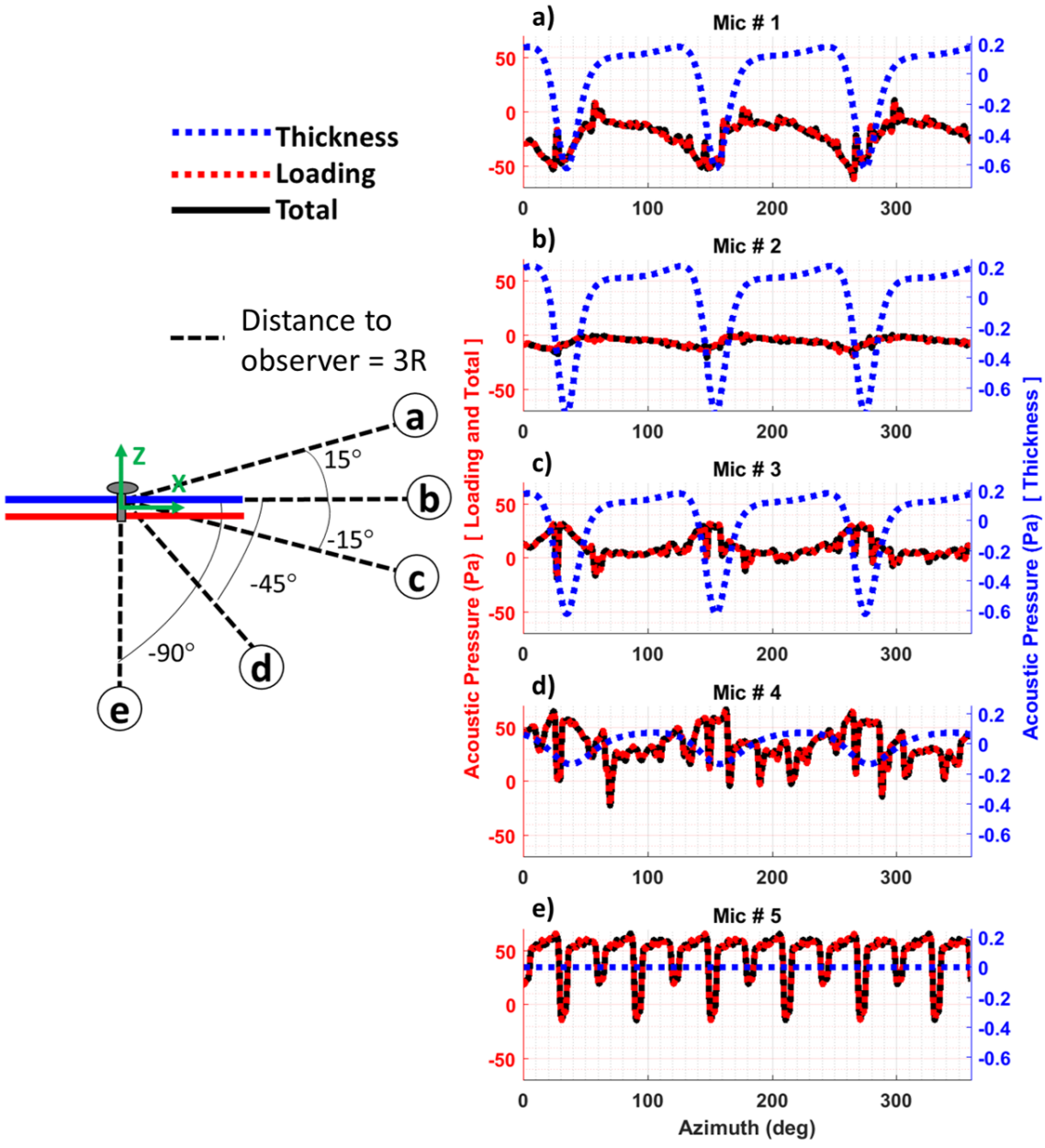

Figure 5.9: Elevation acoustic directivity in hover for coaxial modern rotor acoustic pressure time history. The left (red) y-axis corresponds to loading and total noise, and the right (blue) y-axis corresponds to thickness noise.

5.2.5 Single versus coaxial modern rotor acoustic predictions

For the single and coaxial modern rotor, thickness, loading and total noise in terms of overall sound pressure level (dB, decibels) are shown in Table 5.2, along with the difference for

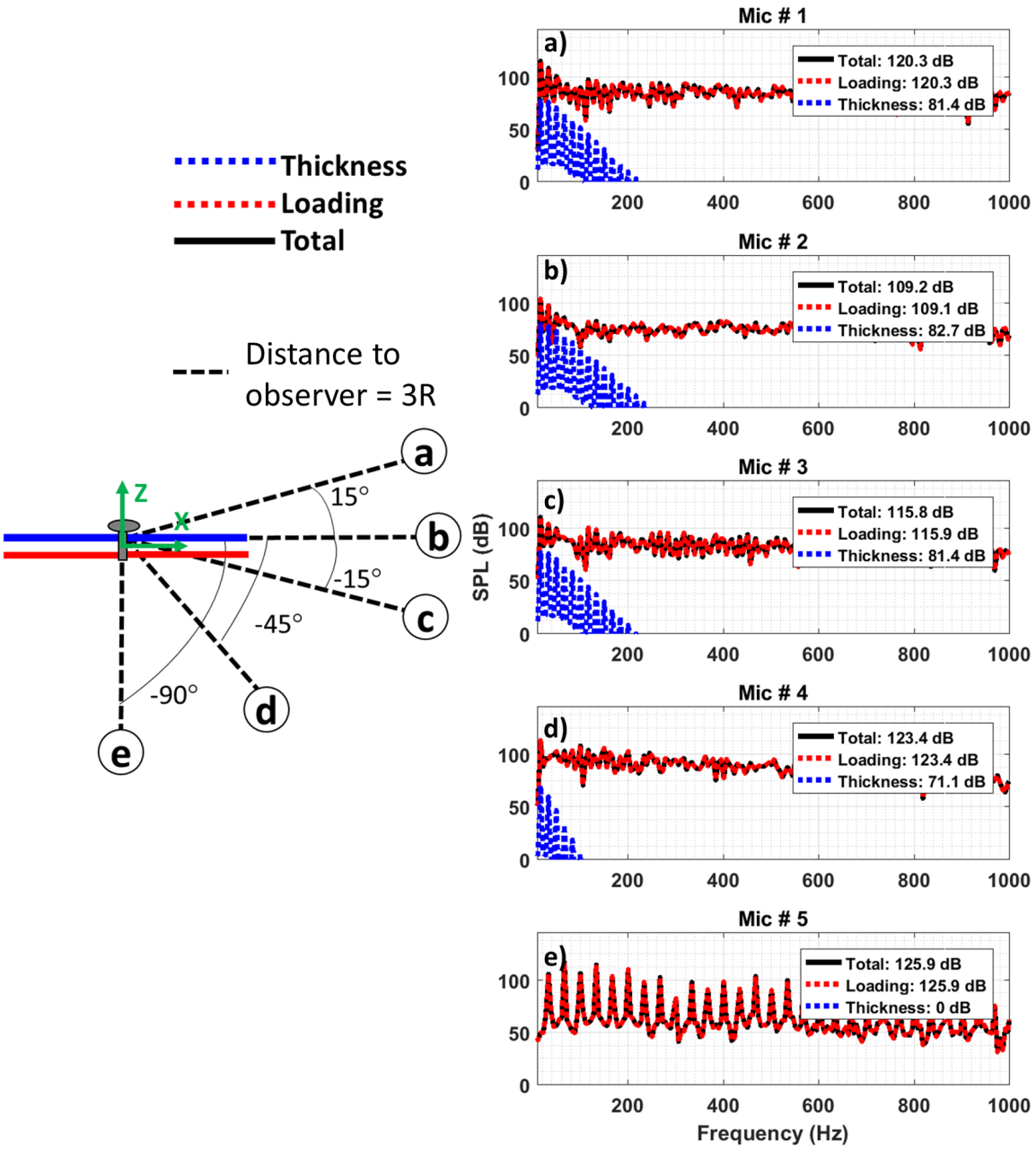

Figure 5.10: Elevation acoustic directivity in hover for coaxial modern rotor frequency spectrum.

observers 1 through 10. Thickness, loading, and total acoustic time histories are compared between the single and coaxial modern rotor design in Figs. 5.13 through 5.15.

For thickness noise, the coaxial modern rotor generates increased OASPL for all observers, compared to the single rotor also, an increase in the peaks of the acoustic pressure

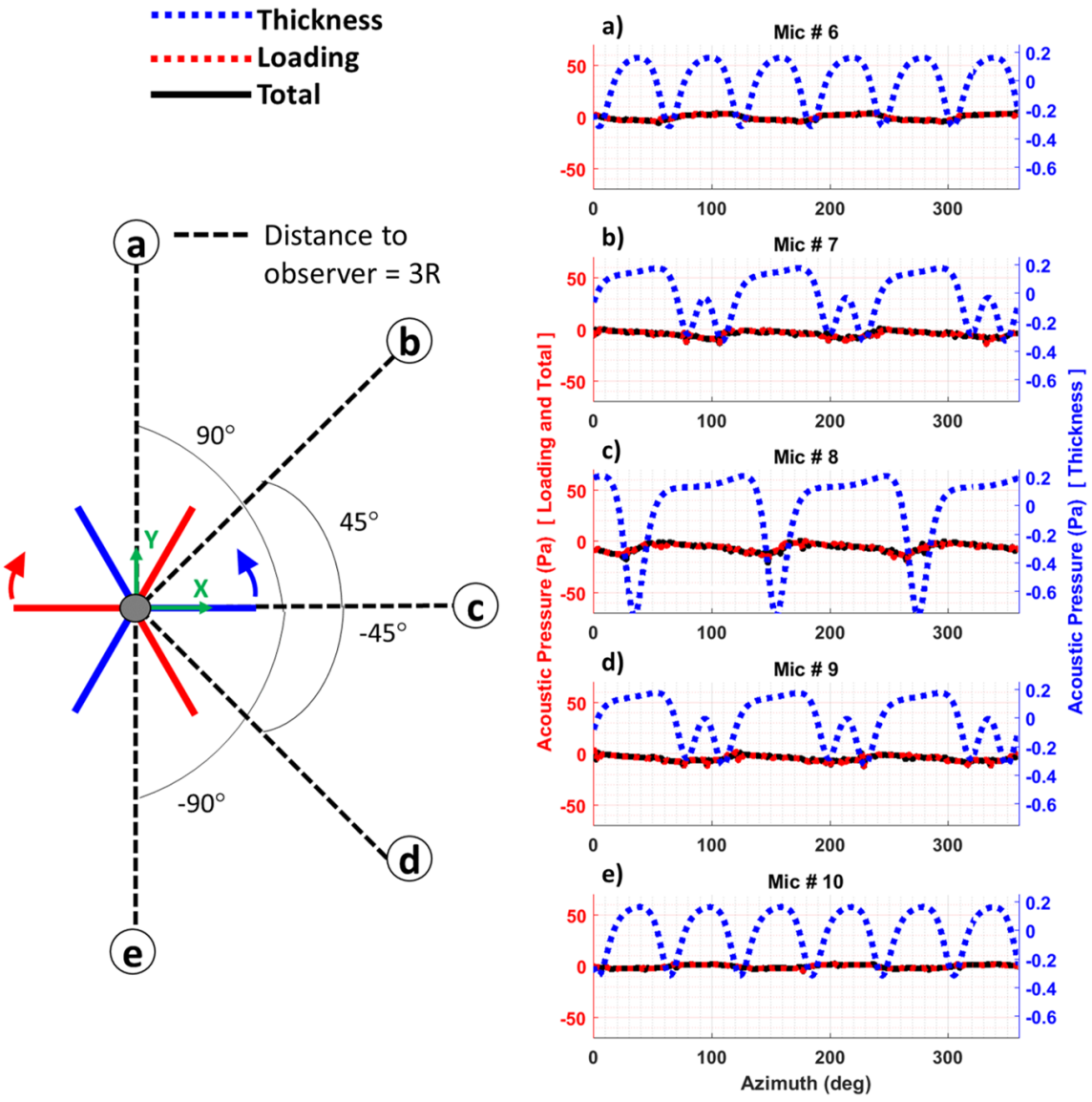

Figure 5.11: Azimuthal acoustic directivity in hover for coaxial modern rotor acoustic pressure time history. The left (red) y-axis corresponds to loading and total noise, and the right (blue) y-axis corresponds to thickness noise.

time history. As shown in Figs. 5.13 a), b), c), d), and h), the pulses for the coaxial modern rotor are larger compared to the single modern rotor. At observer locations 1, 2, 3, 4, and 8 (Fig. 5.13 a), b), c), d)), the arrival time for the upper and lower rotor blades are the same, that coincides with the same arrival time as the single rotor blades. For these specific locations, the upper and lower rotor blades are added together. When the arrival time of

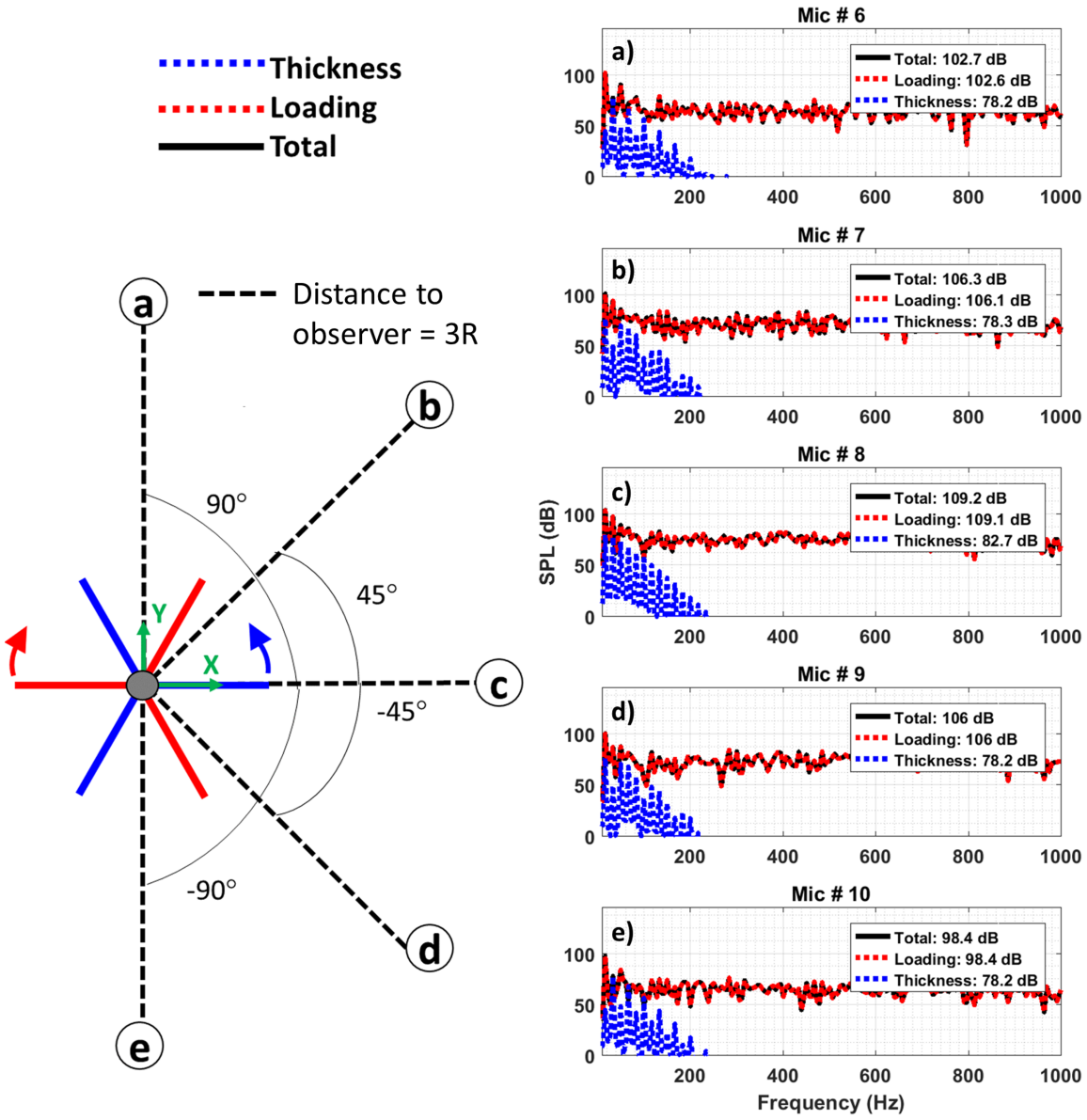

Figure 5.12: Azimuthal acoustic directivity in hover for coaxial modern rotor frequency spectrum.

the upper and lower rotor blades for the modern coaxial rotor do not coincide, six distinct pulses can be seen as shown in Figs. 5.13 f), g), i), and j) for observers 6, 7, 9, and 10. The location of observer 5 (Fig. 5.13 e)) directly below the rotor, results in no thickness noise. Observers 2 and 8 are collocated and experience the highest thickness noise OASPL.

Loading noise for the coaxial modern rotor is also higher compared to the single modern

rotor. Comparing the single and coaxial modern rotor loading calculations, a clear difference between the two is seen in Fig. 5.14 e) for observer 5. Observer 5, directly beneath the rotor, has the highest loading noise OASPL. The effect of blade overlap for the modern coaxial rotor compared is also evident in Fig. 5.14 e). The additional pulses in the coaxial modern rotor acoustic loading time history are a direct result of blade overlap (Figs. 5.3 a) and d).

Comparing the total noise for this particular configuration of a single and coaxial modern rotor, resulted in a higher OASPL for all observers for the modern coaxial rotor. Increased OASPL for the modern coaxial rotor is due to the additional rotor, that results in additional aerodynamic effects for blade crossing occurrences.

5.2.6 Summary

Acoustic predictions for a single and coaxial modern rotor were performed using PSU-WOPWOP version 3.4.3. Adjusted for tip loss, blade aerodynamic loads constructed from stacked 2D OVERFLOW results were used to predict loading noise, while the geometry of the blades and blade motion were used for thickness noise calculations. Observers were placed around the single and coaxial modern rotor to capture thickness and loading noise effects. Overall noise was higher for the coaxial rotor compared to the single rotor for this particular configuration. Effects of the blade crossing occurrences in the loading time history were manifested in the loading noise of the coaxial rotor. For this particular configuration, loading noise calculations dominated compared to thickness noise calculations for the single and modern coaxial rotor.

Table 5.2: Coaxial and single modern rotor noise sources and differences for observers 1 through 10.

Thickness noise (dB)			
Observer	Coaxial rotor	Single rotor	Difference
1	81.39	75.37	6.02
2	82.72	76.71	6.01
3	81.37	75.37	6.00
4	71.11	65.11	6.00
5	0.00	0.00	0.00
6	78.23	76.72	1.51
7	78.31	76.72	1.59
8	82.72	76.71	6.01
9	78.23	76.72	1.51
10	78.23	76.71	1.52
Loading noise (dB)			
Observer	Coaxial rotor	Single rotor	Difference
1	120.27	113.96	6.31
2	109.14	102.58	6.56
3	115.86	108.64	7.22
4	123.36	116.47	6.89
5	125.88	118.48	7.40
6	102.64	94.96	7.68
7	106.13	97.66	8.47
8	109.14	102.58	6.56
9	105.95	101.90	4.05
10	98.38	94.96	3.42
Loading noise (dB)			
Observer	Coaxial rotor	Single rotor	Difference
1	120.31	114.00	6.31
2	109.20	102.64	6.56
3	115.78	108.55	7.23
4	123.36	116.46	6.90
5	125.88	118.48	7.40
6	102.67	95.08	7.59
7	106.26	97.82	8.44
8	109.20	102.64	6.56
9	106.03	101.94	4.09
10	98.39	94.98	3.41

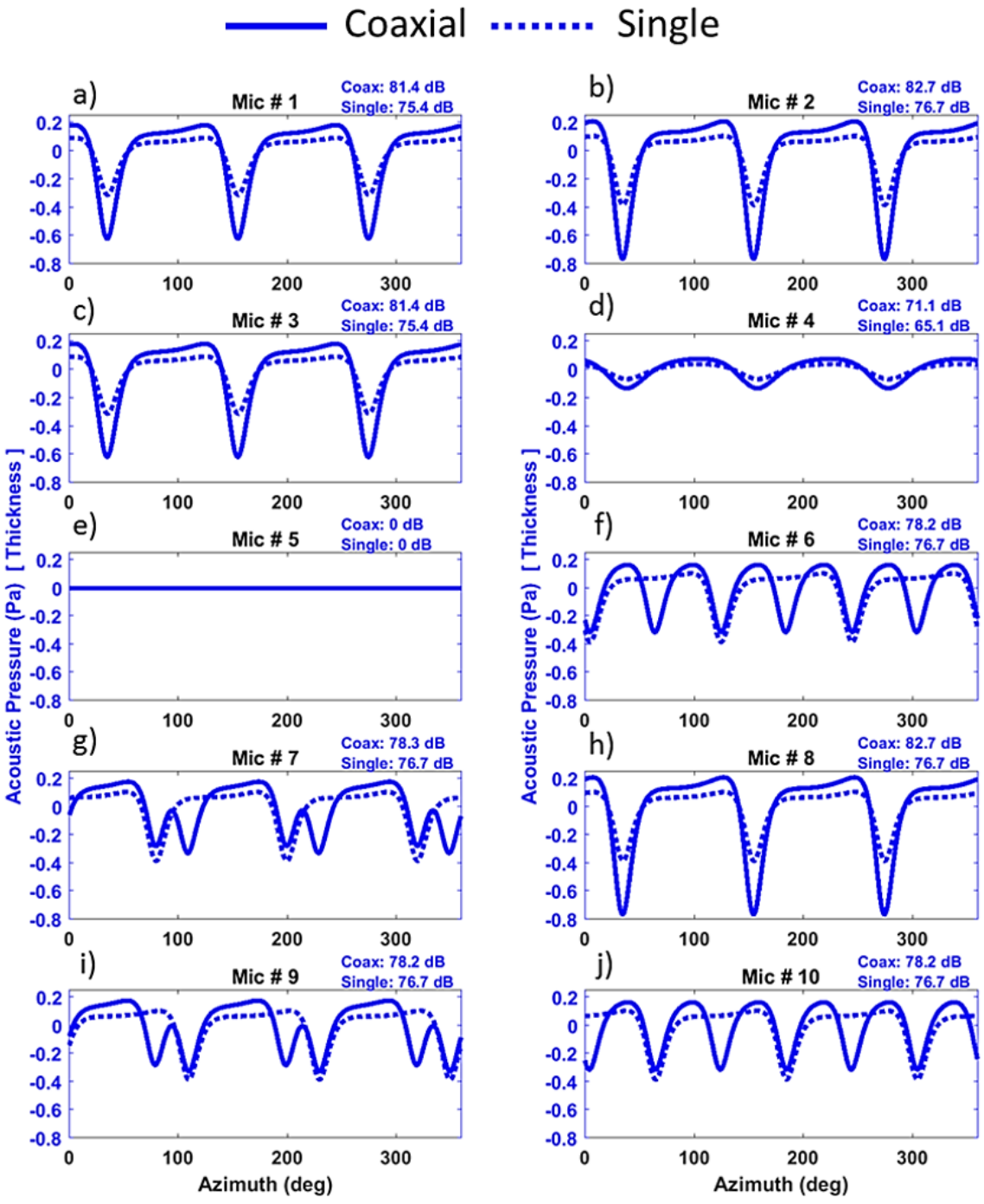

Figure 5.13: Single and coaxial modern rotor in hover. Thickness noise time history comparison for observers 1 through 10.

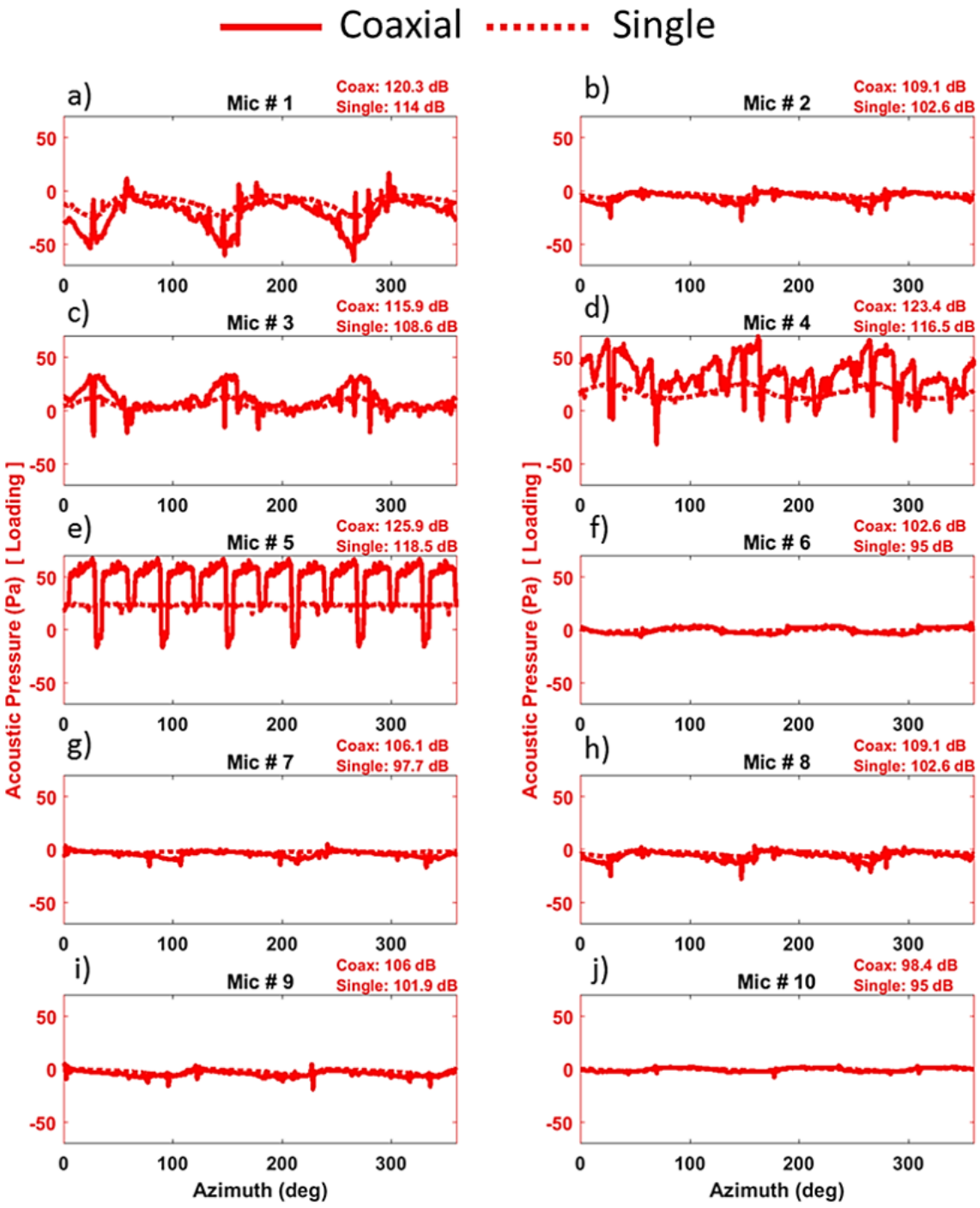

Figure 5.14: Single and coaxial modern rotor in hover. Loading noise time history comparison for observers 1 through 10.

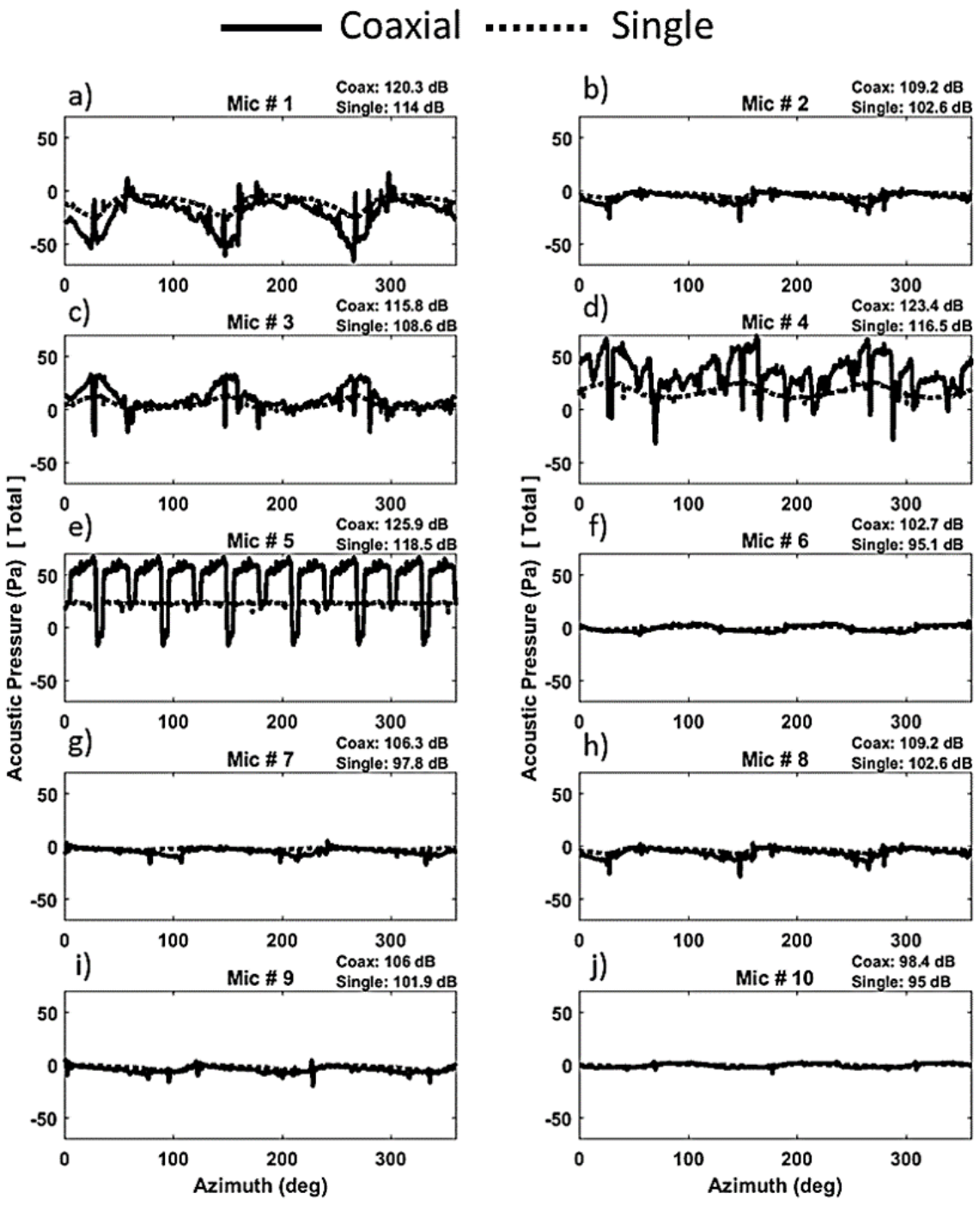

Figure 5.15: Single and coaxial modern rotor in hover. Total noise time history comparison for observers 1 through 10.

CHAPTER 6
CONCLUSIONS

Aerodynamic performance and aerodynamic noise sources of a contra-rotating rotor systems (CACR) in hover and edgewise flight were studied using various existing and new computational tools. The main aerodynamic difference between the single and coaxial rotor is the rotor wake interference, which has a larger influence on loading noise than other noise sources. Having two rotors introduces two independent acoustic signals from two independent sources, which contributes to thickness noise. BVI is more complex due to the tip vortex from the upper rotor interacting with the lower rotor blades, giving more opportunities for BVI to occur. HSI noise can be avoided by slowing the rotor or flying at lower speeds in forward flight to avoid transonic flow on the rotors, but possible shock-shock interaction could occur between upper and lower rotor blades. Broadband noise is not explored, due to its expected minimal contribution to the overall sound.

Specific aerodynamic phenomena of coaxial rotors are identified along with their associated type of rotor source noise. Contributing design parameters and flight conditions are also discussed. Conclusions from this study are provided below.

- 2D potential flow simulations of two airfoils, separated vertically, and traveling in opposite directions gave the ability to understand the aerodynamics of coaxial rotor blades before and after a blade crossing. The lift of the upper and lower airfoil increases before overlap and decreases after. The increase in lift of the upper airfoil is due to an increase in angle-of-attack caused by to the upwash from the lower airfoil, while the angle-of-attack of the lower airfoil also increases due to the upwash from the upper airfoil. After overlap, the opposite phenomena occurs, where a decrease in lift is seen for both the upper and lower airfoil.

- 2D OVERFLOW results revealed that a separation distance greater than two chords is required to minimize effects due to airfoil thickness. Furthermore, acoustic predictions revealed that thickness noise from a coaxial rotor is greater than a single rotor, but the thickness noise of both rotor systems is negligible compared to loading noise. Furthermore, the presence of deposited shed vorticity from a crossing event, was pushed downward when a vertical downwash velocity was simulated; in turn, the deposited shed vorticity from the upper airfoils directly impacts the lower airfoils. The presence of downwash reduced the angle-of-attack and therefore reduced effects due to circulation for positive angles-of-attack.

- Load calculations using 2D OVERFLOW and 3D RotUNS show significant effects when the upper and lower rotor blades of a coaxial rotor overlap. Blade crossing causes an increase in Mach number and absolute angle-of-attack. Reducing vertical separation distance can increase loading effects due to blade crossing occurrences. To identify the time and location of a blade crossing, the code RABBIT was developed, that is able to predict blade overlap for unconventional CACR designs. RABBIT accommodates varying blade phase angle and RPM, where time and location of crossing is less intuitive.

- The code RABBIT not only calculates blade overlapping time and location but also predicts BVI locations and time along with BVI strength factors, that gives designers the ability to quickly determine what flight conditions or design parameters to change in order to reduce BVI occurrences.

- To reduce the occurrence of high-speed-impulsive noise, it is suggested that the translating blade velocity not exceed Mach numbers that could result in rotor-shock interactions.

The aerodynamic phenomena investigated in this study provide insight into the complicated flow of contra-rotating rotor systems. Understanding the effect of various parameters

on the different types of coaxial rotor noise sources enables designers to consider low-noise design options that will in-turn help improve our environment.

6.1 Future work

To continue exploring coaxial rotor aerodynamics and aeroacoustics sources the following items are suggested:

- The sharp fluctuations in blade loads during blade crossings are unique features of coaxial rotors, with strong implications for bending and torsional loads on the rotor. The work presented here is a starting point for investigating these loads, and providing design tools.

- The very strong loading noise source due to blade crossings is another unique feature of coaxial rotors compared to conventional rotors. This appears to be a problem that will generate strong interest in the acoustics community, and demand innovations. Solutions may involve non-conventional blade designs.

Appendices

For a copy of the following codes and input files please contact Natasha Lydia Schatzman (contact information below).

Chapter 2: Potential flow MATLAB code VITS (Vortex Interaction Tracking Simulation)

Chapter 3: Single and coaxial (HS1 and HC1) rotor blade momentum theory MATLAB code

Chapter 4: RABBIT (RApid Blade and Blade-vortex Interaction Timer) MATLAB code

Chapter 4: BVI impulse factor MATALB code

Chapter 5: PSU-WOPWOP input files for single and/or coaxial modern rotor

Natasha Lydia Schatzman

NASA Ames Research Center

Email: Natasha.Schatzman@nasa.gov

Work phone: 650-604-5903

REFERENCES

[1] M. Mosher and R. L. Peterson, "Acoustic measurements of a full-scale coaxial helicopter," in *AIAA Aeroacoustics Conference*, Atlanta, GA, Apr. 1983.

[2] D. A. Wachspress and T. R. Quackenbush, "Impact of rotor design on coaxial rotor performance, wake geometry and noise," in *American Helicopter Society 62nd Annual Forum*, Phoenix, AZ, May 2006.

[3] H. W. Kim, K. Duraisamy, and R. E. Brown, "Aeroacoustics of a coaxial rotor in level flight," in *American Helicopter Society 64th Annual Forum*, Montreal, Canada, Apr. 2008.

[4] ——, "Effect of rotor stiffness and lift offset on the aeroacoustics of a coaxial rotor in level flight," in *American Helicopter Society 65th Annual Forum*, Grapevine, TX, May 2009.

[5] V. Samokhin, A. Kotlyar, and B. Burtsev, "Acoustic certification of helicopter ka-32a," in *27th European Rotorcraft Forum*, Moscow, Russia, Sep. 2001.

[6] D. Boyd, C. Burley, and D. Conner, "Acoustic predictions of manned and unmanned rotorcraft using the comprehensive analytical rotorcraft model for acoustics (carma) code system," in *American Helicopter Society International Specialists' Meeting on Unmanned Rotorcraft*, Chandler, AZ, Jan. 2005.

[7] C. P. Coleman, "A survey of theoretical and experimental coaxial rotor aerodynamic research," NASA, NASA TP- 3675, Mar. 1997.

[8] M. K. Taylor, "A balsa-dust technique for air-flow visualization and its application to flow through model helicopter rotors in static thrust," NACA, NACA TN- 2220, Nov. 1950.

[9] M. Ramasamy, "Measurements comparing hover performance of single, coaxial, tandem, and tilt-rotor configurations," in *American Helicopter Society 69th Annual Forum*, Phoenix, AZ, May 2013.

[10] C. G. Cameron, D. Uehara, and J. Sirohi, "Transient hub loads and blade deformation of a Mach-scale coaxial rotor in hover," in *AIAA Science and Technology Forum and Exposition, SciTech*, Orlando, FL, Jan. 2015.

[11] D. Walsh, S. Weiner, K. Arifian, T. Lawrence, M. Wilson, T. Millott, and R. Blackwell, "High airspeed testing of the Sikorsky X2 technology demonstrator," in *American Helicopter Society 67th Annual Forum*, Virginia Beach, VA, May 2011.

[12] J. G. Leishman and S. Ananthan, "An optimum coaxial rotor system for axial flight," *Journal of the American Helicopter Society*, vol. 53, no. 4, pp. 366–381, 2008.

[13] R. D. Harrington, "Full-scale-tunnel investigation of the static-thrust performance of a coaxial helicopter rotor," NACA, NACA TN- 2318, Mar. 1951.

[14] J. G. Leishman and M. Syal, "Figure of merit definition for coaxial rotors," *Journal of the American Helicopter Society*, vol. 53, no. 3, pp. 290–300, Jul. 2008.

[15] J. C. Ho, H. Yeo, and M. Bhagwat, "Validation of rotorcraft comprehensive analysis performance predictions for coaxial rotors in hover," in *American Helicopter Society 71st Annual Forum*, Virginia Beach, VA, May 2015.

[16] R. C. Dingeldein, "Wind-tunnel studies of the performance of multirotor configurations," NACA, NACA TN- 3236, Aug. 1954.

[17] W. Johnson, A. M. Moodie, and H. Yeo, "Design and performance of lift-offset rotorcraft for short-haul missions," in *American Helicopter Society Aeromechanics Specialists Conference*, San Francisco, CA, Jan. 2012.

[18] H. W. Kim and R. E. Brown, "Computational investigation of small scale coaxial rotor aerodynamics in hover," in *American Helicopter Society 62nd Annual Forum*, Phoenix, AZ, May 2006.

[19] ——, "Coaxial rotor performance and wake dynamics in steady and maneuvering flight," in *American Helicopter Society 62nd Annual Forum*, Phoenix, AZ, May 2006.

[20] O. Juhasz, M. Sya, R. Celi, V. Khromov, O. Rand, G. C. Ruzicka, and R. C. Strawn, "Comparison of three coaxial aerodynamic prediction methods including validation with model test data," *Journal of the American Helicopter Society*, vol. 59, no. 4, pp. 366–381, 2010.

[21] K. W. McAlister, C. Tung, O. Rand, V. Khromov, and J. S. Wilson, "Experimental and numerical study of a model coaxial rotor," in *American Helicopter Society 62nd Annual Forum*, Phoenix, AZ, May 2006.

[22] J. Schmaus and I. Chopra, "Aeromechanics for a high advance ratio coaxial helicopter," in *American Helicopter Society 71st Annual Forum*, Virginia Beach, VA, May 2015.

[23] D. N. Arents, "An assessment of the hover performance of the XH-59A advancing blade concept demonstration helicopter," AMRDL, Fort Eustis, VA, Report USAAMRDL-TN- 25, May 1977.

[24] R. Singh and H. Kang, "Computational investigations of transient loads and blade deformations on coaxial rotor systems," in *33rd AIAA Applied Aerodynamics Conference*, Dallas, TX, Jun. 2015.

[25] G. D. Walsh, "A preliminary acoustic investigation of a coaxial helicopter in high-speed flight," PhD thesis, Department of Aerospace Engineering, Pennsylvania State University, State College, PA, 2016.

[26] B. K. S. J. G. Walsh G. and F. Gandhi, "An acoustic investigation of a coaxial helicopter in high-speed flight," in *Proceedings of the AHS International 72nd Annual Forum*, West Palm Beach, FL, May 2016.

[27] N. L. Barbely, N. M. Komerath, and L. A. Novak, "A study of coaxial rotor performance and flow field characteristics," in *American Helicopter Society Aeromechanics Specialists Conference*, San Francisco, CA, Jan. 2016.

[28] N. L. Barbely and N. M. Komerath, "Coaxial rotor flow phenomena in forward flight," in *SAE 2016 Aerospace Systems and Technology Conference*, Hartford, CT, Sep. 2016.

[29] ——, "Compressible 2D flow field interaction of two contra-rotating blades," in *SAE 2016 Aerospace Systems and Technology Conference*, Phoenix, AZ, Nov. 2016.

[30] N. L. Schatzman, N. M. Komerath, and E. Romander, "Time-varying loads of coaxial rotor blade crossings," in *SAE 2017 Aerospace Systems and Technology Conference*, Fort Worth, TX, Sep. 2017.

[31] P. Singh and P. P. Friedmann, "Application of vortex methods to coaxial rotor wake and load calculations," in *55th AIAA Aerospace Sciences Meeting*, Grapevine, TX, Jan. 2017.

[32] ——, "Modeling coaxial rotor wakes in forward flight using viscous vortex particle method with refined blade loads," in *AHS Technical Conference on Aeromechanics Design for Transformative Vertical Flight*, San Francisco, CA, Jan. 2018.

[33] R. Feil, J. Rauleder, M. Hajek, C. Cameron, and J. Sirohi, "Computational and experimental aeromechanics analysis of a coaxial rotor system in hover and forward flight," in *Proceedings of the 42nd European Rotorcraft Forum, Lille, France*, 2016.

[34] J. H. Schmaus and I. Chopra, "Aeromechanics of rigid coaxial rotor models for wind-tunnel testing," *Journal of Aircraft*, vol. 54, no. 4, 2017.

[35] C. G. Cameron, K. A., and J. Sirohi, "Performance of a Mach-scale coaxial counter-rotating rotor in hover," *Journal of Aircraft,*, vol. 53, no. 3, pp. 746–755, 2016.

[36] T. Nagashima and K. Nakanishi, "Optimum performance and wake geometry of a coaxial rotor in hover," *Vertica*, vol. 7, pp. 225–239, 1983.

[37] A. Akimov, V. Butov, and B. Bourtsev, "Flight investigation of coaxial rotor tip vortex structure," in *American Helicopter Society 50th Annual Forum*, Washington, D.C., Jun. 1994.

[38] A. Bagai, "Aerodynamic design of the X2 technology demonstrator main rotor blade," in *American Helicopter Society 64th Annual Forum*, Montreal, Canada, Apr. 2008.

[39] G. Ruzicka and R. Strawn, "Computational fluid dynamics analysis of a coaxial rotor using overset grids," in *American Helicopter Society Aeromechanics Specialists Conference*, San Francisco, CA, Jan. 2008.

[40] J. W. Lim, K. W. McAlister, and W. Johnson, "Hover performance correlation for full-scale and model-scale coaxial rotors," in *American Helicopter Society 63rd Annual Forum*, Virginia Beach, VA, May 2007.

[41] W. Johnson, "Influence of lift offset on rotorcraft performance," NASA, NASA TP-215404, Nov. 2009.

[42] A. J. Ruddell, G. W., and R. McCutcheon, "Advancing blade concept (ABC) technology demonstrator," USAVRADCOM, Fort Eustis, VA, Report USAAVRADCOM-TR-81-D- 5, Apr. 1981.

[43] F. Bohorquez, "Rotor hover performance and system design of an efficient coaxial rotary wing micro air vehicle," PhD thesis, Department of Aerospace Engineering, University of Maryland, College Park, MD, 2007.

[44] V. K. Lakshminarayan and J. D. Baeder, "Computational investigation of small scale coaxial rotor aerodynamics in hover," in *47th AIAA Meeting Including The New Horizons Forum and Aerospace Exposition*, Orlando, FL, Jan. 2009.

[45] H. Yeo and W. Johnson, "Investigation of maximum blade loading capability of lift-offset rotors," in *American Helicopter Society 69th Annual Forum*, Phoenix, AZ, May 2013.

[46] N. Rajmohan, J. Zhao, and C. He, "A coupled vortex particle/CFD methodology for studying coaxial rotor configurations," in *American Helicopter Society Aeromechanics Specialists Conference*, San Francisco, CA, Jan. 2014.

[47] M. J. Bhagwat, "Co-rotating and counter-rotating coaxial rotor performance," in *AHS Technical Conference on Aeromechanics Design for Transformative Vertical Flight*, San Francisco, CA, Jan. 2018.

[48] F. J. Williams and D. L. Hawkings, "Sound generation by turbulence and surfaces in arbitrary motion," *Philosophical Transactions of the Royal Society of London A: Mathematical, Physical and Engineering Sciences*, vol. 264, no. 1151, pp. 321–342, 1969.

[49] M. J. Lighthill, "On sound generated aerodynamically. I. General theory," *Royal Society of London A: Mathematical, Physical and Engineering Sciences*, vol. 211, no. 1107, pp. 564–587, 1952.

[50] F. Farassat and G. P. Succi, "The prediction of helicopter discrete frequency noise," Tech. Rep., 1983, pp. 309–320.

[51] K. S. Brentner and F. Farassat, "Modeling aerodynamically generated sound of helicopter rotors," *Progress in Aerospace Sciences*, vol. 39, no. 2, pp. 83–120, 2003.

[52] A. D. Pierce, and R. T. Beyer, *Acoustics: An introduction to its physical principles and applications*. Melville, NY: Acoustical Society of America, 1991, ch. 1.

[53] R. M. Martin, M. A. Marcolini, W. R. Splettstoesser, and K. J. Schultz, "Wake geometry effects on rotor blade-vortex interaction noise directivity," NASA, NASA TP- 3015, Nov. 1990.

[54] W. Johnson, *Helicopter Theory*. Princeton, NJ: Princeton University Press, 1980.

[55] F. H. Schmitz and Y. H. Yu, "Helicopter impulsive noise: Theoretical and experimental status," NASA, NASA TM- 84390, 1983.

[56] T. F. Brooks and C. L. Burley, "Rotor broadband noise prediction with comparison to model data," *AIAA Journal*, vol. 2210, p. 2001, 2001.

[57] C. D. Harris, "Two-dimensional aerodynamic characteristics of the NACA 0012 airfoil in the Langley 8 foot transonic pressure tunnel," NASA, NASA TM- 81927, 1981.

[58] T. K. Sengupta, A. Bhole, and N. A. Sreejith, "Direct numerical simulation of 2D transonic flows around airfoils," *Computers and Fluids*, vol. 88, pp. 19–37, 2013.

[59] J. J. Bertin and M. L. Smith, *Aerodynamics for engineers*. Prentice-Hall, 1998, pp. 49–143.

[60] R. Nichols and P. Buning, "Users Manual for OVERFLOW 2.2," *NASA Langley Research Center, Hampton, VA, Aug*, 2010.

[61] W. Johnson, *CAMRAD-ii: Comprehensive analytical model for rotorcraft aerodynamics and dynamics*, Johnson Aeronautics, Palo Alto, CA, 2007.

[62] R. G. Rajagopalan, V. Baskaran, A. Hollingsworth, A. Lestari, D. Garrick, E. Solis, and B. Hagerty, "RotCFD - A tool for aerodynamic interference of rotors: Validation and capabilities," in *American Helicopter Society Aeromechanics Specialists Conference*, San Francisco, CA, Jan. 2012.

[63] K. Guntupalli, L. A. Novak, and R. G. Rajagopalan, "RotCFD: An integrated design environment for rotorcraft," in *American Helicopter Society Aeromechanics Specialists Conference*, San Francisco, CA, Jan. 2016.

[64] J. G. Leishman, "Principles of helicopter aerodynamics," in. New York, NY: Cambridge University Press, 2000, ch. 10.

[65] MATLAB, *Version 7.10.0 (r2010a)*. Natick, Massachusetts: The MathWorks Inc., 2010.

[66] W.-C. Ben, A. R. George, and S. J. Yen, "Blade-vortex interaction noise directivity studies using trace mach number," in *American Helicopter Society Aeromechanics Specialists Conference, CT*, 1995.

[67] B. Malovrh and F. Gandhi, "Sensitivity of helicopter blade-vortex interaction noise and vibration to interaction parameters," *Journal of aircraft*, vol. 42, no. 3, pp. 685–697, 2005.

[68] M. J. Bhagwat, "Effect of blade number on induced power in hover," *Journal of the American Helicopter Society*, vol. 56, no. 2, 2011.

[69] C. Hennes, L. Lopes, J. Shirey, J. Erwin, and K. S. Brentner, "PSU-WOPWOP 3.3.3 Users Guide," *The Pennsylvania State University, University Park, PA, USA*, 2009.

VITA

Natasha Lydia Schatzman was born in New Brunswick, New Jersey on November 22, 1987. She graduated from Thomas County Central High School in May 2006. Natasha received her undergraduate and Masters degree in aerospace engineering from Georgia Institute of Technology in May 2011 and 2014, respectively. She is the youngest of three children by James and Lydia Barbely. Her two older siblings are Eric James Barbely and Allen Peter Barbely. She married Dr. David Matthew Schatzman on October 22, 2016. Currently, she is a NASA civil servant aerospace engineer at NASA Ames Research Center in Moffett Field, California.